Effect of Pressure and Magnetic field on the Resistance behaviour of Transition Metal Pnictides ($BaFe_2As_2$, $BaMn_2As_2$ and $FeSb_2$)

By

T SATHYANARAYANA ANNAM

Enrolment No: PHYS 02200704012

Indira Gandhi Centre for Atomic Research, Kalpakkam

A thesis submitted to the
Board of Studies in Physical Sciences

In partial fulfilment of the requirements
For the Degree of

DOCTOR OF PHILOSOPHY
of

HOMI BHABHA NATIONAL INSTITUTE

February, 2013

Homi Bhabha National Institute

Recommendations of the Viva Voce Board

As members of the Viva Voce Board, we certify that we have read the dissertation prepared by **T Sathyanarayana Annam** entitled **"Effect of Pressure and Magnetic field on the Resistance behavior of Transition Metal Pnictides ($BaFe_2As_2$, $BaMn_2As_2$ and $FeSb_2$)"** and recommend that it may be accepted as fulfilling the dissertation requirement for the Degree of Doctor of Philosophy.

____Date:
Chairman

____Date:
Guide/Convener

____Date:
Examiner

____Date:
Member 1

____Date:
Member 2

____Date:
Member 3

Final approval and acceptance of this dissertation is contingent upon the candidate's submission of the final copies of the dissertation to HBNI.

Certificate

I hereby certify that I have read this dissertation prepared under my direction and recommend that it may be accepted as fulfilling the dissertation requirement.

Dr. A.Bharathi

Date:
Place:

STATEMENT BY AUTHOR

This dissertation has been submitted in a partial fulfilment for an advanced degree at Homi Bhabha National Institute (HBNI) and is deposited in the Library to be made available to borrowers under rules of the HBNI.

Brief quotations from this dissertation are allowable without special permission, provided that accurate acknowledgement of source is made. Request for permission for extended quotation from or reproduction of this manuscript in whole or in part may be granted by the Competent Authority of HBNI when in his or her judgement the proposed use of the material is in the interests of scholarship. In all other instances, however, permission must be obtained by the author.

T Sathyanarayana Annam

DECLARATION

I, hereby declare that the investigation in the thesis has been carried out by me. The work is original and has not been submitted earlier as a whole or in part for a degree / diploma at this or any other Institution / University.

T Sathyanarayana Annam

Dedicated to
My beloved Family

ACKNOWLEDGEMENTS

I express my sincere gratitude to my thesis supervisor Dr. A. Bharathi for her continuous encouragement, support and motivation. I am deeply grateful for her invaluable help and immense patience in the preparation and correction of this thesis. Her deep conviction, sincerity and diligence in every work she does are really very inspiring. I learnt a lot in these five years from her knowledge and experience and I always owe my sincere respects and debt of gratitude to her.

I am grateful to Dr. C. S. Sundar for his constant encouragement and support. I always amazed by his everlasting enthusiasm in science, his knowledge and his meticulous care in finding the finer details of experimental observations. He is a real source of inspiration.

I am deeply indebted to Dr. Awadhesh Mani for his encouragement, support and care. He is a very friendly and easily accessible person who readily gives his help. His knowledge is immense and he has always been there to clarify many of my doubts and in the improvement of my understanding. I am grateful for his suggestions, comments and his invaluable help during the final stage of this thesis.

I am grateful to Dr. J Janaki and Dr. T Geetha kumary for providing $FeSb_2$ samples and for their help and encouragement in the work. I would like to thank Dr J Janaki for her help and guidance in XRD analysis.

I am grateful to my friend Dr. K Vinod for his immense help in the synthesis of single crystals and in the magnetoresistance measurements. I always remember his relentless and industrious efforts for the synthesis of single crystals and I am very happy to be associated with such a good collaborator.

I would like to thank Dr. Antony Arulraj for high pressure XRD measurements and Rietveld refinements.

I would like to thank my friend Shilpam Sharma for his help in the experiments and data acquisition. His has got a good knack of Labview Programming and his help in this regard greatly improved the efficiency of data acquisition. I also thank him for his helpful discussions and support in numerous instances.

I would like to thank Dr. N Ghosh for his initial help in the magnetoresistance measurements on $BaFe_2As_2$.

I would like to thank Dr. K Gireesan for his cooperation and help in arranging unlimited supply of Liquid He for magnetoresistance measurements. I would like to thank the Liquid Helium plant staff for their help and cooperation. I am deeply grateful to Shri Kuppuswamy and Shri Selvam for their stupendous help and cooperation in all the stages of my research in the last five years.

I am grateful to Mrs. Kalavathi, Dr. V Sridharan and Mr M Sarguna for XRD measurements. Many times they came to office on holidays to do XRD measurements for my samples. I am grateful for their concern, help and interest in my work.

I would like to Dr. Shemima Hussain of UGC DAE-CSR, Kalpakkam node and Dr. G. Amarendra for the SEM characterization.

I would like to thank my labmates Dr Edward Prabhu, Paul Raj and Devidas for their help, encouragement and for all the fun we had in the lab.

I am feeling a great sense of pleasure and immense satisfaction at this moment while writing these acknowledgements to thank each and every member of Material Science Group whose help, support and whole hearted wishes made this thesis possible. My thanks are due to everyone who inspired and motivated me.

With out the mention of my friends, this page will have no meaning. I am deeply indebted to my best friends Prabakar, Prashanth and Gururaj for their moral support, encouragement, concern and help. They are always there with me in all the stages and their company and friendship made the ambience around me so lively, enthusiastic and endearing. I also cherish the memories of elated and beautiful moments I had with my friends Thirumurugan, Bharath, Srihari, Rajini, Soumee, Herojit, Prasanna and Madhu. Thank you all my dear friends for your boundless help, support, concern and care.

I would like to thank my parents, my sister and my brothers for their unconditional and boundless love, encouragement, support, care and appreciation. They are always concerned about my well being, health and happiness. I always owe to God for giving me such a wonderful family and friends, and above all for creating very healthy and happy ambience with benevolent people always around me.

CONTENTS

Chapter 1

Introduction

The magnetic properties of solids that contain *3d* electrons are generally described in terms of two opposite viewpoints. In the picture of weakly interacting itinerant electrons, magnetism arises due to different density of states for the up and down spin electrons, and this seems satisfactory in the description of metallic systems. On the other hand, for small overlap between sites or for strong local interactions, the valence electrons can form localized moments and behave effectively like local spins that can act on each other by exchange interactions, leading to various spin orderings viz., ferro-magnetic, anti-ferromagnetic, ferrimagnetic, helical ordering etc. This description is valid for insulating oxide systems. Since the magnitude of the magnetic moment is dictated by local bonding of *3d* ion with the surrounding chemical elements in a compound, a smooth transition from the itinerant to localized moment behaviour is possible by modifying the bonding in the solid, either by the application of pressure or by suitable chemical substitution. The study of metal-pnictide compounds is especially useful in this regard, as there is a covalent bond between the *3d* transition metal ion and pnictogen atom, whose degree of hybridization can be altered by the application of pressure and chemical substitution.

This thesis deals with three pnictide compounds, whose ground states show different local antiferromagnetic orders. At first is considered the Spin density wave (SDW) order, which arises from the nature of topology of the Fermi surface of itinerant electrons and holes, the example being Co doped $BaFe_2As_2$. The second deals with the G-type Anti-ferromagnetic order, arising due to exchange interactions between local Mn magnetic moments in $BaMn_2As_2$ and the third deals with a Kondo insulating order, in which a local magnetic moment on Fe couples with itinerant conduction electrons, due to the Kondo interaction, in $FeSb_2$. At first we introduce the three types of ground states investigated in this study. We then address the issue of how electronic property changes occur by application of pressure and chemical substitution. We then introduce how measuring transport properties under application of magnetic field can be used to understand the nature of the electronic states present in the system. In addtion we introduce, how the application of magnetic field can affect the magnetic state of the local moments, and in turn affect the electronic transport, in systems. In the final three sections we provide a literature survey of the relevant research work carried out on the three compounds, which form the subject matter of the thesis.

1.1 SDW Magnetic order

The spin density wave (SDW) is an antiferromagnetic ground state of metals for which the density of the conduction electron spins is spatially modulated [1]. It is a many-particle ground state of conduction electrons in the system, and is observed in metals and alloys; most prominently in chromium and its alloys. This state also occurs as a ground state in strongly anisotropic systems, for example in the one-dimensional organic conductors [1]. In these systems, below the temperature, $T_{sdw,}$ the electron gas becomes unstable and enters a collectively ordered ground state of an itinerant antiferromagnet due to nesting at the Fermi surface. Nesting describes the property of the reciprocal space to map parts of the Fermi surface with electron or hole character on top of each other by translation with the wavevector Q. In two or three dimensions a complete nesting by just a single Q-vector is not possible, but different parts of the Fermi surface can be mapped by different Q vectors in a more or less perfect way. To accomplish this, the spin density in real space should acquire a periodicity, which will be described in the following. In a metal the density of the conduction electrons with spin up (↑) and with spin down (↓) is uniform everywhere; the spatial variation of the total charge density is given by

$$\rho(r) = \rho_{\uparrow}(r) + \rho_{\downarrow}(r)$$

and only reflects the periodicity of the crystal lattice. The development of a SDW violates this translational invariance; and the charge density of a particular spin, given by, $\rho_{\uparrow(\downarrow)}$ has a sinusoidal modulation

$$\rho_{\uparrow(\downarrow)}(r) = \frac{1}{2}\rho_0(r)[1 \pm \sigma_0 \cos \vec{Q}.\vec{r}]$$

In which σ_0 is the amplitude and Q the wavevector of the SDW. The wavelength $\lambda=2\pi/Q$ of SDW is determined by the topology of the Fermi surface of the conduction electrons and in general is not a multiple of (i.e. commensurate with) the lattice period 'a'. In fact, the ratio λ/a can change with temperature, external pressure, doping and other parameters.

As will be described in detail later in the chapter, $BaFe_2As_2$ presented in chapter 3 of the thesis, is a compound, with a semi-metallic ground state. Two dimensional electron and hole pockets on the Fermi surface make possible features of nesting, since, a vector in reciprocal space can connect substantial portions of a Fermi surface (or connect separate Fermi surfaces), leading to a commensurate anti-ferromagnetic order. Interestingly, while very strong nesting favours a spin density wave state, a weaker or partial nesting seems to favour superconducting pairing via spin fluctuations. Because the shape of the Fermi surfaces and thereby the strength of nesting can be changed by manipulating the electron count, the spin-density wave state can be changed into the superconducting state by chemical substitution and by pressure, perhaps explaining the strong pressure and doping dependencies of T_c in the pnictides [2]

1.2 AFM order in magnetic sub-lattices

In a simple Neel Anti-ferromagnet there are two sub-lattice magnetizations that are opposite to each other, these can occur strictly for only the simple cubic structures. In more complicated crystal structures like the FCC, lattice frustrations are introduced, if Neel anti-ferromagnetic order is demanded. It is well known that the parent compounds of the High T_C cuprates are anti-ferromagnetic Mott insulators [3]. In La_2CuO_4, the parent compound of the first oxide compound in which High T_C, superconductivity was observed, the staggered antiferromagnetic ordering occurs due to local Cu moments in the Cu-O sub-lattice. Hole doping this sub-lattice gives rise to frustration in Anti-ferromagnetic order, which in turn favours mobility of the doped holes, leading to conduction and excitations conducive for the superconducting pairing interactions [3]. In another example viz., Na_xCoO_2, hole doping occurs on the geometrically frustrated Co sub-lattice, leading to a very large conductivity and also a large entropy of charge transport, leading to excellent thermoelectric properties [4]. Another good example of hole doping induced exotic ground state behaviour is provided by the vast variety of magnetic ground states seen in hole doped $LaMnO_3$, the pristine sample being again a Mott insulator with a robust AFM order [3].

In the fourth chapter of the thesis we present, pressure effects and chemical substitutions effects on $BaMn_2As_2$. This compound is unique among the BaT_2As_2 compounds, since it has a G-type anti-ferromagnetic insulating ground state. Detailed neutron scattering experiments reveal that the Mn moment is large ~3.9 μ_B/Mn. A comparison of the electronic structures of $BaFe_2As_2$ and $BaMn_2As_2$ systems reveal that the latter is closer to Mott localization than the former, implying that electron-electron correlations are stronger in the latter compound [5]. This suggests that the compound is very similar to the parent compounds of High T_C superconducting cuprates and the colossal magneto-resistive manganates, implying that doping $BaMn_2As_2$ with carriers can induce a superconducting ground state with a large T_c.

1.3 Kondo Insulating state

Understanding, the semiconducting behaviour of resistivity, combined with the vanishing of the magnetic susceptibility with decrease in temperature in f-electron systems viz., $Ce_3Bi_4Pt_3$, CeNiSn and SmB_6, led to the postulation of a new ground state termed the Kondo insulator in early 90's [6]. In these systems the localised *f* levels that lie in close proximity to the Fermi level, E_F, lead to hybridisation between the conduction electrons and localised levels leading to the opening of gap [6], termed the Kondo Insulating gap that can be direct or indirect [7]. In CeNiSn [6] the gap is narrow and a semi metallic state results. FeSi was the first known *3d*-electron system, which showed properties that define the Kondo-insulating ground state [7]. The central question raised by pressure and chemical substitution investigation of Kondo Insulators, is how pressure can modify, many-body effects which drive the development of the semiconducting gap [8]. Experiments are however difficult to interpret, since, in the narrow gap of the Kondo insulator, due to interfering contributions from defect states in the gap, intrinsic and extrinsic effects are difficult to delineate particularly in transport measurements [7]. In FeSi, application of pressure and isoelectronic substitution resulted in metallising this compound, the latter being dominated by defect states in the gap [9-10]. In the opposite case of an the increase in the lattice constant, it has been shown that due to a reduction in the local moment and itinerant electron hybridization, the stabilization of an itinerant anti-ferromagnetic state occurs [11]. The studies of effects and chemical substitution on the KI, $FeSb_2$ compound is dealt with Chapter 5 of the thesis.

1.4 Effect of High pressure on ground state properties

High pressure measurements provide a unique oppurtunity to perturb the groundstate, leading to phase transitions with out introducing chemical complexity in a system. With increasing pressure the lattice becomes more incompressible as the atoms have to overcome stonger repulsion potentials. This leads to the reduction in the amplitude of lattice vibrations and associated changes in the phonon spectra [12-13]. The reduced amplitude of lattice vibrations is responsible for resistivity decrease in ordinary metals [13]. As the interatomic distance decreases, the overlap of electronic orbitals increases leading to the broadening of electronic energy bands as well as shifting of different energy bands relative to each other [12,14,15,16]. As a result, overlap/separation of different bands occurs at the Fermi energy E_F, leading to changes in the electronic structure thereby altering the physical properties of materials.

Pressure also has a profound effect on magnetism. In the ferromagnetic (FM) metals like Fe, Co and Ni, the magnetic moment decreases with increase of pressure due to increase in broadening of d-bands [17]. Fe loses its magnetic moment for P > 18 GPa and Co and Ni are predicted to become nonmagnetic for application of pressures greater than 150 and 250 GPa respectively [17]. Collapse of magnetic moment occurs in the transiton metal oxides MnO, CoO and NiO which are antiferromagnetic Mott insulators, and also show insulator to metal transition at high pressures [18,19]. Superconductivity appears in some compounds under the application of pressure, in close proximity to a collapsed magnetic phase. Iron becomes superconducting in the nonmagnetic *hcp* phase under the application of pressures between 15 to 30 GPa [20]. Similarly in some heavy fermion metallic compounds, the AFM, Neel temperature decreases with increase of pressure and superconductivity emerges at low temperatures [21, 22]. Chemical substitution particularly, using isoelectronic dopants can mimic effects akin to that under application of pressure. In fact the increase in the superconducting transition temperature under pressure in $La_{2-x}Sr_xCu_2O_4$ [3], gave a clue for the synthesis of the more compressed $Y_1BaCu_2O_7$ [3] which is a archetypical high T_C superconductor at ambient pressure, with a transition temperature of 90K. In addition to reduction or increase in volume, chemical substitutions can change the electronic structure by addition of holes and electrons, giving rise new ground states that are asociated with spectacular changes in physical properties, as amply demonstrated in vast number of studies in $BaFe_2As_2$ [23].

1.5 Effect of magnetic field on ground state properties

Magnetic field is another important parameter which can affect the physical properties of a system, besides pressure and chemical substitution. Magnetic field acts on spin and orbital degrees of freedom of electrons in a material, causing changes in their magnetic and transport properties. In the case of non magnetic metals, application of a magnetic field increases the resistance due to cyclotron orbital motion of electrons and resulting in a positive magnetoresistance (MR) [24]. This is restricted to the limit of low magnetic fields, where the cyclotron frequency ω and scattering time τ, are such that $\omega\tau<<1$. In this limit, the relative mobility of carriers in the system can be determined by magnetoresistance measurements [25]. Combined with Hall measurements the number density of carriers and their mobility can be mapped as a function of temperature [25]. In the presence of high magnetic fields, when $\omega\tau>>1$, partially quantized electronic motion occurs, termed as Landau quantization [24, 25]. In this regime of magnetic field the Fermi surface topology can be determined employing single crystals from detailed analysis of the measured periodic resistivity and magnetization as a function of the inverse of applied magnetic field [25]. This method, when applied to 2D systems, led to the discovery of the Quantum Hall effect [26].

The magnetic field can be employed to affect the scattering of electrons, in systems with magnetic moments. In ferromagnetic metals negative MR results below the Curie temperature as the applied magnetic field reduces the spin fluctuations arising due to temperature [27]. On the other hand in anti-ferromagnetic metals, magnetic field increases the spin disorder by aligning spins in its direction and giving rise to positive MR [27]. In $Pr_{1-x}Ca_xMnO_3$ with ($0.3 \leq x \leq 0.5$) [28] application of magnetic field improves the Hunds coupling of electrons in the Mn ions, and leads to the metal to insulator transition bringing about the colossal MR as observed in $La_{0.75}Ca_{0.25}MnO_3$ [29]. Application of magnetic field aids in ferromagnetic order and across a magnetic transition coupled with structural transition leads to interesting effects like giant magneto-striction observed in $Gd_5(Si_{1.8}Ge_{2.2})$ [30] and giant magneto-caloric effect as observed in MnAs [31]. Another important phase transition which can be brought by magnetic field is superconductivity to normal state transition. The study of upper critical field behavior and pair breaking mechanisms in a superconductor in the presence of magnetic field is both of scientific and technological importance and is a subject of intense research in condensed matter physics [32].

1.6 $BaFe_2As_2$

The interest in $BaFe_2As_2$ can be traced to the discovery of superconductivity in fluoride doped arsenide $LaFeAs(O_{1-x}F_x)$ with $T_c \sim 26$ K, which increases to 43 K under pressure [33-34]. This remarkable discovery kindled the interest in the search for superconductivity in the transition metal pnictide systems with higher T_c. These efforts has resulted in the synthesis of several classes of Iron pnictides among which $BaFe_2As_2$ has emerged as an important compound, giving rise to superconductivity (SC) by application of pressure or chemical substitution [35-37]. One characteristic feature of these pnictide superconductors is the existence of SDW in the parent compounds, which gives way to superconductivity with electron / hole doping or under application of pressure [35]. This behaviour is very similar to two other well known classes, namely, cuprates and heavy fermion superconductors, in which T_c lies at the two extreme ranges of temperature. In the former, superconductivity emerges from a charge doped anti-ferromagnetic insulator with highest $T_c \sim 160$ K [38], while in the latter, the ground state is tuned between itinerant SDW and superconductivity with T_c as low as 1 K [21]. The $BaFe_2As_2$ based superconductors show very high upper critical fields and low anisotropy of the order ~2 -3 [40]. They also show exotic properties in their normal state like in plane anisotropy [41] and linear MR due to presence of Dirac Cone States in the electronic structure [42]. In what follows, we provide a brief description of structural and physical properties of this system.

1.6.1 Structure of $BaFe_2As_2$

$BaFe_2As_2$ exhibits $ThCr_2Si_2$ type tetragonal structure (space group I4/mmm) at room temperature [35]. It has a layered structure as shown in Fig.1.1. The unit cell contains two iron arsenide layers in which each Fe atom is surrounded by four As atoms forming edge sharing distorted $FeAs_4$ tetrahedra along the *ab*-plane. These FeAs layers are separated by layers of Ba along the *c*-axis. At 140 K, it undergoes a tetragonal to orthorhombic phase transition (space group Fmmm). At the same temperature it also shows the SDW transition. The magnetic moments are aligned ferro-magnetically along *b*-axis and antiferromagnetically along *a* and *c*-axes (see Fig.1.1) and the magnetic moment on the Fe is 0.9 μ_B [35].

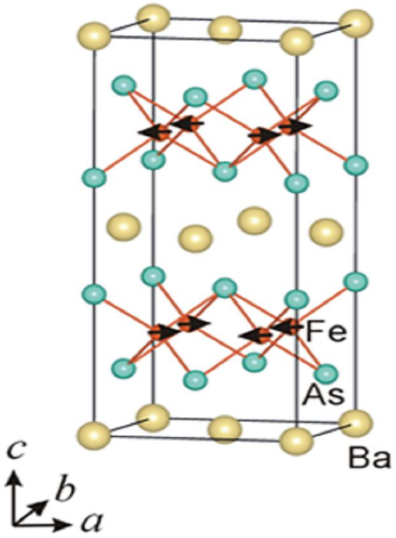

Figure 1.1: Crystal structure of $BaFe_2As_2$ [35]. The magnetic moments on Fe show the ferromagnetic coupling along b-axis and the anti-ferromagnetic coupling along a- and c-axes.

1.6.2 Electronic and Physical properties

A result of band structure calculation for parent compound $BaFe_2As_2$ is shown in Fig 1.2 for energies near E_F [43]. Here, hole bands occur at the Γ point, while the electron bands are at the X point. There is nesting of electron -type pockets of Fermi surface and hole type ones, separated by a commensurate nesting vector (π, π). This nesting vector is the same as the commensurate AFM ordering wave vector. The density of states (DOS) for holes and electrons is comparable for undoped materials; with doping of hole or electron respectively one or the other becomes dominant. Hole and electron doping strongly affect the diameter of the Fermi surfaces, resulting in the destruction of the Fermi surface nesting condition. LDA band calculations for the Fermi surfaces of 10% electron and hole doped $BaFe_2As_2$ are shown in Figure 1.3 [44]. This in addition destroys the long-range magnetic order, which is believed to bring in magnetic fluctuations, an essential prerequisite for the occurrence of superconductivity in these compounds.

Important physical properties of $BaFe_2As_2$ system are clearly captured by the bulk temperature dependent resistivity & magnetic susceptibility measurements. Resistivity in this system shows positive temperature coefficient from 4.2K to 300 K temperature range as shown in Fig 1.4 [39]. There is a sharp fall in resistivity at the SDW transition. The susceptibility of the system shows monotonic decrease from 300 to 4.2 K for application of field parallel and perpendicular to *ab*-plane [39]. Susceptibility also shows a drastic fall at 140 K at the SDW transition [see Fig.1.4]. Above the transition temperature, it does not show Curie-Weiss behavior instead it increases linearly with temperature. Such linear increase in susceptibility with temperature arises due to existence of strong antiferromagnetic correlations well above the transition temperature [39].

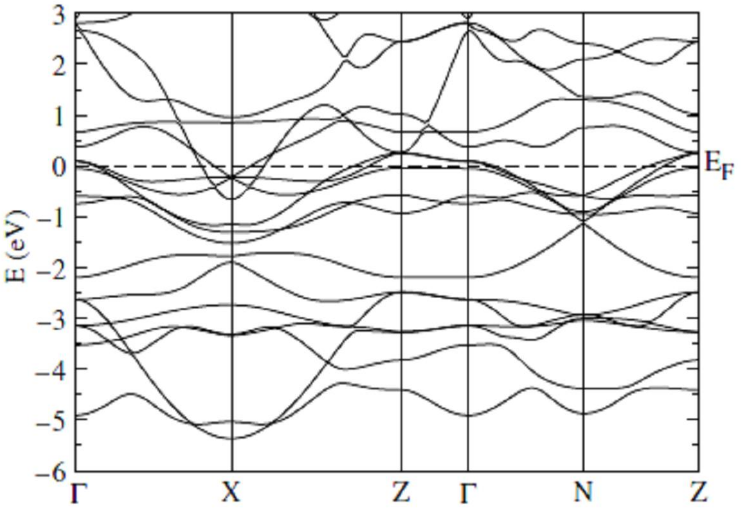

Figure 1.2. LDA band structure close to the Fermi energy E_F for body-centered-tetragonal $BaFe_2As_2$. One can clearly see hole bands at the Γ point and electron bands at the X point(s) [43]

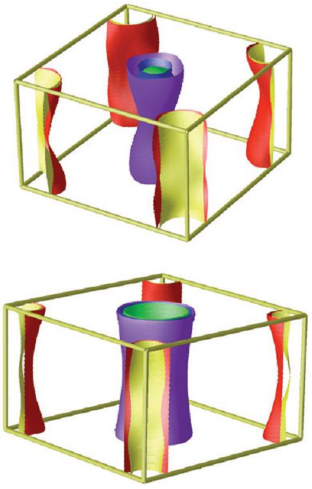

Figure 1.3 The Fermi surfaces of the tetragonal nonmagnetic 10% electron doped $Ba(Fe_{0.9}Co_{0.1})_2As_2$ (top) and 10% hole-doped $(Ba_{0.8}Cs_{0.2})Fe_2As_2$ (bottom) obtained using LDA and the virtual crystal approximation The horizontal plane is in the a–b tetragonal crystal plane, and the vertical axis is parallel to the crystallographic c-axis. The hole Fermi surfaces are in the centre and the electron Fermi surfaces are at the corners of the Brillouin zone. The figure shows that the hole Fermi surfaces shrink and expand as electrons and holes are doped into $BaFe_2As_2$, respectively. [44].

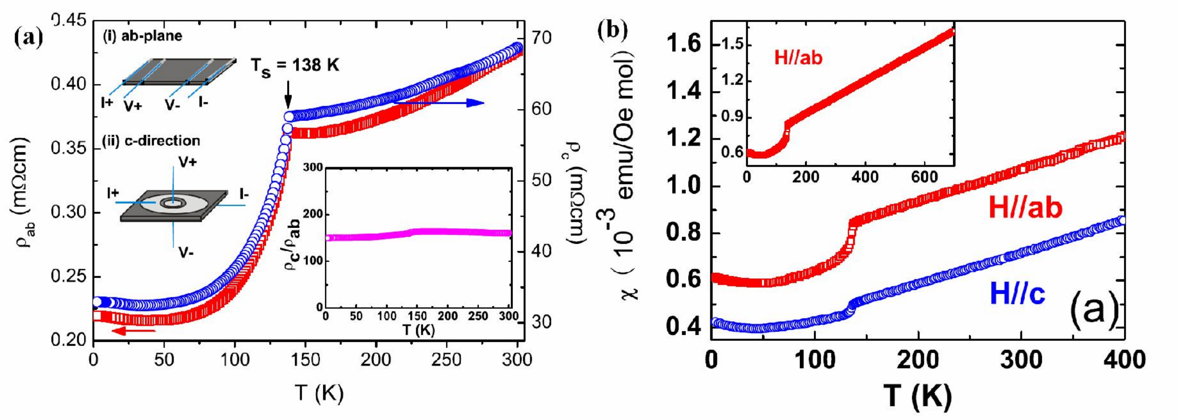

Figure 1.4 (a)Temperature dependent resistivity along ab plane and along c-axis and its ratio in the bottom right inset; (i) and (ii) show voltage and current configurations along the respective planes and (b) susceptibility variations for $BaFe_2As_2$ single crystals for H along ab and c directions. Inset shows variation along ab over a wide temperature range [39]

1.6.3 Effect of Pressure on $BaFe_2As_2$

Pressure profoundly affects the transport and magnetic properties of $BaFe_2As_2$. High pressure resistivity measurements using cubic anvil cell show systematic decrease of SDW transition (T_{sdw}) with increase of pressure up to 10 GPa and SDW phase disappears for pressures greater than 10 GPa [45]. Superconductivity appears at ~ 18 K in the pressure range 10.5 to 11 GPa and the transition temperature (T_c) decreases with increase of pressure up to 15 GPa and disappears beyond 15 GPa [45]. Resistivity measurements with Bridgman anvil cell also show similar reduction in T_{sdw} with increase of pressure but the complete suppression of SDW phase occurs at smaller pressure ~ 4 GPa in these cells as compared to the Cubic anivil cell [45-46]. The consolidated T-P phase diagram is shown in Fig.1.5, which exhibits a dome like feature for T_c with a maximum at a critical pressure. Below this pressure, the system shows the coexistence of SDW and SC phases. Above the critical pressure, only superconductivity appears and the transition temperature decreases with increase of P.

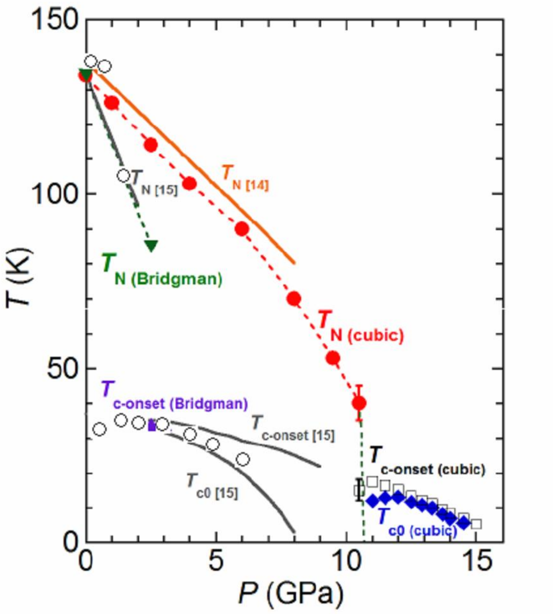

Figure 1.5 Temperature pressure phase diagram for $BaFe_2As_2$ obtained from high pressure resisitivity measurements [45,46]. The solid symbol denote results from cubic anvil cell[45] and open symbols are from Bridgeman-anvil cell[46]

1.6.4 Effect of Chemical Substitution

Similar to the application of pressure, chemical substitution also induces superconductivity in this compound. Various substitutions have been possible at Ba, Fe and As sites that give superconductivity viz., K substitution at Ba site which is also equivalent to adding holes in to the system [36], Co and Ni substitutions at the Fe site which is equivalent to adding electrons [47- 49], isoelectronic substitutions with Ru and P at the Fe [50-51] and As [52] sites gives superconductivity. A typical T-x phase diagram obtained in $BaFe_{2-x}Co_xAs_2$ is shown in Fig.1.6. Similar to the application of pressure, with increase of concentration of substituted element also, the SDW transition associated with structural transition shift to lower temperatures and superconductivity appears at low temperatures.

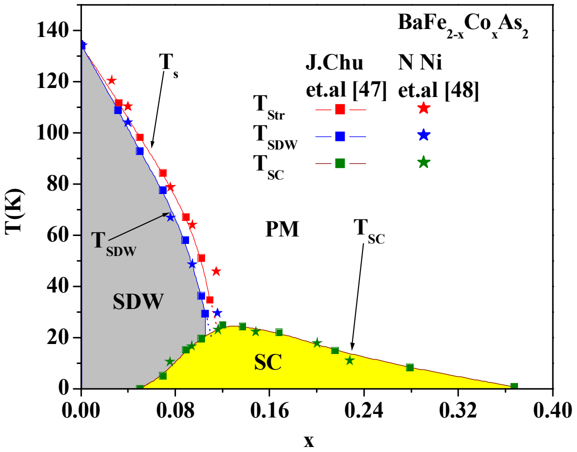

Figure 1.6 Temperature dependent resistivity variation for $BaFe_{2-x}Co_xAs_2$ single crystal at different x [47, 48] obtained from resitivity measurements

1.7 $BaMn_2As_2$ crystal structure and electronic properties

The undoped $BaMn_2As_2$ compound crystallizes in the same structure as the $BaFe_2As_2$. The physical properties [53] suggest that it has an insulating ground state with band gap of 0.03eV. Neutron scattering measuring show that the Mn atom has moment of 3.9 μ_B and it orders in a checker board like fashion, into a G-type anti-ferromagnet (see Fig 1.7) at a Neel temperature of 625K [54]. Further these studies indicate that the magnetic moment is aligned along the c-axis. The band structure calculations reveal that it has an indirect band gap [55]. Since the material is insulating it is clear that magnetism can arise from exchange interaction between localized magnetic moments. Further, detailed calculations suggest that the magnetism of the compound is well-described by the Anti-Ferromagnetic local moment Heisenberg model, with a Mn spin S = 5/2 as expected from the d^5 electronic configuration of Mn^{2+}, suggestive of a high spin configuration [56]. A comparison of the electronic structure of $BaFe_2As_2$ and $BaMn_2As_2$ system reveals that the latter is closer to Mott localization than the former, implying that electron-electron correlations are stronger in the latter compound

[5]. It has been suggested that doping $BaMn_2As_2$ with carriers can induce large magnetic fluctuations in the metallic compound and can give super conducting ground state with a large T_c. Several transition metals were substituted at Mn site, aiming at metallizing $BaMn_2As_2$. But these attempts suggest that the solubility is poor; the attempted substitutions at Mn site were with Cr, Fe, Co, Ni, Cu, Ru, Rh, Pd, Re and Pt and Sb at the As site [57]. Since pressure is seen to decrease the magnetic moment in $BaFe_2As_2$ and bring in superconductivity we explored the possibility of metallization of $BaMn_2As_2$ by the application of pressure. We do obtain a MIT at ~ 40 K with 4.3 GPa. For higher pressures this sample is completely metallized in the 4K to 300 K temperature range.

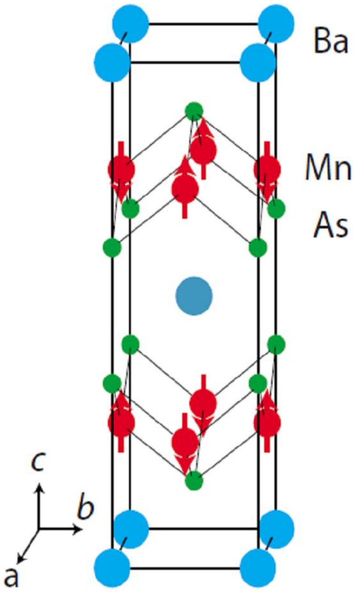

Figure. 1.7 The crystallographic and the magnetic structures of $BaMn_2As_2$. The arrows on the Mn atoms represent the *G*-type arrangement of the Mn^{2+} spins in the antiferromagnetically ordered state [54].

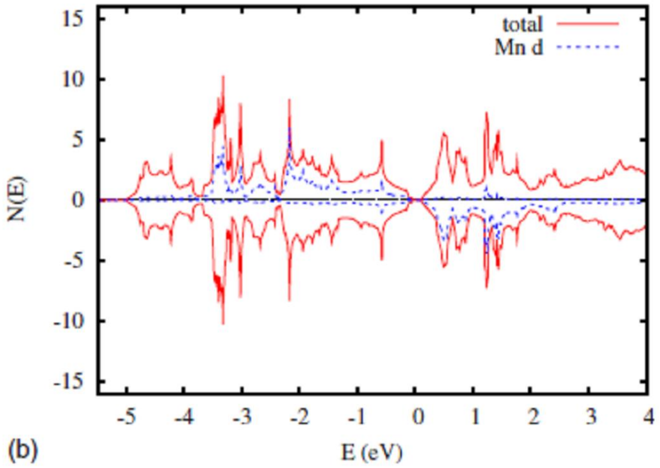

Figure. 1.8. Electronic DOS and projections onto the LAPW spheres for antiferromagnetic $BaMn_2As_2$. Plots show majority spin above the axis and minority spin below. The remaining (non-Mn) contribution to the valence bands is mainly from As *p* states. [55]

1.8 $FeSb_2$

1.8.1 Crystal Structure

The small gap semiconductor $FeSb_2$ crystallizes into a FeS_2 - type marcasite structure shown in Fig. 1.9. Basic construction units are $FeSb_6$ octahedra that form edge sharing chains along the *c* axis, which are stacked in a somewhat corrugated body-centered geometry, sharing corners in *a* and *b* directions. The lattice is orthorhombic (space group *Pnnm*), with two formula units per unit cell. [58-59].

1.8.2 Electronic structure and physical properties

Band structure calculations within density-functional theory (DFT) suggest that the electronic structure of the $FeSb_2$ is dominated by the Fe 3*d* states and the Sb 5*sp* states [58]. The calculated *DOS* is shown in Figure 1.10. The calculated direct gap is found to be around

0.2 eV. However, a clear nonzero DOS of about ~ 1 state per eV per unit cell is seen at the Fermi energy E_F indicating metallic ground state (see inset of Fig.1.10). Subsequently, detailed computations involving a many-body renormalization model revealed that in $FeSb_2$ correlation effects beyond DFT are essential for obtaining the insulating ground state [60]. Apart from this theoretical prediction, there are experimental studies which indicate the presence of strong electron correlation in $FeSb_2$ similar to that seen in the compound FeSi. Infrared optical spectroscopy measurements indicate formation of the KI gap at much lower temperatures than that corresponds to the gap energy [61-62]. This unusual behavior is seen in the Kondo insulators [63].

The temperature dependent electrical resistivity $\rho(T)$ studies on $FeSb_2$ reveals it to be a narrow gap semiconductor, which exhibits anisotropy in resistivity along the three crystallographic axes [59]. $\rho(T)$ shows insulating behavior along orthorhombic *a* and *c* axes from 2 K to 300 K, whereas it shows an insulating behavior below 40K and a metallic behavior up to from 40 K-300K along b-axis [59]. The average energy gap found by fitting $\rho(T)$ to activated behavior is found out to be ~ 300 K, which is in good agreement with the optical spectroscopy measurements [59, 61]. The mobility of the charge carriers is very high of the order of ~ 10^3 cm^2/V s [59, 64] and was attributed to result in the colossal magneto resistance observed in $FeSb_2$ [59]. The magnetization behavior could be explained based on the fact that, electron transfer occurs between two narrow bands separated by a gap with temperature, which results in changes in Pauli susceptibility, earlier used for understanding the magnetic behaviour of the Kondo insulating system FeSi [59].

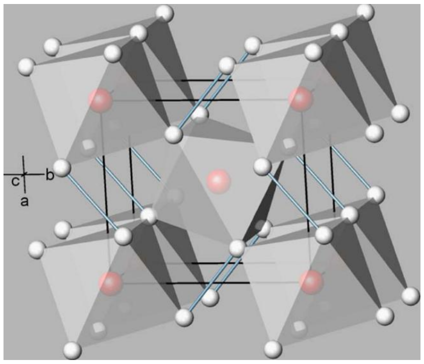

Figure. 1.9. Structure of $FeSb_2$. Red (dark) atoms are Fe and white atoms are Sb. The unit cell is orthorhombic with a =5.83 Å, b=6.54 Å, and c=3.20 Å and the structure belongs to space group No. 58 (*Pnnm)*. The Sb atoms are tetrahedrally coordinated by three Fe atoms and one Sb atom. The Fe atoms are octahedrally coordinated by six Sb atoms. The Fe-Sb and Sb-Sb dimer (dark, blue) bonds are 2.58 Å, 2.60 Å, and 2.88 Å, respectively. There are no direct Fe-Fe bonds and the shortest Fe-Fe distance is 3.20 Å. The unit cell contains two formula units. [58]

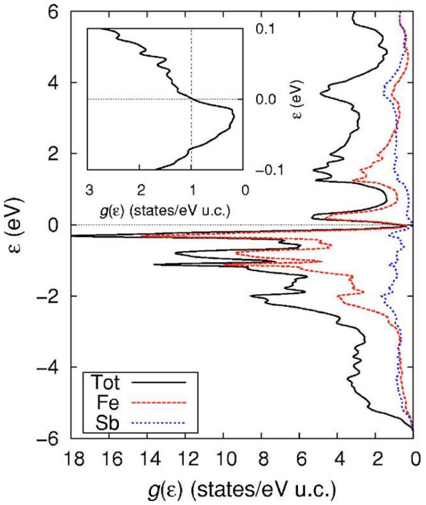

Figure 1.10. The density of states (*g)* of $FeSb_2$ as a function of electron energy ε. The straight dotted line represents the Fermi level E_F. Inset is a replot of the same data in the vicinity of the Fermi level, a nonzero $g(F_F$)is observed. [58]

REFERENCES

1. G. Gruner, *Rev. Mod. Phys*. **66**, 1 (1994)
2. M. Johannes, *Physics* **1**, 28 (2008), Zlatko Tesanovic, *Physics* **2**, 60 (2009)
3. M. Imada, A.Fujimori, and Y.Tokura, *Rev. Mod. Phys*., **70**, 1039(1998)
4. M.L. Foo, Y. Wang, S. Watauchi, H.W. Zandbergen, T. He, R.J. Cava, N.P. Ong, *Phys. Rev. Lett.* **92**, 247001 (2004).
5. Schmalian Yao , H. Wang, and Kotliar, *Phys. Rev. B* **84**, 245112 (2011)
6. G. Aeppli and Z. Fisk *Comments Condens. Matter Phys.* **16,** 155 (1992)
7. Jozef Spałek1 and Andrzej Slebarski2, *Journal of Physics: ConferenceSeries* **273,** 012055 (2011)
8. Xiao-hua Xu, Zheng-zhong Li, and Ming-wen Xiao, *Phys. Rev.* B **54**, 12 993 (1996)
9. Awadhesh Mani, A. Bharathi and Y. Hariharan, *Phys. Rev. B* **63**, 115103(2001)
10. Awadhesh Mani, A. Bharathi, S. Mathi Jaya, G. L. N. Reddy, C. S. Sundar and Y. Hariharan, *Phys. Rev. B* **65**, 245206(2002)
11. Z. wang et.al *Physica B* **199&200,** 463 (1994)
12. A. Jayaraman, *Rev. Mod. Phys*. **55**, 65 (1983)
13. B. M. Suleiman, L S. E. Gustafsson, and A. Lunden , *International Journal of Thermophysics,* **18**, 1527 (1997)
14. H. G. Drickamer and C. W. Frank, *Annu. Rev. Phys. Chem*.**23**, 39 (1972)
15. A.]ayaraman, *Annu. Rev. Mater. Sci*. **2**, 121 (1972)
16. A.K. McMahan, *Physica* B **139 & 140**, 31(1986)
17. Valentin Iota, Jae-Hyun Park Klepeis, Choong-Shik Yoo, Jonathan Lang, Daniel Haskel, and George Srajer, *Appl. Phys. Lett.* **90**, 042505 (2007)

18. Jean-Pascal Rueff and Abhay Shukla, *Rev. Mod. Phys*. **82**, 847 (2010)
19. J. R. Patterson, C. M. Aracne, D. D. Jackson, V. Malba, S. T. Weir, P. A. Baker and Y. K. Vohra*, Phys.Rev. B* **69**, 220101(R) (2004).
20. Katsuya Shimizu, Tomohiro Kimura, Shigeyuki Furomoto, Keiki Takeda, Kazuyoshi Kontani,Yoshichika Onuki and Kiichi Amaya, *Nature* **412**, 316 (2001).
21. N. D. Mathur, F. M. Grosche, S. R. Julian, I. R. Walker, D. M. Freye, R. K. W. Haselwimmer and G. G. Lonzarich, *Nature* **394**, 39 (1998).
22. Christian Pfleiderer, *Rev. Mod. Phys*. **81**, 1551 (2009).
23. Canfield and Budko, *Annu. Rev. Condens. Matter Phys*. **1**, 27 (2010).
24. A. A. Abrikosov, *Fundamentals of the Theory of Metals* (North-Holland, Amsterdam, 1988.
25. J. M. Ziman, *Principles of the theory of solids (2nd Edition)*, Cambridge University Press, Cambridge, (1972) P252.
26. M. Heilblum and A. Stern, *Physics World* **13**, 37 (2000).
27. Hiroshi Yamada and Sathoshi Takada, *J. Phys. Soc. Jpn.,* **34**, 51 (1973).
28. Y. Tomioka, A. Asamitsu, H. Kuwahara, Y. Moritomo and Y. Tokura , *Phys.Rev. B* **53**, 1689(R) (1996).
29. A P Ramirez, *J. Phys.: Condens. Matter* **9**, 8171 (1997).
30. L. Morellon, P. A. Algarabel, M. R. Ibarra,J. Blasco, and B. Garcı´a-Landa, Z. Arnold and F. Albertini, *Phys.Rev. B* **58**, 14721(R) (1998).
31. A M Tishin and Y I Spichkin, *The Magnetocaloric Effect and its Applications* , IOP Publishing Ltd 2003.

32. Charles P. Poole, H. A. Farach, R. J. Creswick and R. Prosorov, *Superconductivity*, Academic Press (2010).
33. Y. Kamihara, T. Watanabe, M. Hirano, and H. Hosono, *J. Am .Chem. Soc.* **130**, 3296, (2008).
34. H. Takahashi, K. Igawa, K. Arii, Y. Kamihara, M. Hirano, and H. Hosono, *Nature* (London) **453**, 376 (2008).
35. D C Johnston, *Advances in Physics* **59***, 803* (2010).
36. M. Rotter, M. Tegel, and D. Johrendt, *Phys. Rev. Lett.* **101**, 107006 (2008).
37. E. Colombier, S. L. Bud'ko, N. Ni, and P. C. Canfield, *Phys. Rev. B* **79**, 224518 (2009).
38. J. Orenstein and A. J. Millis, *Science* **288**, 468 (2000).
39. X. F. Wang, T. Wu, G. Wu, H. Chen, Y. L. Xie, J. J. Ying, Y. J. Yan, R. H. Liu, and X. H. Chen, *Phys. Rev. Lett.* **102**, 117005 (2009)
40. A Gurevich, *Rep. Prog. Phys*. **74,** 124501(2011).
41. Jiun-Haw Chu, James G. Analytis, Kristiaan De Greve, Peter L. McMahon, Zahirul Islam, Yoshihisa Yamamoto and Ian R. Fisher*, Science* **329**, 824 (2010).
42. Khuong K. Huynh, Yoichi Tanabe, and Katsumi Tanigaki , *Phys. Rev. Lett.* **105**, 207202 (2010).
43. L. Zhang and D.J. Singh, *Phys. Rev. B* **79**, 174530, (2009).
44. I.I. Mazin and J. Schmalian, Physica C: Superconductivity, **469**, 614, (2009).
45. Takehiro Yamazaki, Nao Takeshita, Ryosuke Kobayashi, Hideto Fukazawa, Yoh Kohori, Kunihiro Kihou, Chul-Ho Lee, Hijiri Kito, Akira Iyo, and Hiroshi Eisaki, *Phys. Rev. B* **81**, 224511 (2010).

46. Awadhesh Mani, Nilotpal Ghosh, S. Paulraj, A. Bharathi and C. S. Sundar, *EPL*, **87** 17004 (2009).
47. Jiun-haw Chu, James G Analytis, Chris Kucharczyk, and Ian R Fisher, *Phys.Rev B* **79**, 014506 (2009).
48. N. Ni, M. E. Tillman, J.-Q. Yan, A. Kracher, S. T. Hannahs, S. L. Bud’ko, and P. C. Canfield, *Phys.Rev B* **78**, 214515 (2008).
49. N. Ni, A. Thaler, J. Q. Yan, A. Kracher, E. Colombier, S. L. Bud’ko, P. C. Canfield and S. T. Hannahs, *Phys.Rev B* **82**, 024519 (2010).
50. A. Thaler, N. Ni, A. Kracher, J. Q. Yan, S. L. Bud’ko, and P. C. Canfield, *Phys.Rev B* **82**, 014534 (2010).
51. Shilpam Sharma, A. Bharathi, Sharat Chandra,V. Raghavendra Reddy, S. Paulraj, A. T. Satya, V. S. Sastry, Ajay Gupta, and C. S. Sundar, *Phys Rev B* **81**, 174512 (2010).
52. Shuai Jiang, Hui Xing, Guofang Xuan, CaoWang, Zhi Ren, Chunmu Feng2, Jianhui Dai1, Zhu’an Xu and Guanghan Cao, *J. Phys.: Condens. Matter* **21**, 382203(2009).
53. Yogesh Singh, A. Ellern, and D. C. Johnston, *Phys. Rev. B* **79**, 094519 (2009).
54. Yogesh Singh, M. A. Green, Q. Huang, A. Kreyssig, R. J. McQueeney, D. C. Johnston, and A. I. Goldman *Phys. Rev. B* **80**, 100403R (2009).
55. Jiming An, A. S. Sefat, D. J. Singh, and Mao-Hua Du, *Phys. Rev. B* **79**, 075120 (2009).
56. D. C. Johnston, R. J. McQueeney, B. Lake, A. Honecker, M. E. Zhitomirsky, R. Nath, Y. Furukawa, V. P. Antropov, and Yogesh Singh, *Phys. Rev. B* **84**, 094445 (2011).
57. Abhishek Pandey, V. K. Anand, and D. C. Johnston, *Phys. Rev. B* **84,** 014405 (2011)

58. A. Bentien, G. K. H. Madsen, S. Johnsen, and B. B. Iversen, *Phys.Rev B* **74**, 205105 (2006).
59. C Petrovic, J. W. Kim, S. L. Bud’ko, A. I. Goldman, P. C. Canfield, W. Choe and G. J. Miller, *Phys.Rev B* **67**, 155205 (2003)
60. Jan M. Tomczak, K. Haule, T. Miyake, A. Georges, and G. Kotliar, *Phys. Rev. B* **82**, 085104 (2010)
61. A. Perucchi, L. Degiorgi, R. Hu, C. Petrovic, and V. F. Mitrović, *Eur. Phys. J.* B **54**, 175 (2006).
62. A. Herzog, M. Marutzky, J. Sichelschmidt, F. Steglich, S. Kimura, S. Johnsen and B. B. Iversen, *Phys. Rev. B* **82**, 245205 (2010).
63. Z. Schlesinger, Z. Fisk, H. T. Zhang, M. B. Maplem, J. D. Di-Tusa, and G. Aeppli, *Phys. Rev. Lett.* **71**, 1748 (1993)].
64. R. Hu, V. F. Mitrović, and C. Petrovic, Appl Phys Lett. **92**, 182108 (2008)

Chapter 2

Experimental Details

Synthesis of single crystalline $BaFe_{2-x}Co_xAs_2$ *and* $BaMn_2As_2$ *samples and polycrystalline* $BaFe_2As_{2-x}P_x$, $Ba_{1-x}Yb_xFe_2As_2$ *and* $Fe_{1-x}Ni_xSb_2$ *samples are described. Different experimental tools used for the characterization of these samples, viz., dipstick resistivity, magneto resistance, vibrating sample magnetometer, high pressure resistivity and high pressure X-ray diffraction are described.*

2.1 Synthesis

2.1.1 Synthesis of precursors FeAs, CoAs , MnAs and MnP

We have adopted two step processes for synthesizing ternary arsenides. In the first step we have synthesized binary arsenides or phosphides as precursors, in a home built high pressure reaction vessel and in the second step we have used the stochiometric mixtures of these precursors to synthesize ternary arsenides. The binary pnictides, for example, the line compound FeAs is synthesized by taking stoichiometric proportions of Fe (99.99%) powder and As (99.999%) powder in a quartz crucible and locked in a stainless steel tube with a pressure 30-35 bar of ultra high pure Argon gas. The schematic of the setup used is shown in Fig 2.1. To prevent the oxidation of reaction vessel, viz. the stainless steel tube vessel during heat treatment, it is clamped inside a quartz tube with a Wilson seal, which is evacuated continuously during the heat treatment, with the help of a rotary pump. This procedure of heat

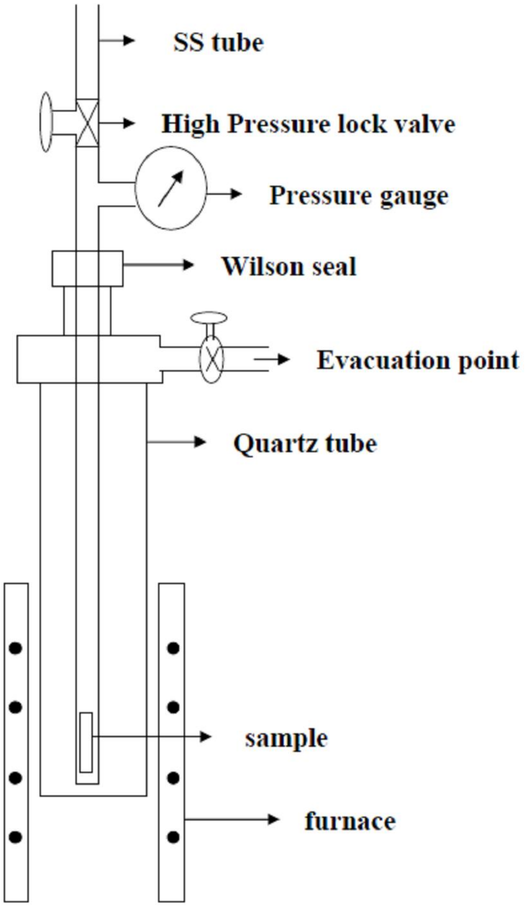

Figure 2.1: Schematic representation of the sample preparation set up for the high pressure synthesis of binary arsenides and phosphides

treating nascent arsenic under high Ar pressure environment provides a safe way, as compared with heat treating in a sealed quartz tube as the latter can explode in the case of inadvertent rise in temperature. The mixture of Fe and As is heated to 600^0C at a rate of 50^0C/hour and subsequently to 800^0C at a rate of 35^0C/hour. After dwelling at 800^0C for 5 hours the product is cooled at a rate of 50^0C/hour up to room temperature. After this first heat treatment, the mixture is ground thoroughly and the same heat treatment is repeated. The CoAs and MnAs samples are also synthesized, similarly. Due to high vapor pressure and low melting pint of P, for the synthesis of MnP, the mixture of high pure Mn (99.99%) and P(99.99%) powders are heated to 600^0C at a rate of 25^0C/hour then heated to 900^0C at a rate of 35^0C/hour, where it was soaked for five hours and then cooled at a rate of 50^0C/hour.

2.1.2 Synthesis of $BaFe_{2-x}Co_xAs_2$ and $BaMn_2As_2$ single crystals

The $BaFe_{2-x}Co_xAs_2$ ($x_{nominal}$ = 0.1, 0.15 and 0.2) single crystals are synthesized without using flux by taking stoichiometric proportions of Ba chunks and pre-synthesized FeAs and CoAs powders in an alumina crucible, which was vacuum sealed in a quartz tube. The samples are heated to 1190^0C at 50^0C/hour, held at 1190^0C for 24 hours and then slow cooled to 800^0C at a rate of 2^0C/hour followed by a fast rate of cooling of 50^0C/hour up to the room temperature. A large number of small shiny crystals with flat plate-like morphology are found in crucibles. The average size of the crystals is 2mm x 1 mm x 0.4 mm. $BaMn_2As_2$ single crystals were also synthesized by the same method by taking stoichiometric mixture of Ba

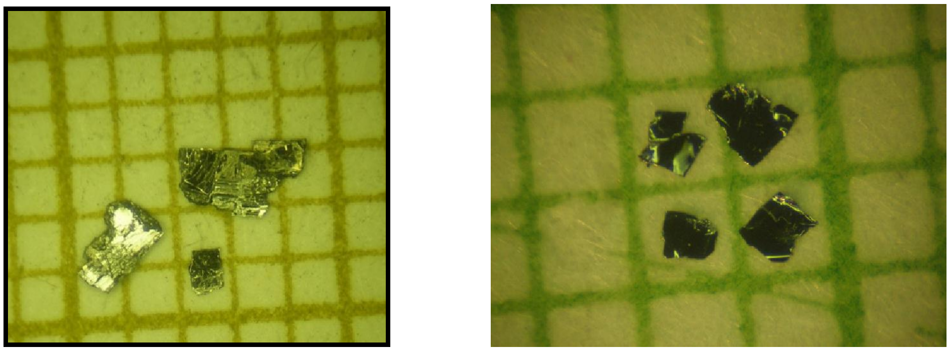

Figure 2.2: Photographs of single crystals of $BaFe_{0.85}Co_{0.85}As_2$ (left panel) and $BaMn_2As_2$ (right panel) single crystals, against millimeter grid on a graph sheet.

chunks and MnAs powder. The average size of $BaMn_2As_2$ single crystals is ~1 mm x 1mm x 0.4 mm. Fig 2.2 shows the photographs of single crystals of $BaFe_{0.85}Co_{0.85}As_2$ and $BaMn_2As_2$ on a graph paper. We have tried to synthesize single crystals of $Ba_{1-x}Yb_xMn_2As_2$ and $BaMn_2As_{2-x}P_x$ samples using the same method but the attempts were not successful and hence we have synthesized polycrystals of these samples.

2.1.3 Synthesis of $BaMn_2As_{2-x}P_x$ and $Ba_{1-x}Yb_xMn_2As_2$ polycrystals

$BaMn_2As_{2-x}P_x$ polycrystals are synthesized using solid state method. Stoichiometric proportions of Ba chunks, MnAs powder and MnP powder are taken in an alumina crucible and vacuum sealed in a quartz tube. The mixture is heated to 1100^0C at a rate of 40^0C/hour and held at this temperature for 24 hours and slow cooled at a rate of 50^0C/hour to room temperature. The samples were opened in a glove box filled with He atmosphere, ground thoroughly and pelletized. They were then vacuum sealed and sintered at 1000^0C for 24 hours. Similarly, for the synthesis of polycrystalline $Ba_{1-x}Yb_xMn_2As_2$, stoichiometric proportions of Ba chunks, Yb chunks and MnAs powder were taken and given the same heat treatment as described above. We could synthesize the samples up to doping concentrations of 15% P (x=0.3) and 15% Yb (x=0.15). Although attempts to synthesize higher concentrations of these samples were made, single phase could not be achieved.

2.1.4 Synthesis of $Fe_{1-x}Ni_xSb_2$ poly-crystals

$Fe_{1-x}Ni_xSb_2$ poly-crystals were also prepared by solid state method. Stoichiometric amounts of Fe (99.99%), Ni (99.9%) and Sb (99.99%) are taken in a quartz ampoule and vacuum sealed. The ampoule is rapidly heated to 1040^0C, held at this temperature for half an hour and subsequently quenched in water. The black pellets thus obtained were crushed into fine powder, pelletized and put again into an evacuated quartz ampoules and heated at 600^0C for 30 days.

2.2 Resistivity

Resistivity at room temperature and ambient pressure is measured using vander Pauw method [1]. The advantage of this method is that resistivity of discs with arbitrary shape can be measured. In order to apply this method for measuring resistivity, the following conditions should be satisfied. The thickness of the sample should be uniform and it should not have any holes in it. The contacts should be made sufficiently small and should be made at the circumference of the disc shaped sample. Then the resistivity of the sample at a constant temperature can be determined by solving the equation

$$e^{-\frac{\pi r_1}{\rho t}} + e^{-\frac{\pi r_2}{\rho t}} = 1 \qquad (1)$$

where r_1 and r_2 are resistances measured by passing currents and measuring voltages in the two different configurations, for instance as shown in Fig 2.3 (a) and (b), ρ is the resistivity of the material and t is the thickness of the sample.

At room temperature, for a sample of thickness,'t', we have measured resistances R_1, R_2, R_3 and R_4 for the four configurations as shown in Fig 2.3. These resistance values are substituted in equation (1) by setting (r_1, r_2) as (R_1, R_2), (R_2, R_3), (R_3, R_4) and (R_1, R_4) along with the thickness,'t', which is solved numerically using a *matlab* program to get the resistivities ρ_{12}, ρ_{23}, ρ_{34} and ρ_{14} . The room temperature resistivity ρ_{300K} is then obtained by taking the average of these four resistivities. After getting the value of ρ_{300K}, the scaling factor

'α' is determined using $\rho_{300K} = \alpha\ R_{300K}$. The resistivity as a function of temperature is then determined by scaling R (T) as $\rho\ (T) = \alpha\ R\ (T)$

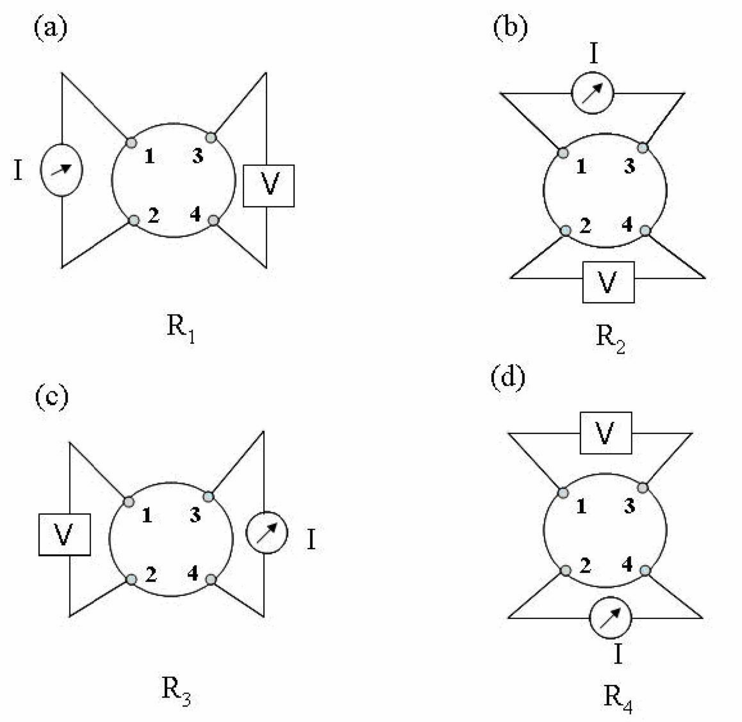

Figure.2.3: Schematic representation of the room temperature vander Pauw resistivity measurement configuration used in our laboratory.
ρ_{12} = vander (R_1, R_2, t), ρ_{23} = vander (R_2, R_3, t), ρ_{34} = vander (R_3, R_4, t), ρ_{14} = vander (R_1, R_4, t),

Resistance of the material as a function of temperature from 4.2 to 300 K can be measured by using dipper cryostat. The schematic picture of this measurement setup is shown in Fig 2.4. In this method, the sample whose resistance is to be measured is mounted on an OFHC copper block which is attached to a stainless steel (SS) tube as shown in Fig 2.4. A pre-calibrated Si diode sensor is mounted on this OFHC copper block, near the sample with proper electrical insulation, to measure the temperature of the sample. Four contacts are made

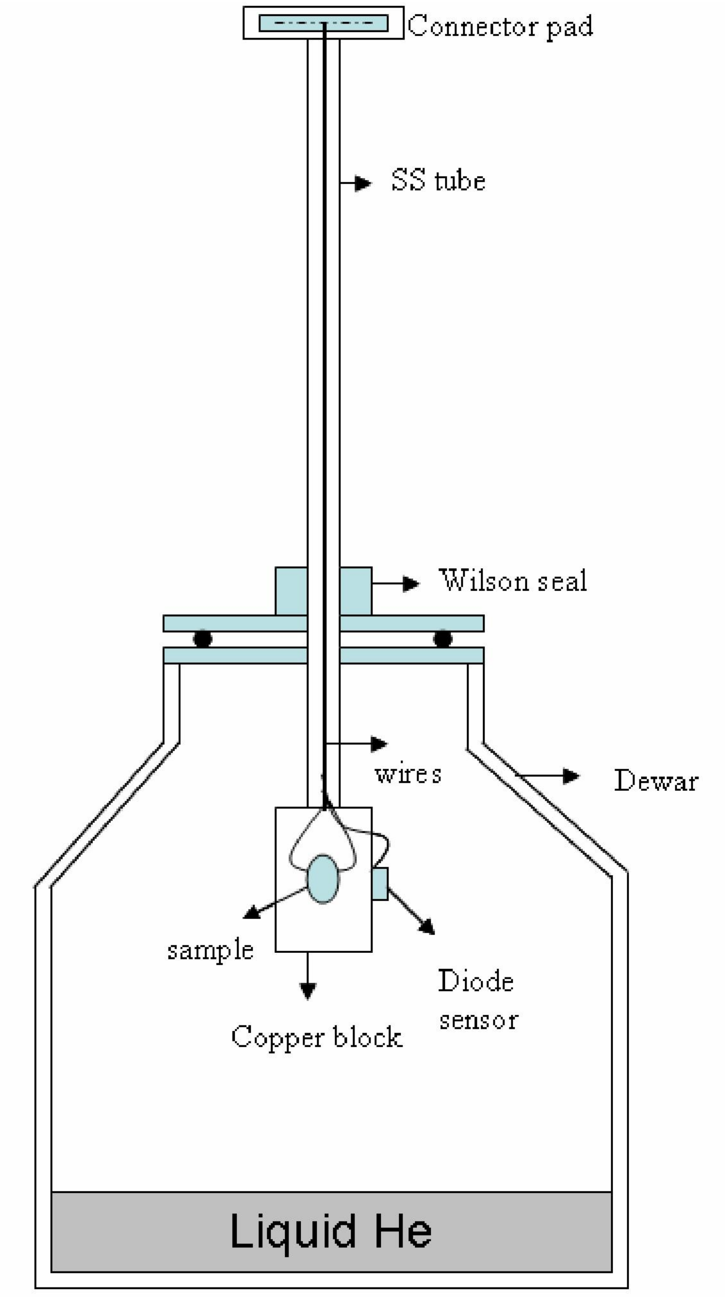

Figure: 2.4 Schematic representation of dipstick resistivity measurement setup in a 100 lit Liquid He Dewar

on the sample in the vander Pauw geometry using Cu wires (38SWG), glued to the sample with silver paint. The leads of the sensor and the sample are soldered to a connector pad, from which electrical connections to the current sources and nano-voltmeters are made. This dipstick is kept clamped at the top of a liquid Helium Dewar and slowly inserted in to the Dewar through the Wilson seal. The sample cools as it moves down in the Dewar due to the thermal gradient present in between liquid helium temperature 4.2K at the bottom and 300 K at the top of the Dewar. During the insertion of the dipstick data acquisition is carried out as follows. Currents I^+ and 10μA are passed to the sample and diode sensor through two different current sources respectively. The voltage drops V^+ and V_{d+} across the sample and diode are measured simultaneously using two different nano-voltmeters. After finishing the measurements, current direction for the sample is reversed while keeping same 10μA current for diode and the voltages V^- and V_{d-} are measured. The resultant resistance is determined as $R_s=|V_s/2I|$ where $Vs = (V^+)-(V^-)$. Subtraction of V^+ and V^- eliminates thermo-e.m.f contribution to the resistance. Simultaneously, the diode voltage $V_d = (V_{d+}+V_{d-})/2$ is converted to temperature using a *matlab* program where a set of pre-calibrated coefficients are stored, enabling conversion of measured voltage to temperature. The current sources and voltmeters are interfaced to computer through GPIB and data acquisition is automated using Labview software. After each data collection, the data are written onto a file and stored for further analysis. The measurement is generally repeated in the warming cycle also by raising the dipstick slowly to check for the repeatability of the data.

2.3 Magnetoresistance

Magnetoresistance (MR) measurements are carried out in the home-built exchange gas cryostat in which temperature can be scanned from 4.2 to 300 K and magnetic field from 0 to 12 T. The schematic picture of the cross sectional view of the cryostat is shown in Fig 2.5 a. It is evident from the schematic diagram, that the cryostat is a gas shielded, stainless steel liquid helium, belly type cryostat (CVE, Korea) with capacity of 30 liters (see Fig.2.5a). The photographs of the cryostat along with pumps used in the routine running of the setup are shown in Fig 2.5b and sample holder assembly is shown in Fig 2.5c in which magnetic field direction is marked. The evaporation rate of liquid helium in this cryostat is less than 300 cc/hour when the magnet is idle.

The superconducting magnet with a 30 mm bore housed in this cryostat is capable of producing magnetic field up to 12 Tesla. The magnet is mounted on a platform and is suspended into the tail region of the cryostat. The sample assembly is placed inside a double walled chamber inside the 30 mm bore of the magnet. The outer region of the double walled chamber, which is kept at a partial pressure (~ 8 mbar) of helium gas, is used as a thermal link to control the temperature of the sample. The inner chamber houses the sample holder assembly, filled with helium gas at a pressure of 1 bar. The desired rate of cooling and warming is achieved using a temperature controller (Oxford instruments, model ITC503) which uses a heater (Manganin wire of resistance 30 Ω) wound around a copper shield, surrounding the sample holder. The copper shield provides a uniform temperature environment for samples. The sample holder is made up of OFHC (Oxygen Free High thermal Conductivity) copper block attached to one end of a SS rod by brazing as shown in Fig 2.5 c. The SS rod together with the copper block rests on the top flange of the double wall chamber with a vacuum compatible neoprene O-ring. The current and voltage leads are thermally anchored to the SS rod at various places using GE varnish in order to avoid the thermal gradient from ambient temperature to OFHC copper sample holder. The leads are terminated at connection ports. Before a typical run the outer vacuum chamber of the cryostat is evacuated for a day or two with a turbo pump followed by pre-cooling the cryostat and the

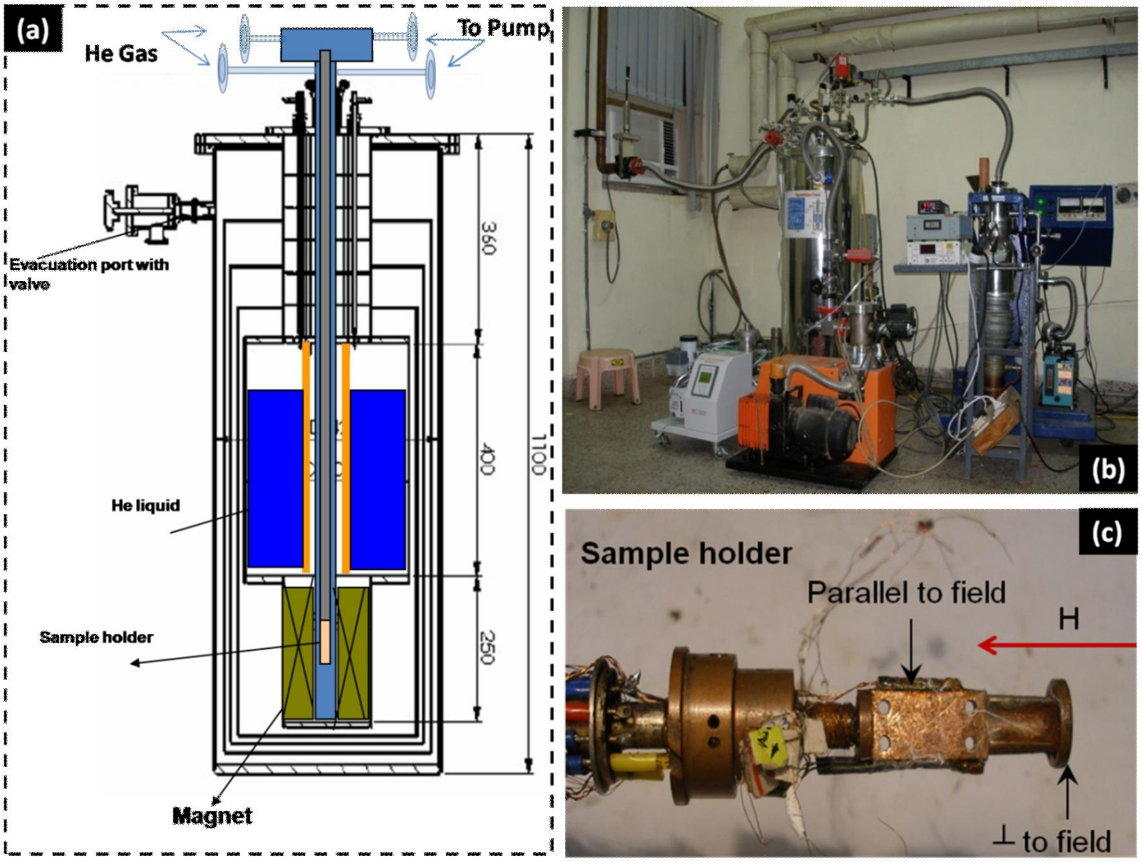

Figure.2.5: (a) Schematic cross-sectional view of the MR cryostat illustrating the position of SC magnet, sample holder etc.(b) Photograph of the MR setup (c) Photograph of the sample holder; showing the OFHC platforms mentioned in the text.

magnet, prior to liquid helium transfer. For pre-cooling, the cryostat is filled with liquid nitrogen. The cryostat remains at liquid nitrogen temperature for 12-24 hours so that the radiation shield and super-insulation cools sufficiently and reaches equilibrium. After pre-cooling, the liquid nitrogen is removed by pressurizing the cryostat with warm nitrogen gas.

Once the liquid nitrogen is completely removed, the cryostat is purged with helium gas thrice. After the purging, liquid helium is transferred. Once the liquid helium bath is filled above the magnet level, magnetic field from 0 to 12T can be applied by passing high current to the solenoidal magnet.

The sample chamber and the outer jacket are evacuated using a diffusion pump prior to pre-cooling. During helium transfer the inner and out sample chambers are filled with He gas, via the valves provided for the purpose. The inner and outer chambers are fitted with manometers to keep the gas pressures in the chambers constant, this is essential in order to achieve good control of temperatures as the PID values of the controllers is strong function of this pressure.

The sample holder has three platforms; two for mounting the samples parallel to the field and one perpendicular to the field (Fig.2.5 c). For measurements parallel to the field, the sample holder can accommodate four samples with maximum size of 5 mm diameter and 1 mm thickness (Fig.2-8c). Four samples can be mounted, two on each side of the copper block. For measurements perpendicular to the field, the sample holder can accommodate one or two samples depending up on the size. Since the size of the single crystals we used is small, we could mount two samples perpendicular to the field.

We have mounted two samples parallel and two samples perpendicular to the field for each run of the measurement. Four different set of probes each consisting of four leads are made available to the connection pad attached to OFHC copper block to feed in the current and to measure the voltage across the four samples. The resistance is measured by four probe

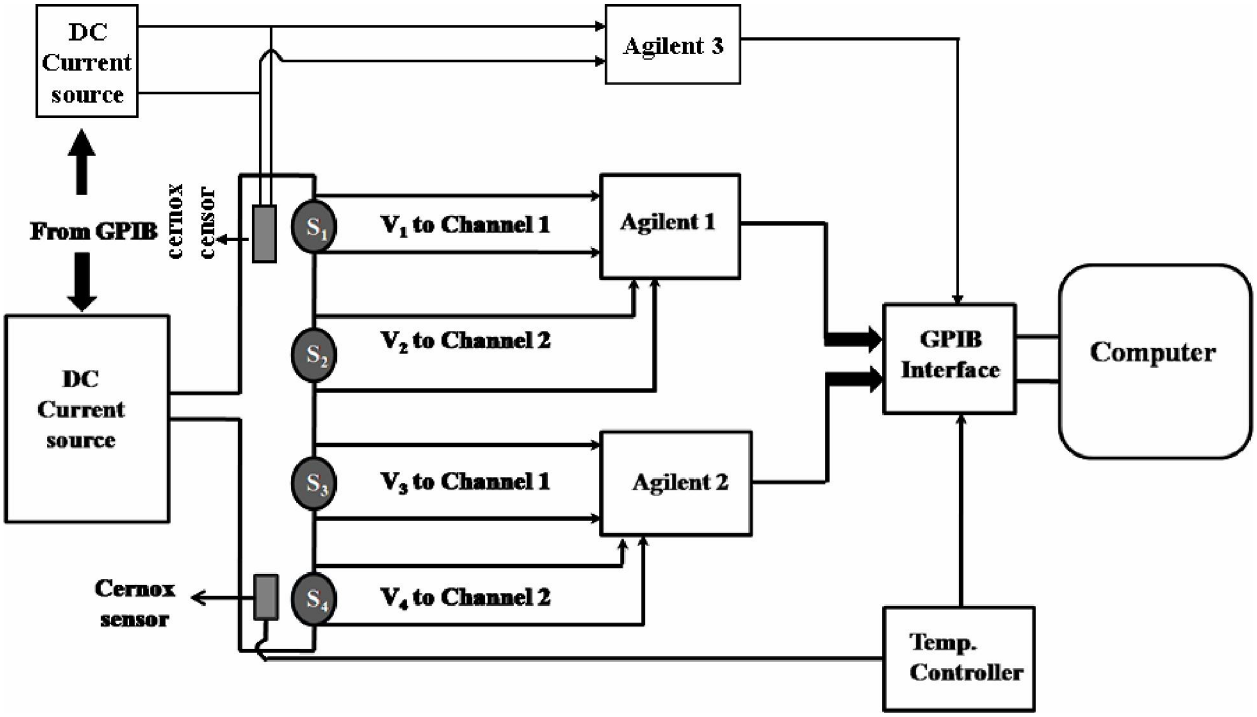

Figure.2.6: Schematic illustration of the resistance measurement in MR setup. Four samples are connected in series with a dc current source and the voltage drops across each of the samples is measured using a two channel Agilent nano-voltmeters.

technique. A calibrated DC current source (Time Electronics) is used to pass a fixed current to the sample and an Agilent (model 34420A) two channel nano-voltmeter is used to measure the voltages across the sample. The schematic diagram illustrating the method of measuring resistance of four samples simultaneously is shown in Fig 2.6. Four samples S_1-S_4 are connected in series and the voltage drops across the four samples V_1-V_4 are measured using two channel Agilent nano-voltmeters. The temperature of the sample is measured using pre-calibrated cernox sensors which are known to be good miniaturized temperature sensors insensitive to high magnetic fields. Here we have used two cernox sensors, one for controlling the temperature and the other for measuring the temperature. For the measurement thermometer, a current of 10 μA is passed and its resistance is measured similar to that in the samples, and it is calibrated to the temperature using a *matlab* program in which a set of calibration coefficients are loaded. The two cernox sensors are firmly fixed on either side of the copper block as shown in Fig 2.5 c, close to the samples. The resistances of the sample and as well as the cernox sensors are measured during positive and negative cycles of currents (to eliminate thermo-emf) and the averaged value is taken as the resistance at that particular temperature. Current sources, Agilent voltmeters and temperature controller are connected to a computer through GPIB interface and data acquisition is automated using Labview software.

2.4 High Pressure Resistivity

The high pressure resistivity measurements in the temperature range 4.2 to 300 K are carried out in a home built miniature Bridgman anvil type pressure cell that can apply pressure up to 8 GPa [2].The schematic picture of the pressure cell is shown in Fig 2.7. The overall dimensions of the pressure cell are 40 mm diameter and 140 mm length so that it can be directly inserted in to a 50 mm diameter liquid helium storage Dewar. The pressure cell contains a stainless steel guide tube, tungsten carbide anvils embedded in SS aligning sleeves, SS lock nut and dipstick attachment. Two supported tungsten carbide anvils of 12 mm diameter x 20 mm length with 4 mm flat and polished anvil faces are tight fitted into aligning SS sleeves of 5 mm wall thickness. A pair of these anvils is guided into the guide tube of 9 mm wall thickness. The upper aligning sleeve contains a slot to insert a lock pin to prevent rotation of the anvil during tightening the lock nut. Two 3 mm diameter threaded holes,

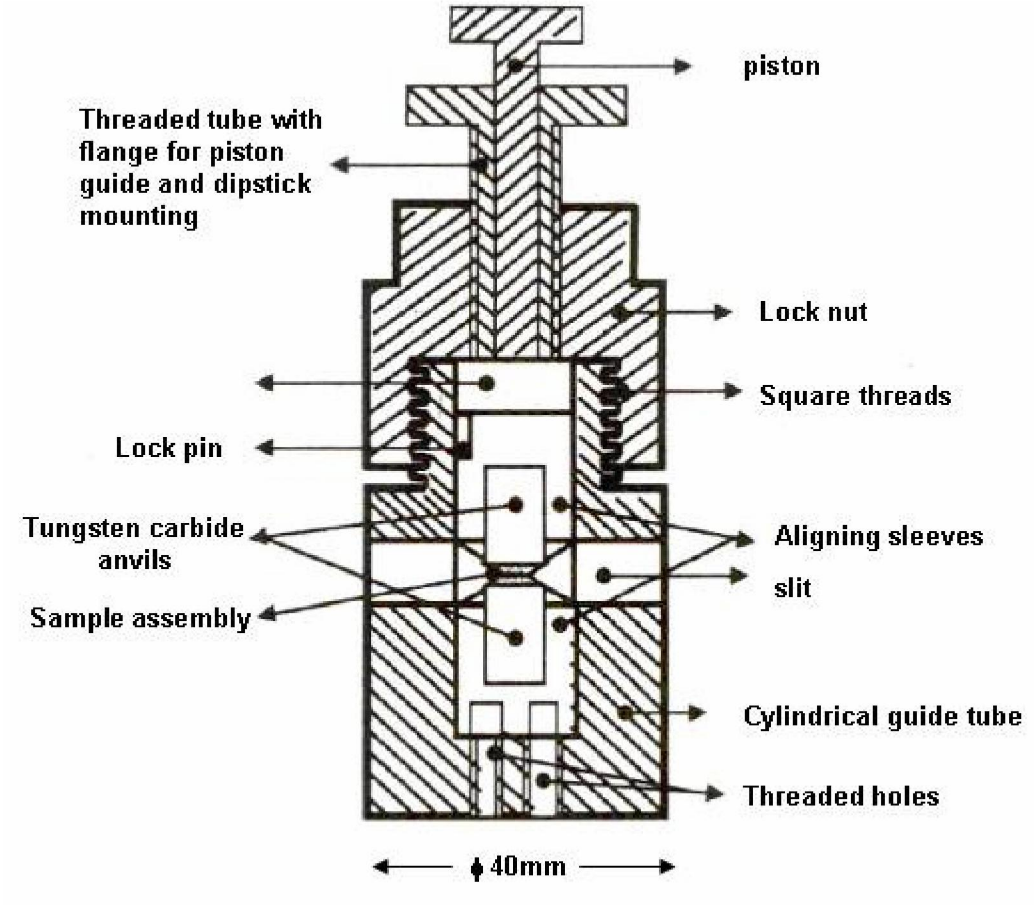

Figure 2.7: Schematic diagram of miniaturized pressure locked high pressure cell used for the resistivity investigations.

provided at the lower closed end of the guide tube, are used for removal of the bottom anvil after completion of the experiment. Two 20mm long x 5mm wide slits are machined in the guide tube to provide openings for taking out the electrical leads. The thermometer is mounted close to the sample assembly in a 3 mm diameter side hole provided on the guide tube. Load is applied on the Bridgman anvil pair using 10 mm diameter hardened steel piston (removed after clamping), which is guided by a threaded tube with a flange. The flange is finally used for mounting the pressure cell to the bottom of the dip-stick.

The schematic diagram of sample assembly is shown in Fig 2.8. The 4mm tip on the anvils constitutes the sample assembly area. A pair of pyrophyllite washers of 1 mm i.d. x 4 mm o.d x 0.17 mm thickness sandwiched together, provide the high pressure sample volume of 1mm diameter x 0.34 mm height with in which the sample is placed. Two thin disks of steatite (1 mm diameter x 0.13 mm thickness), sandwiching sample are placed in the central hole of pyrophyllite washers to provide the pressure transmitting medium. Eight electrical leads of 48 gauge Manganin wires are anchored between the pyrophyllite washers to facilitate

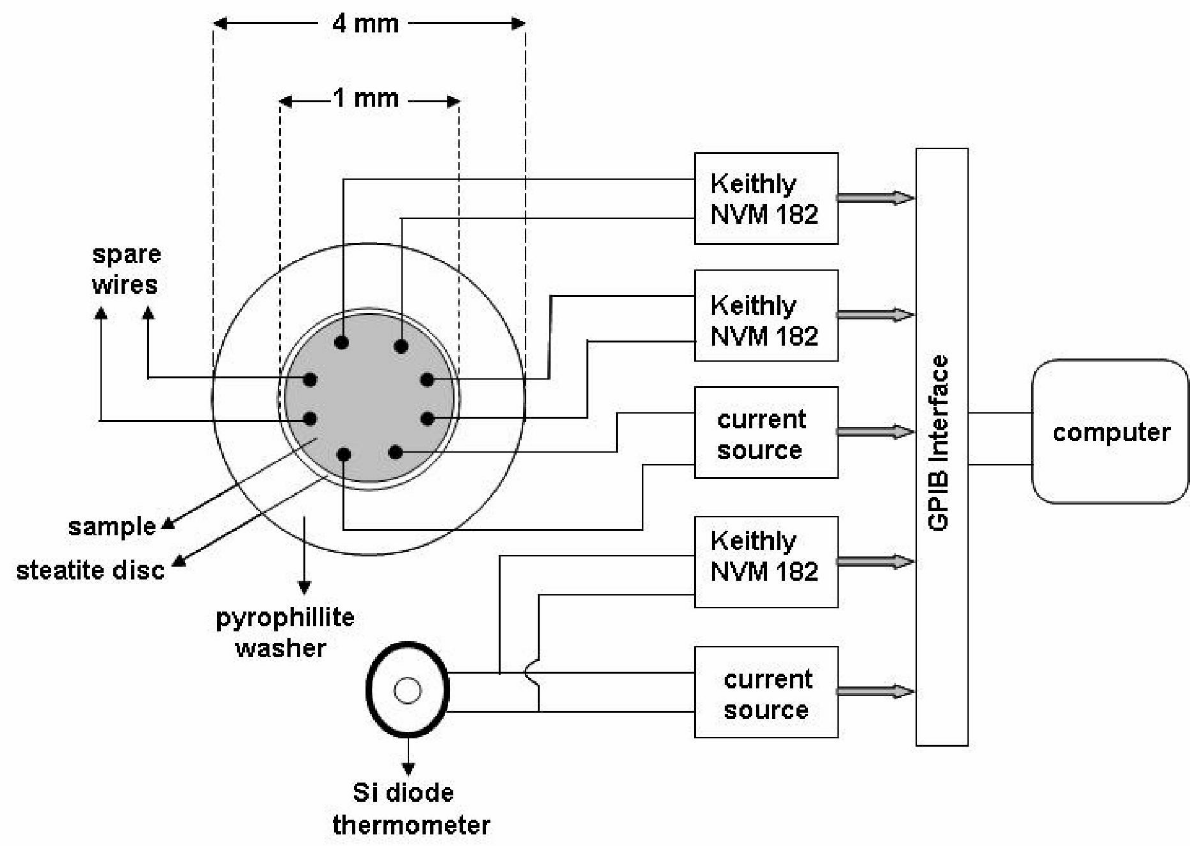

Figure.2.8: Sample assembly for four probe measurement of resistance under external pressure and low temperature.

four probe electrical resistance measurements. Current is passed between any two of the eight leads and the voltages across the sample are measured using two separate Keithley 182 nano-voltmeters as shown in Fig 2.8. It would be enough to have six electrical leads emanating from the high pressure volume in order to carry out four probe electrical resistance measurement. However, anticipating occasional lead failure, two spare electrical leads are provided so that the pressure assembly can be cycled through many pressure settings. Pressure on the anvils is applied at room temperature using a hydraulic press and locked by tightening the lock nut. The pressure locked cell is then attached to a dip-stick for low temperature measurements. Several layers of aluminized mylar foils are wrapped around the pressure cell

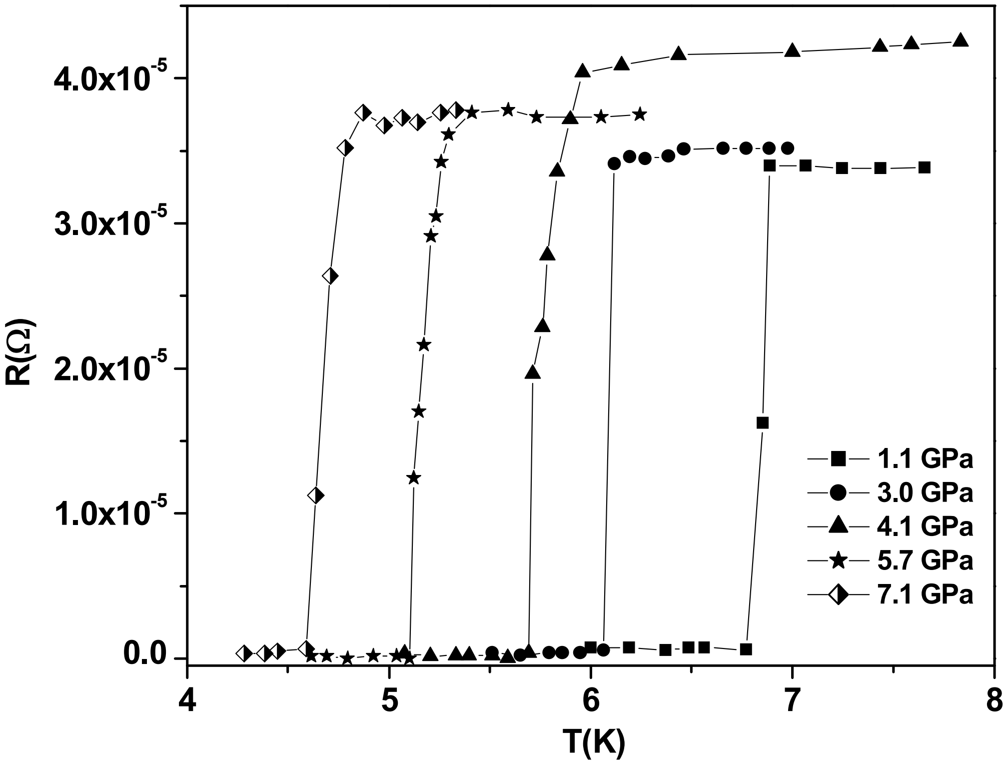

Figure.2.9: Variation of T_c of Pb at various pressures

to improve temperature uniformity in the pressure cell. The internal pressure of the cell is pre-calibrated by measuring the shift in the superconducting transition temperature of lead with respect to the applied load prior to the mounting of the samples. Fig 2.9 shows the variation of T_c of Pb sample at various applied pressures. The high pressure resistance measurements on the sample are carried out subsequently by maintaining experimental conditions similar to those used during the pressure calibration to minimize the error in the pressure measurements. However an error of ~ 0.2 GPa in the reported pressure can be expected.

2.5 Vibrating Sample Magnetometer

Magnetization measurements are carried out from 4 to 30 K on $BaFe_{2-x}Co_xAs_2$ single crystals to check for superconductivity, in a commercial (CRYOGENIC, UK) vibrating sample magnetometer (VSM). The schematic picture of VSM is shown in Fig 2.10. The VSM works on the principle of Faraday's law of induction according to which an *e.m.f.* is induced in a conductor by a time-varying magnetic flux. In the VSM, the sample is magnetized by a homogenous magnetic field and it is vibrated sinusoidally at fixed frequency of 20.4 Hz and amplitude of 1 mm with respect to two oppositely wound stationary pick-up coils. The resulting field change **B**(*t*) at a point **r** inside the detection coils induces voltage in it and is given by

$$V(t) = \int_A \frac{\partial \boldsymbol{B(t)}}{\partial t} \cdot d\boldsymbol{A}$$

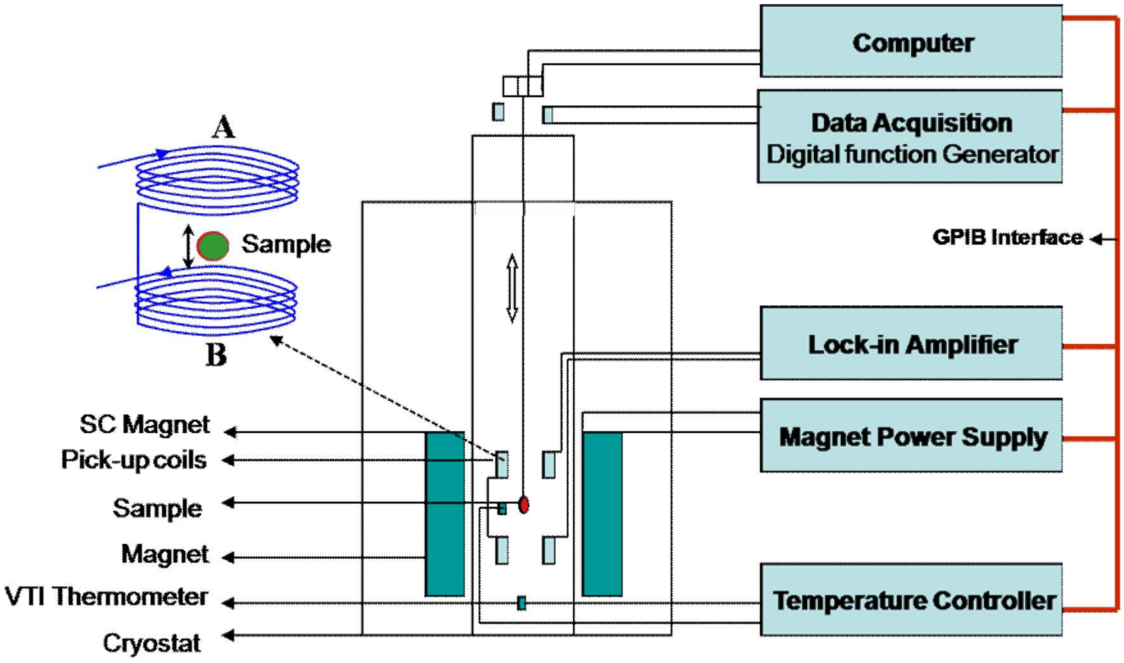

Figure.2.10: Schematic picture of vibrating sample magneometer

where **A** is the area vector of a single turn of the coil and the summing is done over *n* turns of the coils. *V*(*t*) can be detected to a high resolution and accuracy by means of suitable associated electronics. For stationary pick-up coils placed in a uniform and stable external field, the only effect measured by the coils is due to the motion of the sample. So the measured voltage *V*(*t*) is a measure of the magnetic moment of the sample.

The magnetic moment calibration was checked using standard Yttrium iron garnet (YIG) single crystal sphere supplied by CRYOGENIC. For this sample the saturation magnetic moment is 7.76×10^{-2} emu at 298 K, 5000 Oe. The magnetization versus applied field at 298 K for the YIG sample is shown in Fig 2.11 a. We have also checked calibration

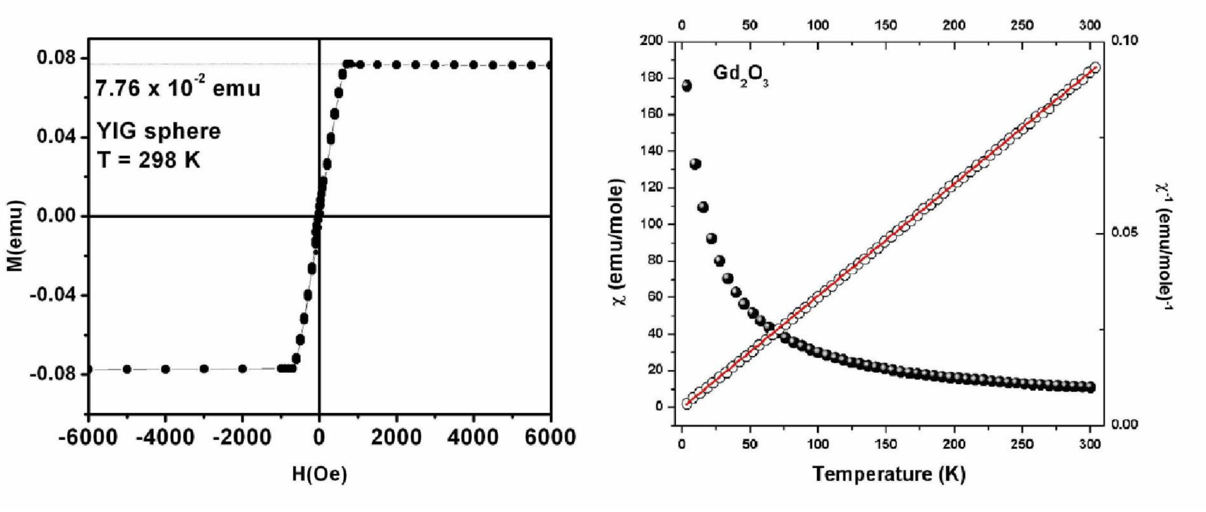

Figure.2.11: (a) Magnetisation versus applied field for YIG sample at 298 K. **(b)** Temperature dependent DC susceptibility and Curie-Weiss fit of the Gd_2O_3 sample measured in the VSM.

using standard Gd_2O_3 sample. Gd_2O_3 is a very stable oxide with Curie-Weiss-like temperature dependent susceptibility that is known to be used for calibration of DC susceptibility measurements [3]. The estimated magnetic moment of Gd from the VSM is $8.02 \pm 0.05\ \mu_B$ against the standard value of $7.98\ \mu_B$. The temperature dependent paramagnetic behavior and Curie-Weiss fit of Gd_2O_3 measured in the VSM is also shown in Fig.2.11 b.

2.6 XRD characterization

The room temperature powder X-ray diffraction(XRD) pattern of all the samples studied in this thesis are recorded using a STOE diffractometer operated with a power of 40 kV and 30 mA, in the Bragg-Brentano geometry. The X-ray radiation used was the Cu-K_α line. The lattice parameters from XRD pattern are extracted using STOE and PCW [4] programs.

High pressure XRD experiments are carried out at room temperature using a Mao-Bell type diamond anvil cell (DAC) in an angle-dispersive mode up to 10 GPa [5]. The sample in the powder form was loaded in to 200 μm diameter hole drilled in a stainless steel gasket. A mixture of methanol, ethanol and water in the volume ration 16:3:1 is used as a pressure transmitting medium. The incident Mo x-ray beam obtained from a Rigaku ULTRAX (18 kW) rotating anode x-ray generator is monochromatized with graphite monochromator. An image-plate-based mardth345 diffractometer was used. The overall resolution of the diffractometer system is $\delta d/d \approx 0.001$. The Mao-Bell type DAC was fitted to the diffractometer and sample to detector distance was calibrated using a standard specimen like LaB_6. The equation of state of silver is used for pressure calibration. Two-dimensional (2D) image data from the Mar345 IP detector is converted to one-dimensional (1D) intensity versus 2θ plots using the FIT2D program [6]. Accurate lattice parameters are refined by Rietveld refinements employing GSAS program [7].

2.7 EDX measurements

Energy dispersive X ray spectroscopy (EDX) measurements were carried out using FEI Quanta 200 scanning electron microscope to determine the elemental composition for $BaFe_{2-x}Co_xAs_2$ single crystals. The composition of $BaMn_2As_2$ single crystals and $Fe_{1-x}Ni_xSb_2$ polycrystals were determined by EDX measurements using Zeiss Supra 55 scanning electron microscope.

References

1. L. J. vander Pauw, Philips Res. Repts. **13**, 1 (1958)
2. Awadhesh Mani , A.Bharathi , V.S.Sastry , T.S. Radhakrishnan and Y.Hariharan, *ICEC18: Proc. 18th Int. Cryogenic Engineering Conf. 2000* ed K G Narayankhedkar (New Delhi: Narosa Publishing House), p 615
3. S. J Blundell "Magnetism in Condensed Matter", Oxford University press, p26 (2000)
4. W. Krause, G. Nolze, Powder Cell for windows, version 2.3 (1999)
5. Dayana Lonappana, N.V. Chandra Shekar, T.R. Ravindrana and P. Ch. Sahua, *Mat. Chem. Phys.* **120**, 65 (2010)
6. A. P. Hammersley, S. O. Svensson, M. Hansfland, A. N. Fitch, and D. Hausermann, *High Press. Res*. **14**, 235 (1996).
7. C. Larson and R. B.V. Dreele, ''*GSAS: General Structural Analysis System*,'' LANSCE, Los Alamos National Laboratory, 1994.

Chapter 3

Transport behavior in the Normal and Superconducting states of $BaFe_{2-x}Co_xAs_2$ under Magnetic field

Magnetoresistance(MR) measurements were carried out for field parallel and perpendicular to crystallographic c-axis of $BaFe_{2-x}Co_xAs_2$ *single crystals for Co fractions, x =0, 0.082, 0.117 and 0.143. Below and close to the structural transition, the x = 0.082 sample shows linear magneto-resistance characteristic of the presence of electron states with Dirac cone dispersion. Upper critical field* (H_{c2}) *has been determined using field dependence of the superconducting transitions measured up to 12T for B||ab and B||c. The anisotropy (γ) defined as* H_{c2}^{ab}/H_{c2}^{c} *shows an increase with increase of Co content and shows a peak close to* T_c*. The* $[dH_{c2}/dT]_{Tc}$ *normalized with the corresponding transition temperature* T_c*, decreases with increase of Co content for both the directions. The implications of the above results are discussed.*

This chapter pertains to the study of magneto resistance (MR) behavior in the spin density wave (SDW) and paramagnetic states of $BaFe_{2-x}Co_xAs_2$ single crystals. Detailed investigations of the upper critical field behavior for the application of field parallel and perpendicular to the *ab* plane for the superconducting crystals of the series are also presented. In real metals, as the electron moves in close orbits on the Fermi surface, the resistivity increases parabolically with field, before showing a saturation. Whereas, the latter does not occur if the electron moves in open orbits on the Fermi surface [1]. In the presence of multiple Fermi surfaces, the transport is dominated by the Fermi surfaces in which the electrons have high mobility. The expected MR in the presence of two carriers is described in the semi classical theory by [2]

$$\frac{\rho(H)-\rho(0)}{\rho(0)}=\frac{\sigma_1\sigma_2(\mu_1-\mu_2)^2B^2}{\sigma_1^2[1+\mu_2^2B^2]+\sigma_2^2[1+\mu_1^2B^2]+2\sigma_1\sigma_2[1+\mu_2\mu_1B^2]} \qquad (1)$$

where σ_i is the conductivity of the i th band (i = 1,2), while μ_i is the mobility of the charge carriers which is positive for holes and negative for electron charge carriers. This equation results in a positive MR with quadratic field dependence at low fields and tends to a constant value at high fields.

To understand the MR measurements in the $BaFe_2As_2$, we need to know its electronic structure, which we now present, based on Band Structure calculations and ARPES measurements [3, 4, 5]. $BaFe_2As_2$ is a semi-metal with the top of the hole bands centred around the Γ point of the Brilloiun zone, whereas the bottom of the electron bands lie at the cube edges viz., ‘X’ point of the Brilloiun zone. These result in concentric hole-like, cylindrical Fermi surfaces centered around the Γ point and cylindrical concentric electron like Fermi surfaces centred around the X point [3]. The resulting topology of the Fermi surface is such that large portions of these hole and electron Fermi surfaces can be translated into one another by a nesting wavevector $Q=(\pi, \pi)$ in reciprocal lattice units. This favours the formation of the SDW state, with a real space ordering of magnetic moments on Fe, leading to an anti-ferromagnetic order commensurate with the lattice [3]. In the SDW state, the Fermi surfaces undergo reconstruction on account of band down-folding, leading to much smaller Fermi Surfaces [6]; According to local density approximation (LDA) calculations, the $BaFe_2As_2$ parent compound has four closed Fermi-surface pockets in the AF reconstructed states, therefore one would need eight parameters (mobility and carrier density for each pocket) to characterize the transport properties, of which it has been shown that only the

Fermi surfaces corresponding to the Dirac cone states contribute to conduction [7]. This was also suggested based on angle dependence of the magnetic quantum oscillations in the SDW state of $SrFe_2As_2$ and $BaFe_2As_2$, where it has been shown that the measured small Fermi-surface pockets are Dirac nodal pockets arising from a Dirac dispersion [8]. With the addition of electrons or holes by chemical substitution in $BaFe_2As_2$, the electron and hole Fermi surfaces respectively expand leading to the violation of Fermi surface nesting and leading to the absence of the SDW transition [9]. Consequently, above the SDW transition, the conductivity has no contribution from states with Dirac cone distribution.

Quantum transport due to the Dirac cone states in the iron pnictide $BaFe_2As_2$ manifests as a linear variation in measured transverse magnetoresistance as a function of magnetic field at low temperatures, as shown by Huynh et.al., in single crystalline $BaFe_2As_2$, within the SDW regime[10]. This experiment [10] was motivated by an earlier work of Abrikosov [11] attempting to understand the large linear magneto-resistance variation seen on Bi metal. In this seminal paper he argued that the appearance of linear magneto-resistance is a new quantum transport phenomenon appearing in metals, or semimetals which have a small concentration of carriers along with a small effective mass [11]. Evidence for the presence of Dirac cone dispersion has been seen in several other Fe-As systems, viz., Ru doped $BaFe_2As_2$[12], Co,Ni and Cu doped $BaFe_2As_2$ [7] and oxy-arsenides, viz., $LaFe_{1-x}Ru_xAsO$[13] and PrFeAsO[14] in their SDW regime. Because of their very small effective mass, the Dirac Cone charge carriers have very high mobility and hence contribute to a high conductivity, leading to the large drop in resistivity characteristic of the SDW transition in these materials [10]. We examined the transverse magneto-resistance behaviour in the $BaFe_2As_2$ and doped $BaFe_2As_2$ crystals that have the SDW ground state and compare it with similar measurements in the paramagnetic regime of the superconducting samples. This is discussed in the first part of this chapter.

The second part of this chapter discusses the upper critical field behavior and its anisotropy in the superconducting $BaFe_{2-x}Co_xAs_2$ single crystals. In a superconductor, the application of an external magnetic field can destroy Cooper pairs in two ways: a) the orbital pair breaking due to the Lorentz force acting via the charge on the paired electrons, known as the orbital limit and (b) the Pauli paramagnetic pair breaking as a result of the Zeeman effect which aligns the spins of two electrons with the applied field, termed the Pauli paramagnetic limit. Werthamer, Helfand and Honenberg (WHH) systematically studied the temperature and impurity dependence of the upper critical field for the conventional type II superconductors, in which both Pauli paramagnetism and spin-orbital scatterings were taken into account [15]. These factors largely complicate the general expression of the temperature dependent $H_{c2}(T_c)$ and only some simplified cases are used in the analysis of the experimental results. In the absence of spin paramagnetic effect, the upper critical field is then restricted by orbital pair breaking effect. In the weak-coupling case the upper critical field is given by

$$H_{c2}(0) = -0.69 T_c \frac{dH_{c2}}{dT}|_{Tc} \qquad (2)$$

where $H_{c2}(0)$ is the zero temperature upper critical field and dH_{c2}/dT is the derivative of the H_{C2} versus temperature at the critical temperature T_C. In the extreme Pauli limiting case, superconductivity is suppressed in a magnetic field when the spin polarization energy exceeds the superconducting condensation energy and the upper critical field is given by

$$H_{c2}(0) = 1.84 T_c \qquad (3)$$

which also termed as the Chandrasekhar-Clogston limit [16, 17].

Estimations of $H_{c2}(0)$ from early experiments in 1111 Fe-As superconductors using the slopes near T_c and the weak coupling formula of the WHH model (Eq (2)) give a value as high as 100T-300T [17, 18, 19]. The scenario changed after high pulsed field measurements were carried out in the 1111 As superconductors [20]. $H_{c2}(0)$ measured from these investigations is ~70T, still sufficiently high for useful applications. Taking into account the multiband nature of the doped $BaFe_2As_2$, Gurevich et.al have been able to understand the complete temperature dependence of the H_{c2} in several of the Fe based arsenides [21, 22]. Here, we have studied the upper critical field behavior in single crystal samples of $BaFe_{2-x}Co_xAs_2$ for x = 0.082, 0.117 and 0.143 which belong to under doped, optimally doped and over doped regions of the phase diagram. Our aim in this study was to investigate the effect of Co composition on the H_{c2} behavior of $BaFe_{2-x}Co_xAs_2$. Since our measurements were carried out on single crystals of these compounds, our data is employed to obtain the upper critical field anisotropy.

The synthesis of the single crystals $BaFe_{2-x}Co_xAs_2$, has been described in detail in Chapter 2. Room temperature XRD measurements were carried out using Cu Kα radiation using Bragg-Brentano geometry. Lattice parameters have been evaluated using STOE software. Resistivity measurements were carried out in the home built exchange gas cryostat form 4.2 to 300 K. Temperature dependent magnetization measurements were carried out using vibrating sample magnetometer to check for bulk superconductivity. Magneto resistance measurements were carried out using exchange gas cryostat from 0 to 12 T.

3.1 Structural Characterization of $BaFe_{2-x}Co_xAs_2$

The room temperature powder X-ray diffraction patterns of $BaFe_{2-x}Co_xAs_2$ obtained from STOE X-ray diffractometer for nominal compositions x_{nom} = 0.0, 0.1, 0.15 and 0.2 are shown in Fig 3.1. The diffraction peaks of all the samples could be indexed to tetragonal $ThCr_2Si_2$ type structure with space group symmetry *I4/mmm* (space group number 139). Small impurity peaks corresponding to FeAs have been observed for x_{nom} = 0.15 and 0.2. The impurity peaks could be due to inadvertent contamination arising from second phase particles present in the cooled melt. From the composition dependent XRD patterns, the unit cell parameters were

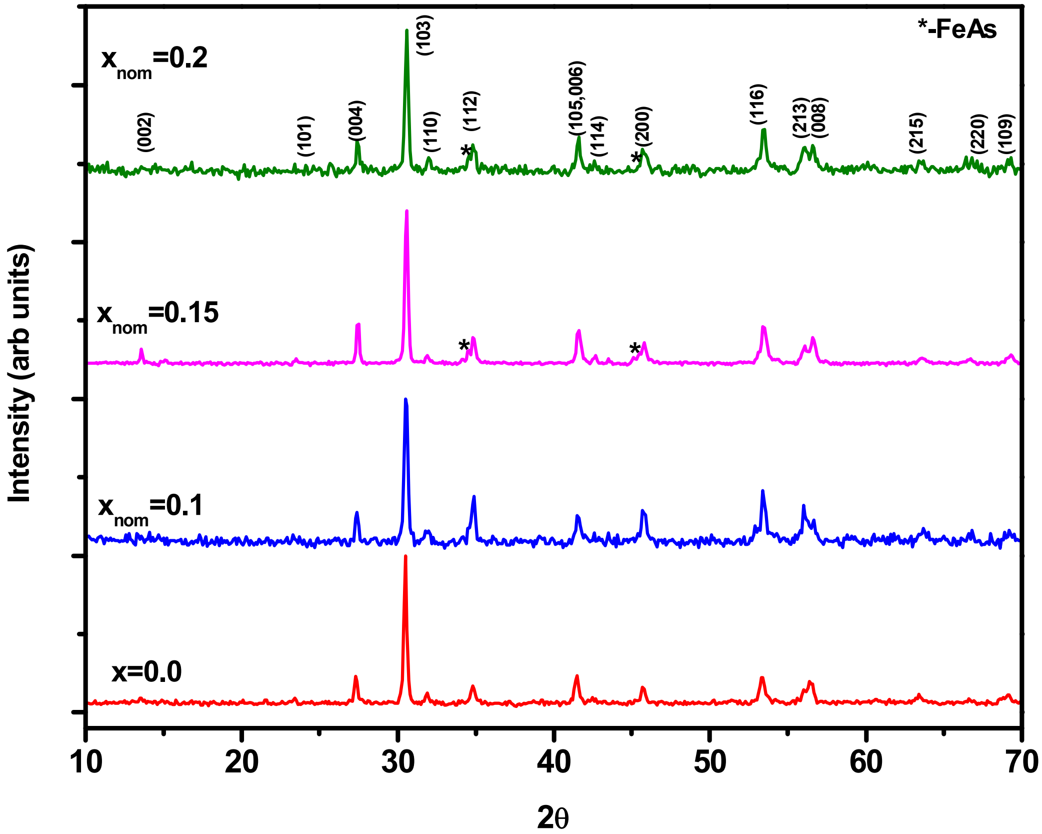

Figure 3.1: XRD patterns for powder $BaFe_{2-x}Co_xAs_2$ samples, indexed to *I4/mmm* symmetry. The intensity is normalized to the maximum value. For successive changes in Co fraction, the XRD patterns are shifted along the intensity axis for clarity.

refined using STOE software. The tetragonal lattice constants *a* and *c* obtained from the refinement for the pristine compound are 3.9652(4) Å and 13.0170(8) Å. The volume of the unit cell is 204.67 Å^3. These values are comparable with the reported lattice parameters and unit cell volume of $BaFe_2As_2$ [23, 24].

Figure 3.2 shows the variations of the lattice parameters *a* and *c* and unit cell volume *V* with Co composition. The lattice parameters *a* and *c* and unit cell volume *V* systematically decrease with increase of $x_{nom.}$ The decrease in the lattice parameter *c* is larger as compared to the decrease in *a*. Since Co atom has smaller radius as compared to Fe, substitution of Co

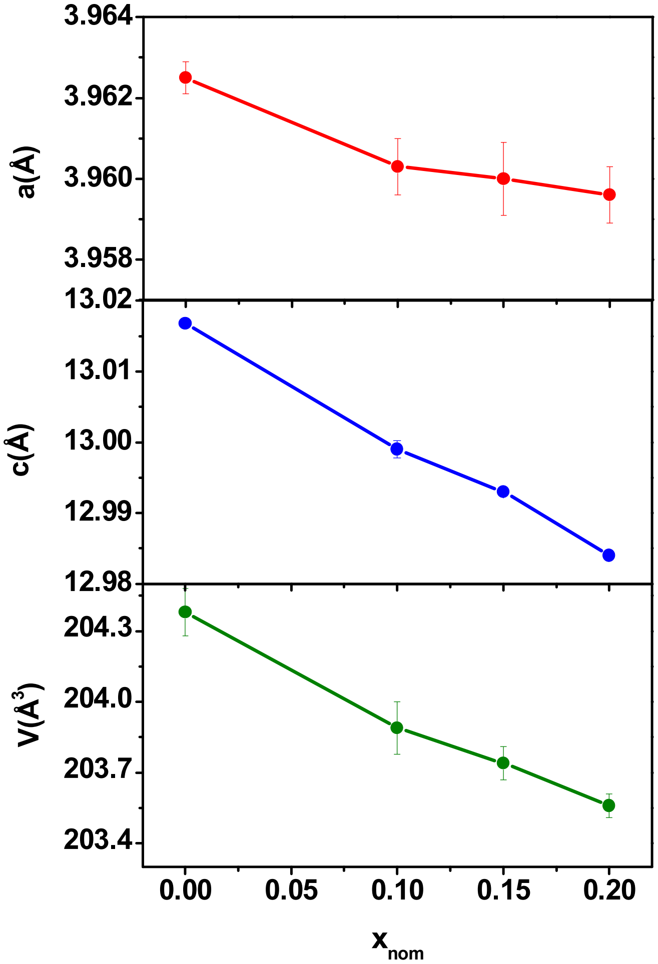

Figure 3.2: The variation in lattice parameters and cell volume with Co fraction of $BaFe_{2-x}Co_xAs_2$ samples.

atom at the Fe site is equivalent to applying chemical pressure resulting in the observed decrease in lattice parameters. Table 1 lists the lattice constants *a* and *c* and unit cell volume *V* for different x_{nom}. The actual content of Co has been determined using reported Co composition correlation with the unit cell volume [24]. Fig 3.3 shows the variation of unit cell volume as a function of Co composition as reported by Ni et.al [24] along with our data. The estimated Co compositions for x_{nom} = 0.1, 0.15 and 0.2 by this comparison are respectively x_{xray} = 0.079, 0.109 and 0.145.

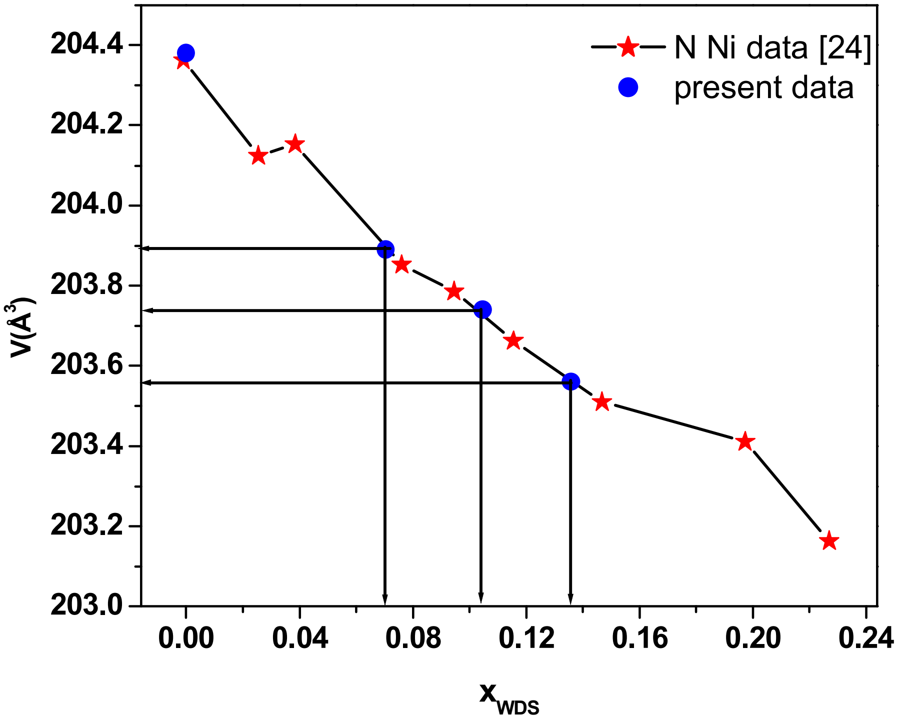

Figure 3.3: The variation of unit cell volume with Co fraction of $BaFe_{2-x}Co_xAs_2$ samples as repoted by Ni et.al [24]. Blue solid circles belong to our present data. Actual composition x_{xray} has been determined using this unit cell volume and Co composition correlation.

Energy dispersive X ray spectroscopy (EDX) measurements were also carried out using a FEI Quanta 200 scanning electron microscope, to determine the actual composition of the Co for all the single crystal compositions. The EDX spectra were taken at three different spots on each of the single crystals for all compositions. Fig 3.4 shows representative EDX patterns for x_{nom} =0.1, 0.15 and 0.2. The spectra show peaks corresponding to elements, Ba, Fe, Co and As. No other elements were detected, indicating the absence of contamination from crucibles during the synthesis.

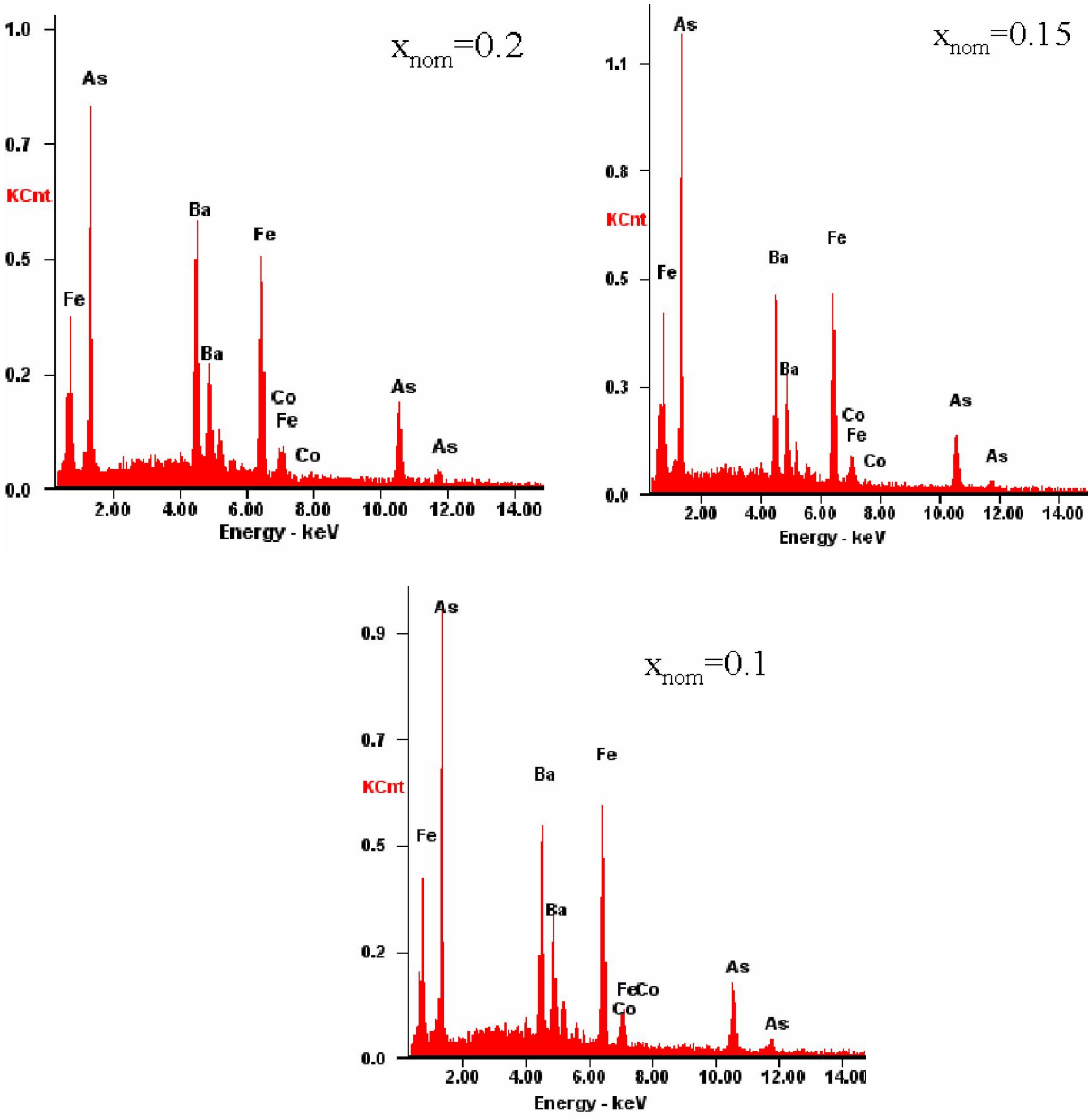

Figure 3.4: Energy dispersive X-ray spectra taken on single crystals of $BaFe_{2-x}Co_xAs_2$ for x_{nom} =0.2, 0.15 and 0.1, showing peaks corresponding to Ba, Fe, Co and As

x_{nom}	a (Å)	c (Å)	V (Å^3)	x_{xrd}	x_{EDX}	x_{ave}
0.1	3.9603(8)	12.999(11)	203.89 (11)	0.079	0.084	0.082
0.15	3.9600(9)	12.993(5)	203.74 (7)	0.109	0.125	0.117
0.2	3.9596(7)	12.984(6)	203.56 (5)	0.145	0.141	0.143

Table1: Structural properties and compostion details of the $BaFe_{2-x}Co_xAs_2$ single crystals. x_{xray} and x_{EDX} are the estimated Co content based on unit cell volume data reported in Ni *et al.* [24] and EDX results. x_{ave} is the average value of x_{xray} and x_{EDX}.

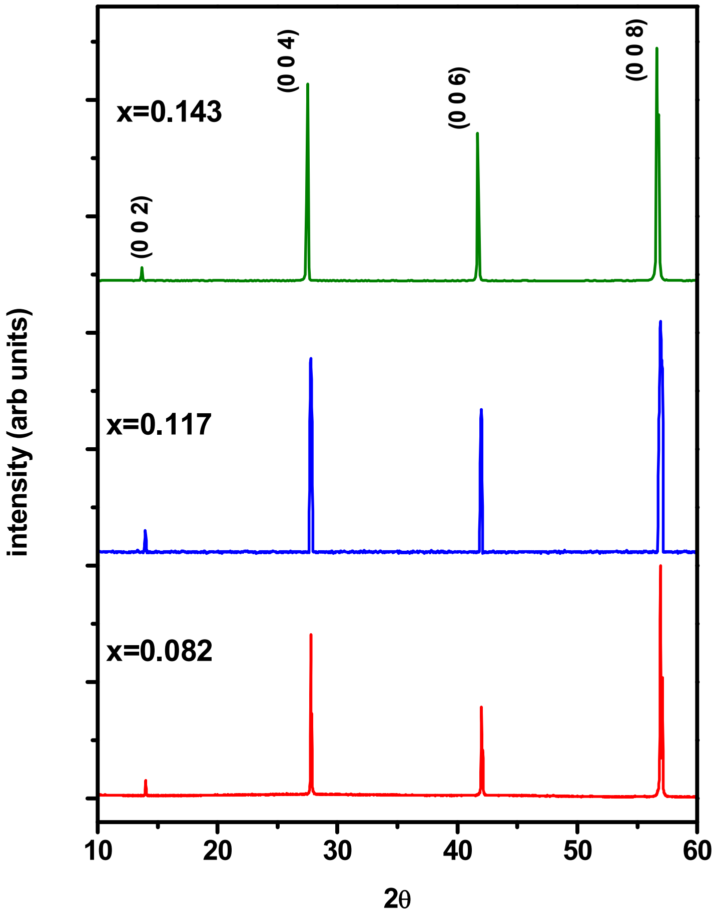

Figure 3.5: XRD patterns for single crystals of $BaFe_{2-x}Co_xAs_2$ samples for X-rays incident on the flat surface of the crystal, indexed to *I4/mmm* symmetry. The intensity is normalized to the maximum value. For successive Co fraction, the XRD patterns are shifted along the intensity axis for clarity.

The estimated Co compositions from these measurements are x_{EDX} = 0.084, 0.125 and 0.141 respectively. These values are comparable with x_{xray} values obtained from lattice volume versus Co composition correlation. The average values (x_{ave}) of Co fractions estimated from the cell volume (x_{xray}) and EDX results (x_{EDX}) for x_{nom} = 0.1, 0.15 and 0.2 are 0.082, 0.117 and 0.143. These x_{ave} values will be used to represent the samples in the remainder of this chapter.

Figure 3.5 shows X-ray diffraction measurements carried out at room temperature on single crystals of $BaFe_{2-x}Co_xAs_2$. The x-rays were made to fall on the flat faces of the crystals. The X-ray pattern shows only diffraction peaks corresponding to (0 0 *l*) planes for all the three samples. This provides evidence that the crystallographic *c*-axis of the single crystals is perpendicular to the flat surface of the crystals

3.2 The SDW and SC transitions in $BaFe_{2-x}Co_xAs_2$ crystals

Figure 3.6 shows the the normalized in-plane resistivity behaviour seen in the pristine single crystalline sample. The current and voltage leads were made with 50 micron copper wires attached to the four corners of the single crystal on the ab plane. The resistivity shows positive temperature coefficient of resistance in the temperature range 4.2 to 270 K. The sharp drop in resistivity at 138 K signals the occurrence of the SDW transition. At temperatures above this transition the resistivity shows a nearly linear monotonous increase. The variation of normalized electrical resistivity ($\rho(T)/\rho(300\ K)$) measured for $BaFe_{2-x}Co_xAs_2$ crystal with, x = 0.082 in the temperature range 4.2 to 300 K is shown in Fig 3.7. The resistivity shows positive temperature coefficient in the temperature range 75 to 300 K and varies linearly in this region. Below 75 K, resistivity increases, but shows a slope change at 65 K. This anomalous temperature dependent resistivity is associated with structural and spin density wave (SDW) transitions for this Co fraction typically observed in the under doped region of

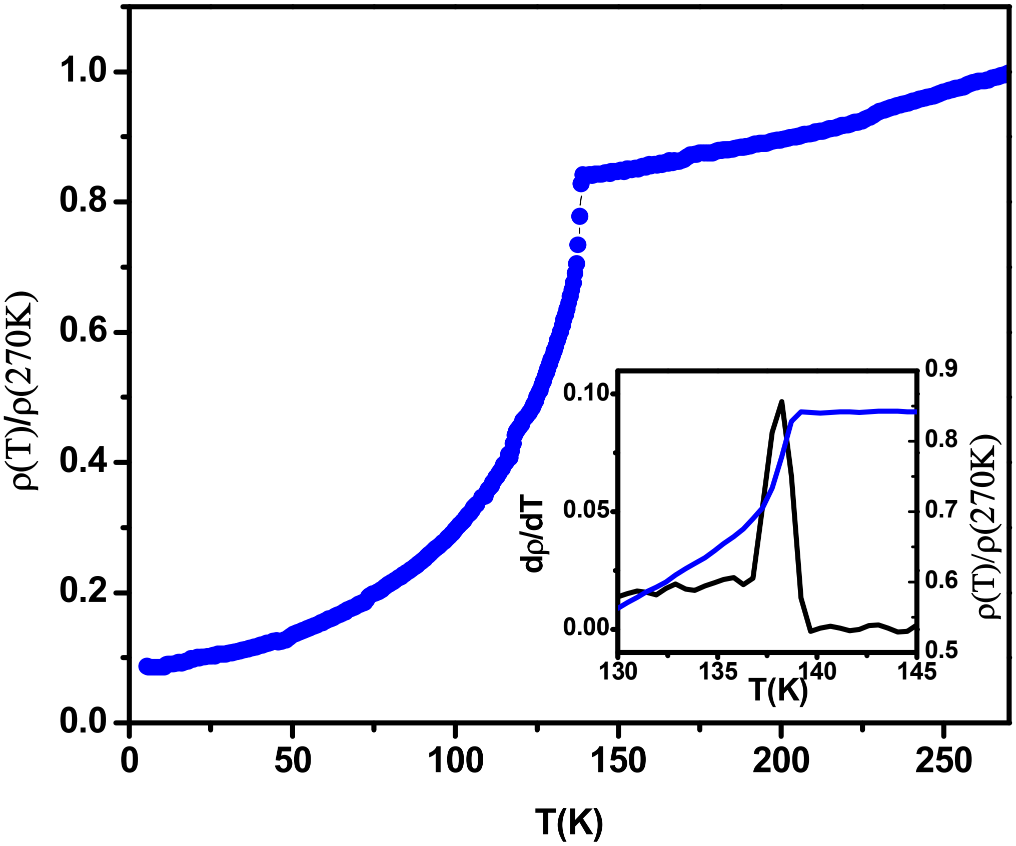

Figure 3.6 : The normalized resistivity as a function of temperature in pristine single crystals of $BaFe_2As_2$. Inset shows the derivative of resistivity. The single peak is associated with the concurrent structural and SDW transitions.

the phase diagram [24, 25]. The dρ/dT versus temperature plot is shown in the top inset of Fig 3.7. Unlike in the pristine sample, dρ/dT in the Co doped sample shows two anomalies, associated with structural (T_{str}) and magnetic (T_{SDW}) transitions and they are found to be 75 K and 62 K respectively. The bottom inset of Fig 3.7 shows the enlarged view of normalized resistivity around the superconducting transition. The transition temperature T_c is determined

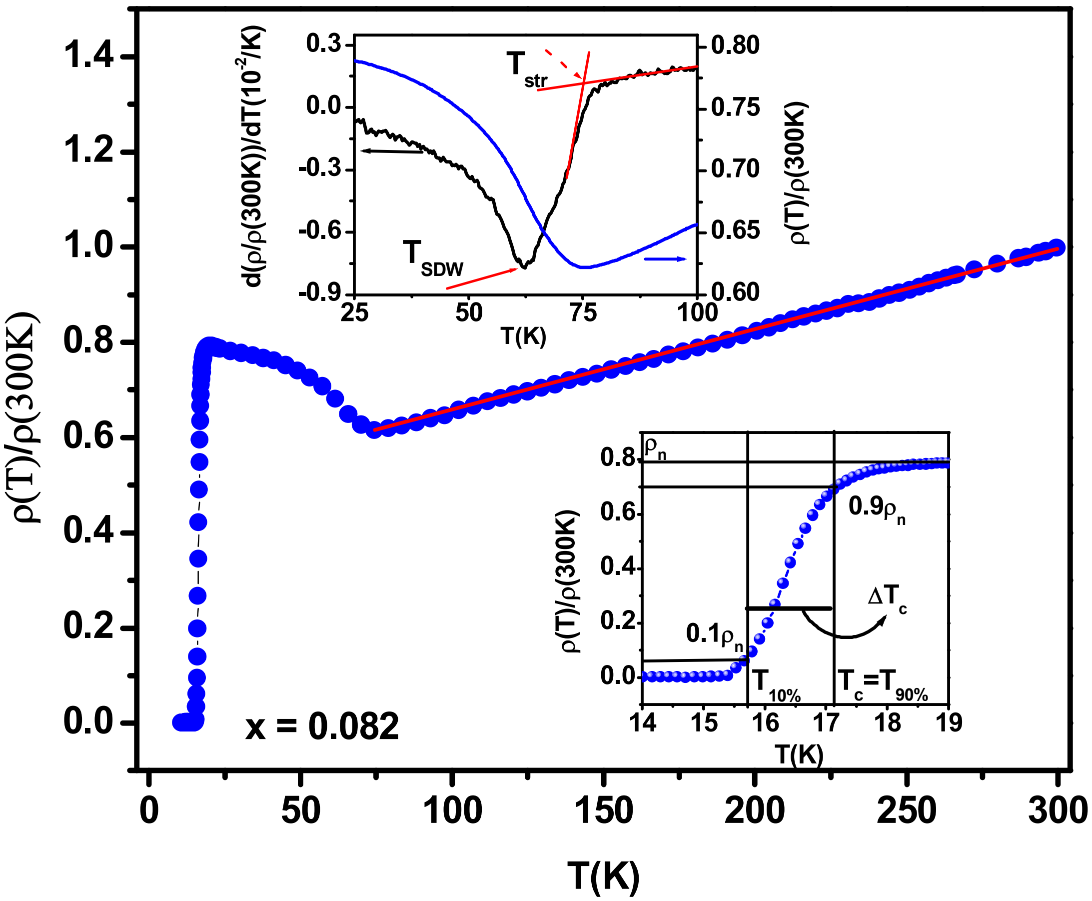

Figure 3.7: Normalized electrical resistivity versus temperature for x = 0.082.The top inset shows the temperature derivative of normalized resistivity versus temperature and enlarged view of resistivity around the SDW transition. The bottom inset shows expanded view of resistivity around the superconducting transition.

by 90% criterion, that is, the temperature corresponding to the point where the resistivity falls to 90% of its normal state value (ρ_n). The transition width (ΔT_c) is determined by the difference between $T_{90\%}$ and $T_{10\%}$. The T_c and ΔT_c obtained using these criterions are 17.1 K and 1.1 K respectively. The T_{str} and T_{SDW} values are comparable with reported values [24, 25] but the value of T_c is slightly larger compared to reported value of ~15 K [24, 25].

The temperature variations of the normalized resistivity for x = 0.117 and 0.143 are shown in Fig 3.8. It is evident from Fig.3.8 that both the samples show positive temperature

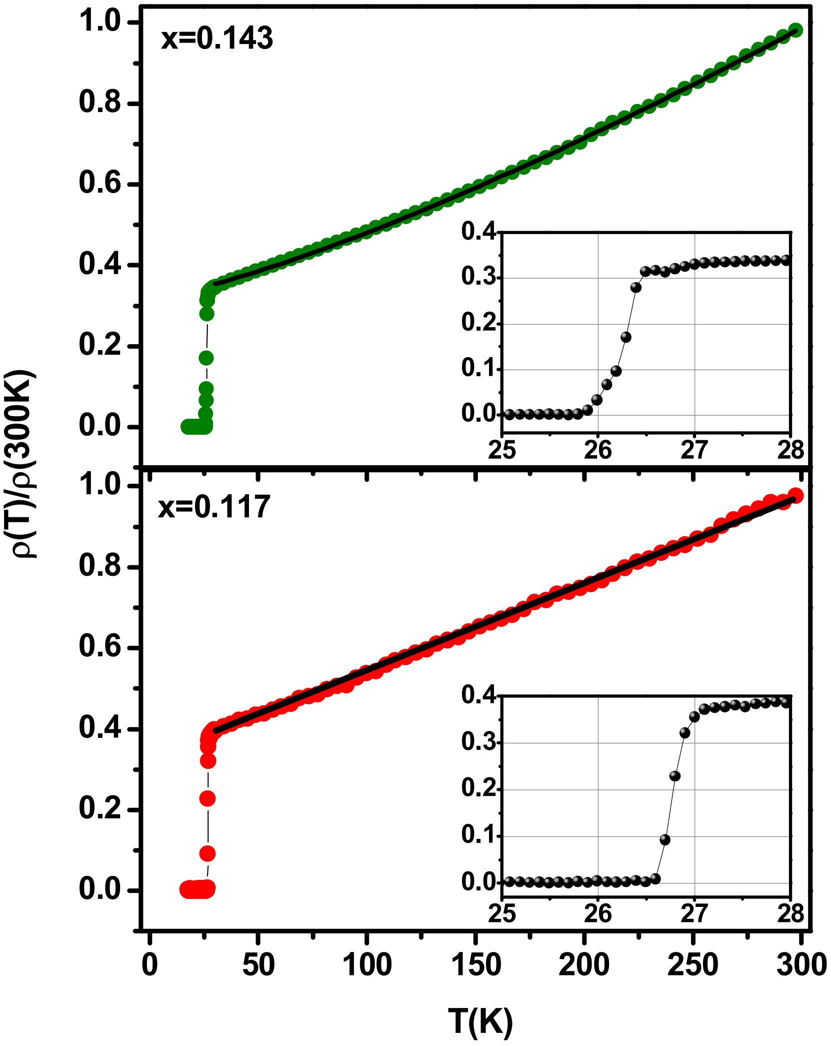

Figure 3.8: Normalized resistivity versus temperature of $BaFe_{2-x}Co_xAs_2$ for x = 0.117 and 143 The black solid lines are fits to T^n. n=1 for x = 0.117 and 1.3 for x = 0.143. The insets in each graph show enlarged view of resistivity around the superconducting transition.

coefficient of resistivity in their normal state. For x = 0.117, the resistivity shows linear decrease as the temperature reduces from 300 K until T_c. In the x = 0.143 sample the resistivity could be fitted to a powerlaw~ $T^{1.3}$. Such non linear resistivity behaviour has been reported in the over doped regime of phase diagram for Co doped $BaFe_2As_2$ [24, 25]. T_c and ΔT_c were determined using similar criterion as that of x =0.082. T_c values obtained for these two samples are respectively 26.9 K and 26.4 K. Their transition widths are similar and are of the order of ~0.4 K. The transition temperatures obtained in the present single crystals are ~ 2-3 K higher than the most of the reported T_c values of $BaFe_{2-x}Co_xAs_2$ system [24-27]. Such increased T_c was also observed for crystals grown by flux method [28]. Our measurements were repeated on three different crystals for all the three compositions. The T_C values are consistent to within 0.5 K for each of the compositions investigated, implying the reliability of our data. The narrow widths of the transition temperatures in the present samples probably indicate that the quality of the single crystals is very good.

3.3 Magnetization measurements

To confirm bulk superconductivity in the samples, magnetization measurements were carried out in a commercial (CRYOGENIC, UK) vibrating sample magnetometer from 4 to 30 K. Fig 3.9 shows normalized magnetization for all the samples of $BaFe_{2-x}Co_xAs_2$ measured in zero field cooling (ZFC) and field cooling (FC) protocols with applied field of 100 Oe. ZFC measurements were carried out by cooling the sample in the absence of field from 300 K to 4K after which measuring magnetic field was applied and magnetization was measured by warming the sample. FC measurements were carried out by cooling the sample in the presence of the measuring field from 300 to 4K and magnetization was measured by warming the sample. FC magnetization is lesser than ZFC value due to flux pinning. The T_c is identified as the temperature at which the ZFC and FC magnetizations separate from each other. The T_c obtained by this criterion for x = 0.082, 0.117 and 0.143 are 16.7, 26.2 and 25.9 K respectively. Lack of definite shape of the crystals precluded the determination of demagnetization factor required for the estimation of correct magnetization signal in the superconducting state. Alternatively we compared the superconducting volume fraction of the samples by comparing with the signal in Pb of similar weight. The signals in the samples are ~ 99% when compared with the signal in Pb indicating their bulk superconducting nature.

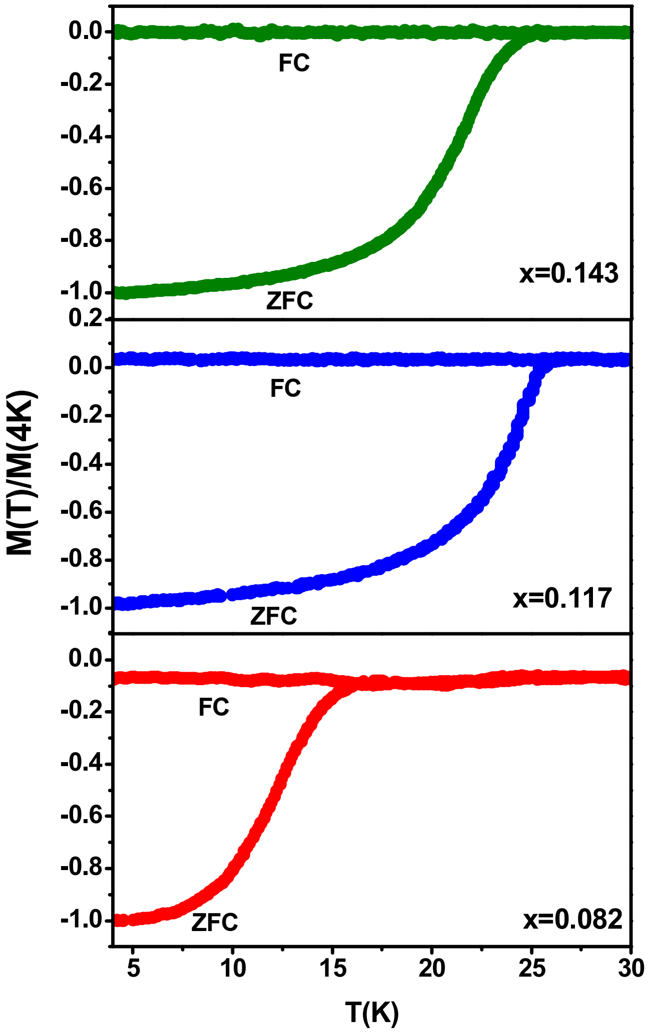

Figure 3.9: Normalized magnetization versus temperature of $BaFe_{2-x}Co_xAs_2$ for x = 0.082, 0.117 and 0.143, FC and ZFC modes of measurement are indicated.

Figure 3.10 depicts the well established phase diagram of $BaFe_{2-x}Co_xAs_2$ system [24, 25], showing the spin density wave, superconducting and paramagnetic regimes. The data shown by full circles are the transitions obtained from data shown in the earlier sections on the present samples. It is evident from the figure that the transition temperatures obtained from the present results are consistent with those reported in literature [24, 25], excepting for the fact that the superconducting transition temperatures are larger. It has been reported that the superconducting transition temperatures for flux grown single crystals in the similar system $CaFe_{2-x}Co_xAs_2$ increase in annealed samples [29]. This suggests that the present method of synthesis is better than cooling from excess flux.

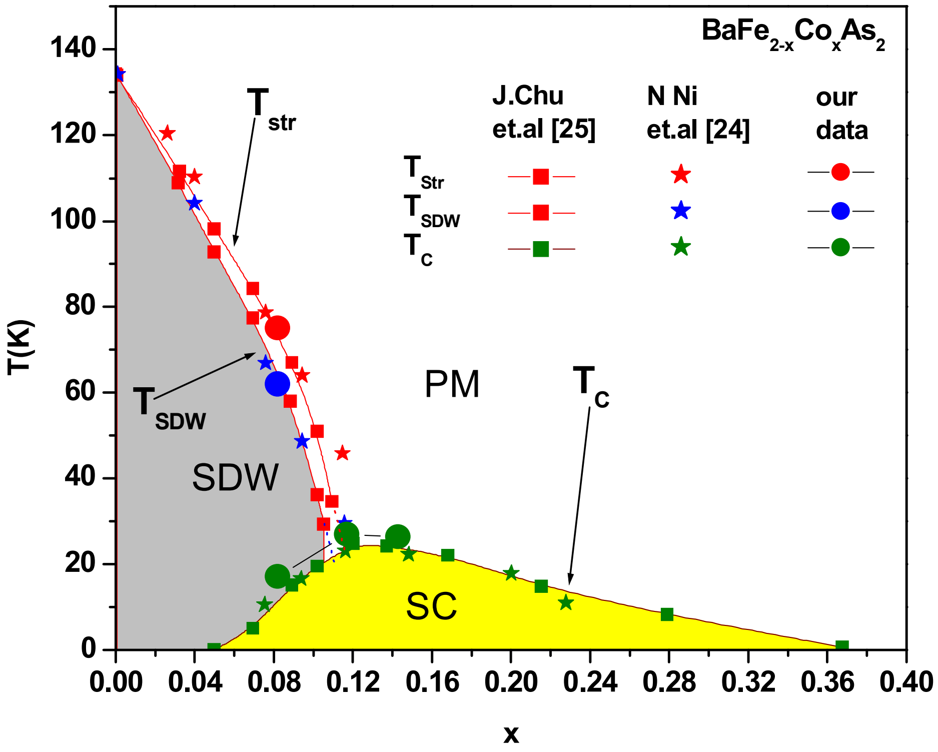

Figure 3.10 :The phase diagram of $BaFe_{2-x}Co_xAs_2$ as obtained from Ref[24, 25]. The T_{str}, T_{sdw} and T_c represent the structural magnetic and superconducting transitions. The data shown as solid circles represent the data obtained from measurements discussed in the present chapter. The paramagnetic(PM), superconducting (SC) and SDW regimes are indicated.

3.4 Magnetoresistance

3.4.1 Magnetoresistance in SDW regime of $BaFe_2As_2$ crystals

Figure 3.11 shows the resistivity versus temperature in the range 4.2 to 300 K for polycrystalline $BaFe_2As_2$ at 0 and 6 T magnetic fields. The steep fall in the resistivity of the sample seen at 140 K is associated with the SDW transition in the sample [24, 25]. The SDW transition in the polycrystal appears broader as compared to that seen in a single crystal [see Fig 3.6].

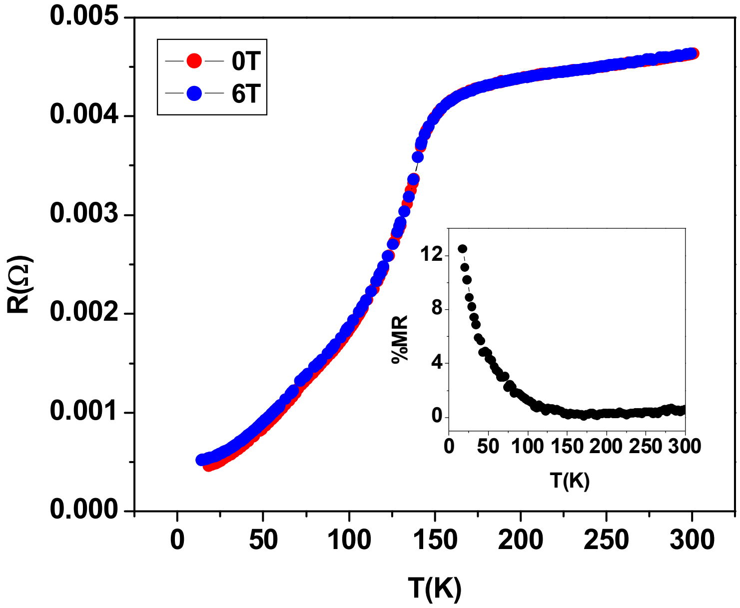

Figure 3.11: Resistance versus Temperature for polycrystalline $BaFe_2As_2$ at magnetic fields 0 and 6 T. The inset shows the variation of MR with temperature.

It is evident from Fig. 3.11 that the SDW transition temperature does not shift by the application of 6T field. The sample, however, shows a positive magneto resistance in the temperature range 4.2 to 300 K. The MR evaluated as (R(T,6T)-R(T,0T))/(R(T,0T) (in %) increases with decrease of temperature as shown in the inset of Fig 3.11. Hall co-efficient measurement indicated that the number density of electrons decrease with decrease in temperature [10]. Despite the decrease in the number density of electrons the fall in resistance in $BaFe_2As_2$ can only arise if the mobility of carrier shows a large increase with decrease in temperature, as shown in our earlier study [30]. It is now clear that the large decrease in resistivity seen in the SDW regime actually arises due to appearance of zero mass Dirac cone dispersed states on account of band down-folding.

Figure 3.12 a shows isothermal MR given by (R(H,T)-R(0,T))/(R(0,T)) measured on single crystals of $BaFe_2As_2$ at different temperatures in the SDW phase, in fields up to 10 T. At the outset it is evident from the figures that the MR is positive and is as large at ~14% at lowest temperatures of measurement viz., ~10 K. Interestingly, the MR above the SDW transition is much smaller and is only of the order of 0.2% (see inset in Fig 3.11). This large

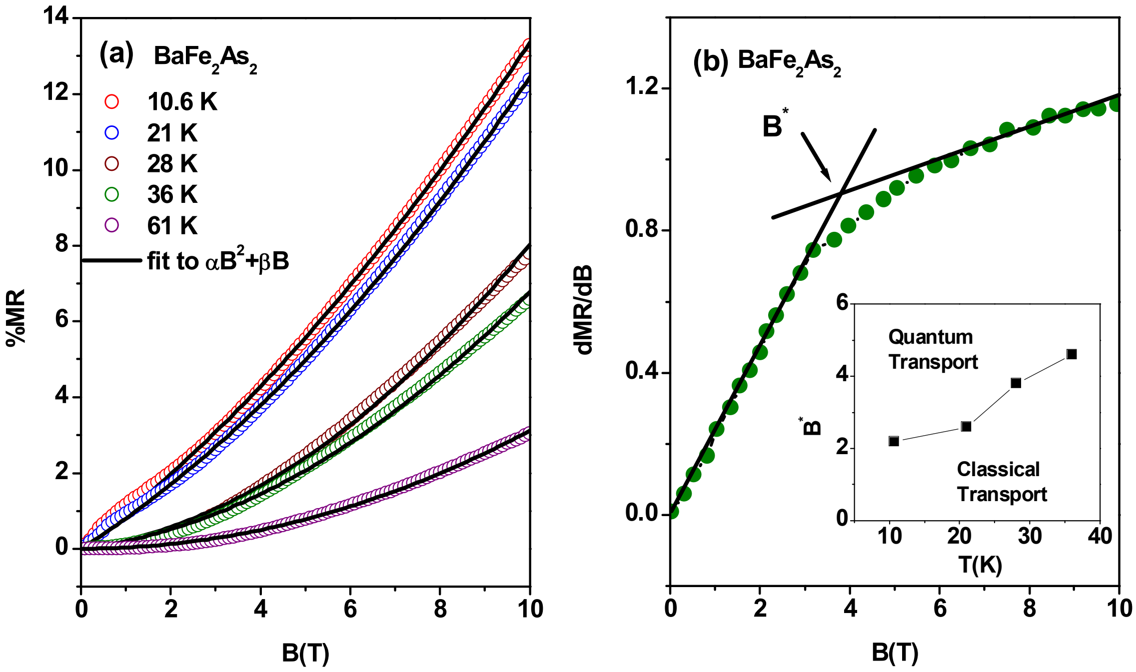

Figure 3.12 (a) Isothermal MR versus magnetic field at different temperatures for single crystal of $BaFe_2As_2$. Magnetic field is applied parallel to *c*-axis. Solid lines are a fit to a sum of parabolic and linear B components (b) The variation of first derivative of MR with field at T=28 K. the cross over from parabolic to linear transport behaviour occurs at a critical field of B*. The latter obtained for different temperatures are shown in the inset.

difference implies that very large changes occur in the nature of carriers across the SDW transition. It is clear from the MR versus field data, shown in Fig.3.12a, that at low fields the variation is parabolic, while it shows a linear B variation at higher fields. On careful perusal of the figure, it can be also seen that the cross over field from parabolic to linear behavior shifts to higher fields as the measurement temperature further increases. Following the analysis of the resistance versus field by Huynh et.al. [10], in Fig.3.12b the derivative of the measured MR versus B viz., dMR/dB versus B is plotted for one representative temperature. It is clear from Fig.3.12 b that the dMR/dB increases steeply at low fields with a large slope and crosses over to a small linear variation with a very small slope at a field marked as B*. This implies that the MR has a quadratic B variation at low fields, whose contribution gets lowered in magnitude as the field increases, to a linear variation in field, at B* [10].

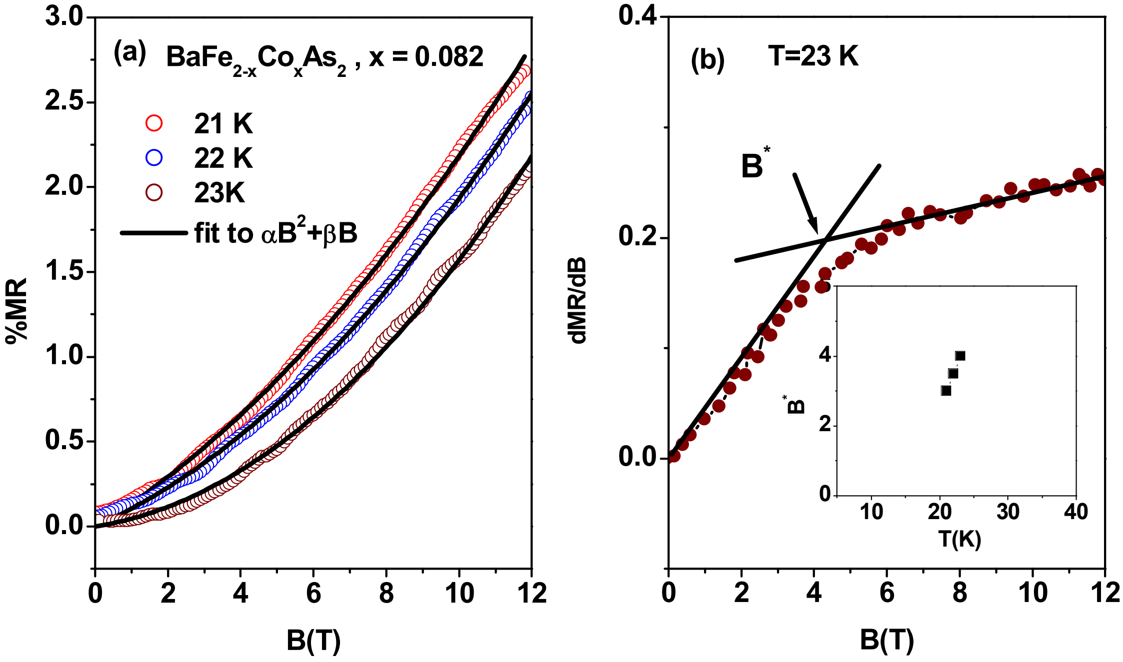

Figure 3.13 (a) Isothermal MR versus magnetic field at different temperatures for single crystal of Co substituted $BaFe_2As_2$. For single crystal sample, magnetic field is applied parallel to *c*-axis. Solid lines are a fit to a sum of parabolic and linear B components. The right panel (b) shows the cross over from parabolic to linear transport behaviour at a critical field of B*. The latter obtained from different temperatures are shown in the inset.

The cross-over field B* as obtained from a similar analysis of all the other MR isotherms, shows an increase with increase of measurement temperature as shown in the inset of Fig.3.12b. Since B^* is the field that delineates the B^2 and B regimes of MR behavior, it is evident from the figure that quantum transport is seen for higher fields and lower temperatures. In Fig.3.13 we show similar experimental data in the Co doped sample which has the SDW transition at 62 K. Here the MR measurements are done in a limited temperature range since the SDW state is stabilized only of a small region of temperature for this composition (see Fig.3.7). It is evident from the figure that even in fields as large as 12T the magneto-resistance at about 20K is much smaller and is ~2.5% as compared to 12% seen in the pristine sample. From the inset of Fig.3.13b it is evident that the quantum transport is

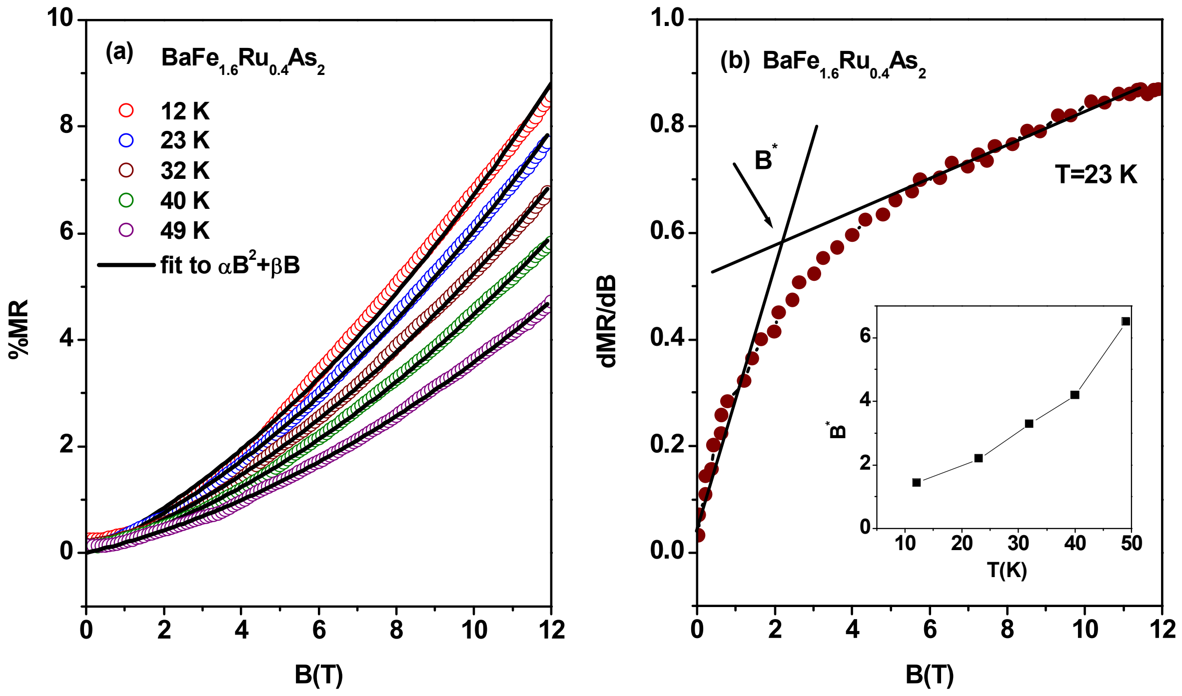

Figure 3.14: (a)Isothermal MR versus magnetic field at different temperatures for single crystal of Ru substituted $BaFe_2As_2$. For single crystal sample, magnetic field is applied parallel to *c*-axis. Solid lines are a fit to a sum of parabolic and linear B components. And Fig (b) shows the cross over from parabolic to linear transport behaviour at a critical field of B*. The latter obtained from different temperature measurements are shown in the inset.

stabilized only at much higher fields of ~ 4T in the Co doped samples at a temperature of ~23K, when compared to 2.5 T in the pristine sample at the same temperature. In order to establish the sensitivity of the MR behaviour to the electronic structure we now compare the MR data in pristine and Co substituted samples with similar data measured in a Ru doped single crystal. The isothermal MR measurements carried out in the Ru doped single crystal sample along with the B* analysis are shown in Figure 3.14. It is evident from Fig.3.14a that the linear contribution due to quantum transport is present in a wide temperature range for these samples, since is evident from Fig.3.14b, that the quantum regime persists over wide temperature and field range, even though the level of Ru substitution is large of ~20%. Since β and α (coefficients of linear and parabolic terms obtained from fits shown as solid lines in Fig 3.12 (a) to 3.14 (a)) represent contributions from quantum and classical transport in a given system, we compare in Fig.3.15, their variation with temperature in the pristine sample, Co substituted sample and the Ru substituted sample. It can be seen from the figure that the

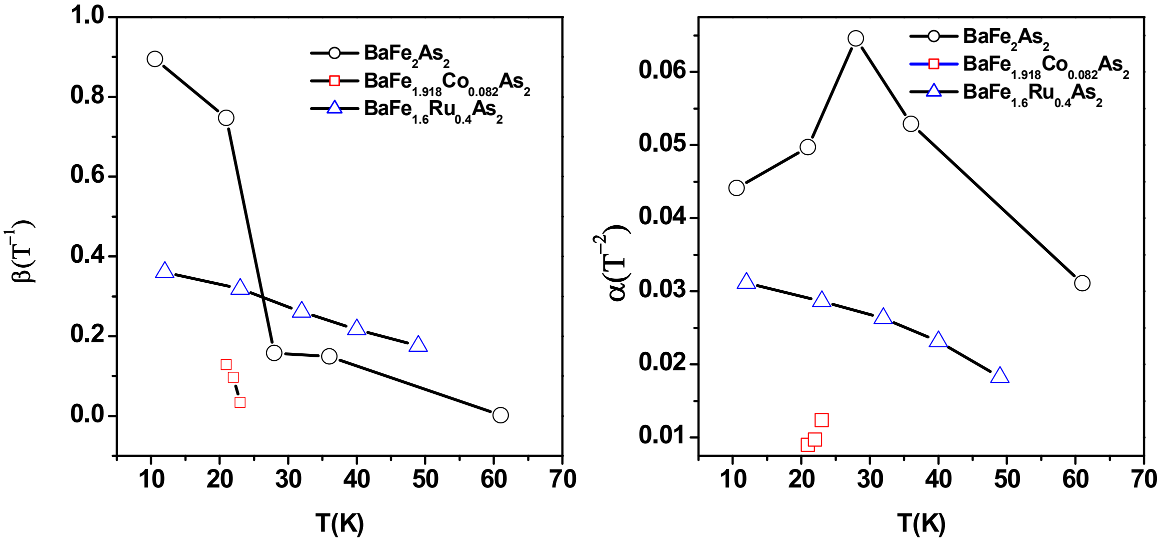

Figure 3.15: The variation of the co-efficients of the linear and quadratic terms with temperature for pristine, Co and Ru substituted samples, obtained from fits shown in Fig. 3.12(a) to 3.14 (a). β and α are in the units of Tesla^{-1} and Tesla^{-2}

contribution from quantum transport decreases with increase in temperature for all the samples. The coefficient of the B^2 term shows a non-monotonic variation with temperature in the pristine sample. This is expected, since it depends on various carrier mobilities and their number densities, which can have a complicated variation with temperature and chemical substitution [7]. Interestingly the β values which are the co-efficients of the B term, is also largest in the pristine sample when compared to both substituted samples. Since β is a measure of the average mobility of carriers, which is dominated by the transport from charge carriers with Dirac cone dispersion [7], the results from Fig.3.15 implies that Dirac cone states are most suppressed by Co substitution, rather than by Ru substitution in these arsenide crystals investigated. Future investigations in annealed crystals would be essential to obtain the quantitative information on the electronic changes brought about by these substitutions.

3.4.2. Anisotropic Magnetoresistance in the SDW state of $BaFe_{1.92}Co_{0.08}As_2$

Figure 3.16 shows the temperature dependent resistance for $BaFe_{2x}Co_xAs_2$ with x = 0.082 at different magnetic fields from 0 to 12 T in the temperature range 30 to 90 K. Fig 3.16a shows the resistance variation with temperature, when applied magnetic field direction is parallel to the *ab* plane of the crystal. As is seen from Fig. 3.16a, in this configuration, a decrease in the resistance is observed with increase of magnetic field. However, contrary to this, an increase in resistance is observed when the applied magnetic field direction is parallel to *c*- axis as shown in Figure 3.16b. In both the configurations, the structural (T_{str}) and spin density wave transitions (T_N) at 75 K and 62 K remain unaltered with the application of magnetic field up to 12T. Using the data shown in Fig 3.16, MR versus temperature was evaluated using (MR=ΔR/R ;[R(B)-R(0)]/(R(0)), where R(0) and R(B)

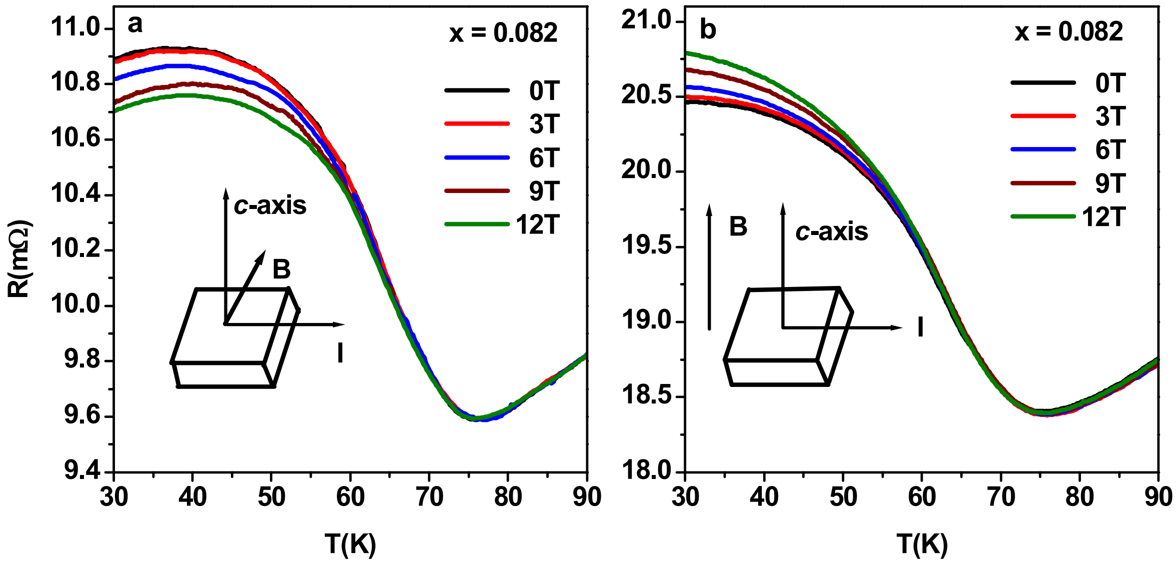

Figure 3.16: Resistance versus temperature for x = 0.082 of $BaFe_{2-x}Co_xAs_2$ at different magnetic fields B = 0, 3, 6, 9 and 12 T with (a) B || *ab* plane and (b) B || *c*-axis. The insets in the graphs show directions of the magnetic field and current used in the respective measurements.

are resistances measured in zero field and in the presence of field B respectively, at each temperature. Figure 3.17 shows the variations of observed magneto resistance as a function of temperature for magnetic field parallel to *ab* plane and *c*-axis. The insets in each graph show the isothermal MR variation with magnetic field at 22 K. From the Fig 3.17 it is clear that at a given temperature of 22K, the MR is negative when B is parallel to *ab* plane and positive when B is parallel to *c*- axis and the magnitude of MR systematically decreases with increase of temperature up to structural transition T_{str}, above which it goes to zero. The negative MR when B parallel to *ab* plane has been shown to arise due to detwinning in the presence of magnetic field [31]. From angular dependence MR of the applied field versus current, of Co doped $BaFe_2As_2$, in the SDW state, it was shown that the MR is negative when B is perpendicular to current direction and positive when current and applied fields are

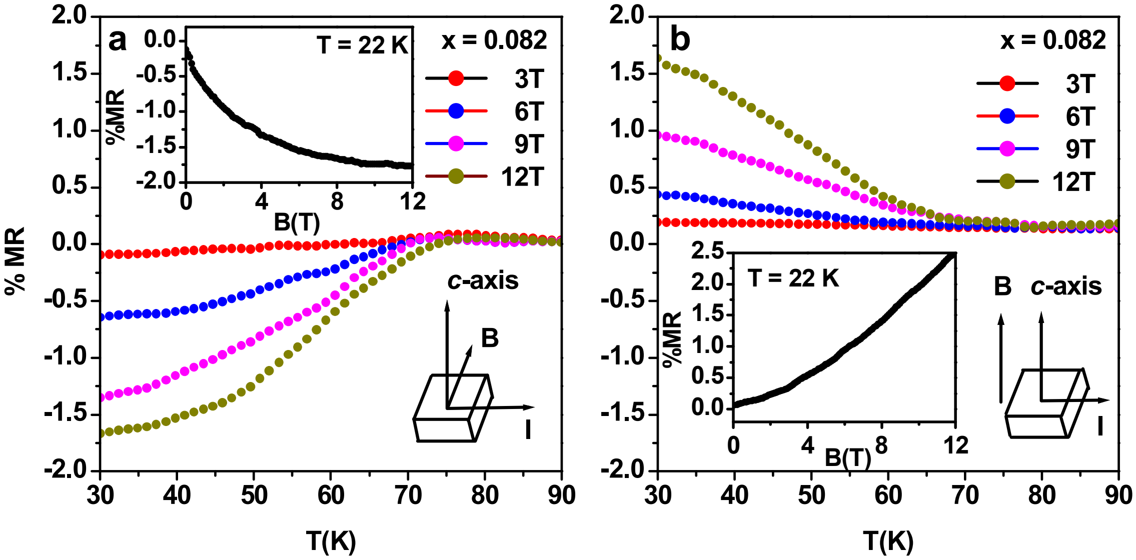

Figure 3.17: Magneto resistance versus temperature for x = 0.082 at different magnetic fields B = 3, 6, 9 and 12 T with (a) B || *ab* plane and (b) B || *c*-axis. The insets in the graphs show magneto resistance versus applied magnetic field at T = 22 K for the respective configurations.

parallel to each other. This was rationalized as follows: in the SDW state for the pristine $BaFe_2As_2$, the spins along the *b*-axis are ferromagnetically coupled and the spins along the *a*-axis are antiferromagnetically coupled [3], resulting in susceptibility anisotropic such that $\chi_b > \chi_a$ [31]. Therefore in a twinned crystal, for fields applied along the *a/b* axis, the twin domains with *b*-axis oriented along the field direction will be favoured [31] as illustrated schematically in Fig3.18. In the absence of field, Fig3.18a shows the schematic picture of arrangement of spins in a twinned single crystal. When a magnetic field is applied, twin boundary moves such that the ferromagnetic configuration is parallel to the field direction, as shown in fig.3.18 b. In the case of a measurement of magneto-resistance, in which current direction is perpendicular to B, field induced detwining ensures that the anitferromagnetic (AFM) aligned *a*-axis is parallel to current as shown in Fig 3.18b. Because of the in-plane electronic anisotropy where $\rho_a < \rho_b$ in these systems [32], a negative magneto-resitance, ensues. Contrary to this, when current is parallel to field, positive MR results because the larger resistive (ρ_a) ferromagnetic

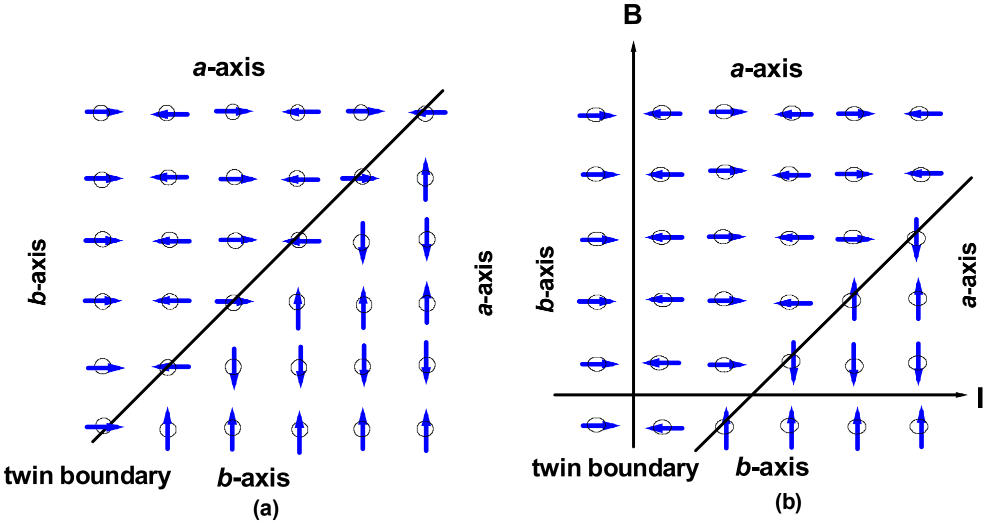

Figure 3.18: Schematic picture of arrangement of spins in a twinned single crystal in the absence of field (a) and in the presence of field (b) for $BaFe_{2-x}Co_xAs_2$ in the orthorhombic phase. When B and I are perpendicular to each other, magnetic field induced detwinning results antiferromatic configuration parallel to current as shown in (b)

(FM) configuration aligns parallel to current direction. Because our measurement configuration pertains to current being perpendicular to magnetic field we observe negative MR as shown in Figure 3.17a. In contrast when B is parallel to *c*-axis, detwinning of the orthorhombic structure does not occur and the positive magneto-resistance results, due to the earlier discussed pristine MR having a $\alpha B^2+\beta B$ dependence, arising due to contributions from classical and quantum transport, as described earlier.

3.4.3. Magnetoresistance in the paramagnetic state

We have also measured the magneto-transport in the paramagnetic regime (see phase diagram Fig 3.10) in the optimally and overdoped $BaFe_{2-x}Co_xAs_2$ crystals with x=0.117 and x=0.143. Figure 3.19 shows the variation of resistance with temperature in the range 30 to 90 K for x = 0.117 and 0.143. Figures 3.19a and 3.19c show the resistance variations for the application of magnetic field parallel to *ab* plane and Figures 3.19b and 3.19d show the resistance variations for magnetic field parallel to *c*-aixs. The insets in each graph show isothermal MR variation with magnetic field at T = 30 K for the respective samples. From the graphs it is apparent that there is no appreciable MR in their normal state, within the limitations of the measurement accuracy. The negligible MR in the paramagnetic state could be due to small mobility of charge carriers in the paramagnetic state of the system.

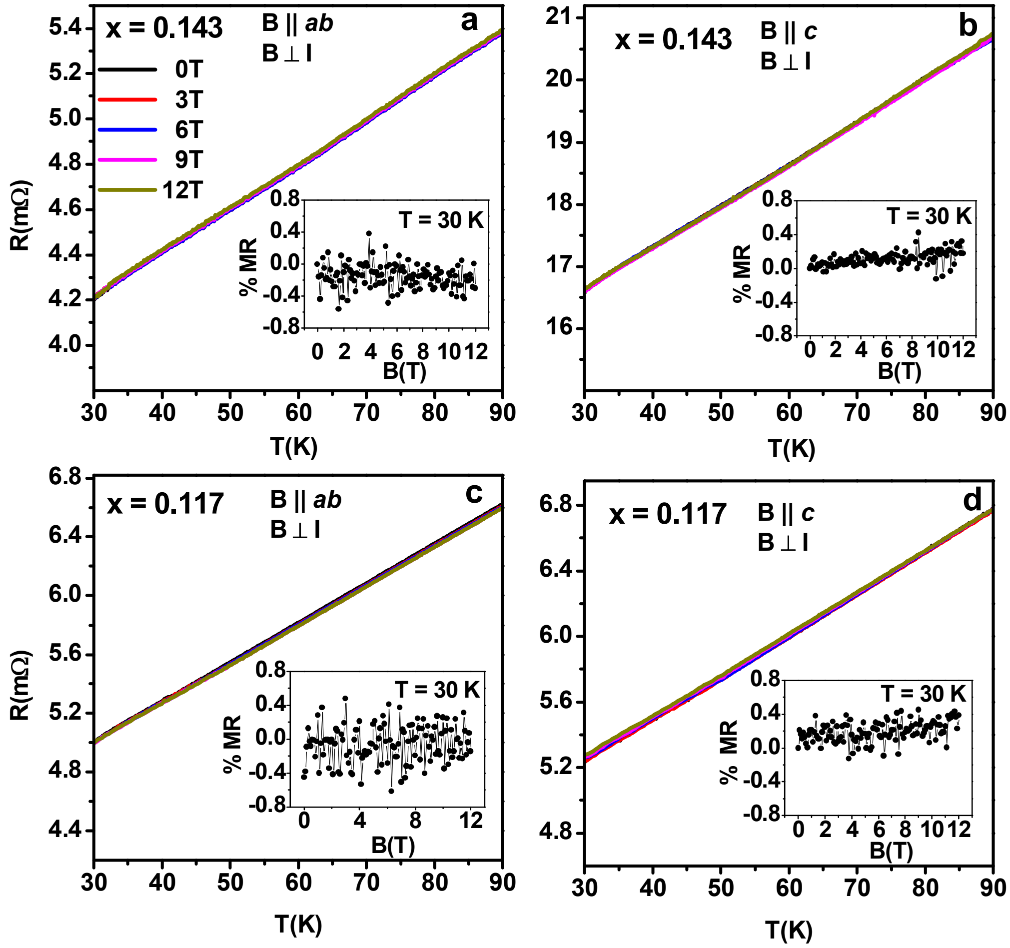

Figure 3.19: Resistance versus temperature for x = 0.117 and 0.143 samples at different magnetic fields B = 0, 3, 6, 9 and 12 T with B || *ab* plane and B || *c*-axis. The insets in each graph show the variation of magneto resistance (MR) with applied field (B) for the respective samples at T =30 K.

3.5 Upper Critical Field (H_{c2}) Behavior

The superconducting transition traces measured in external magnetic fields up to 12 T for $BaFe_{2-x}Co_xAs_2$ samples with x=0.083, 0.117 and 0.143 are shown in Fig.3.20.

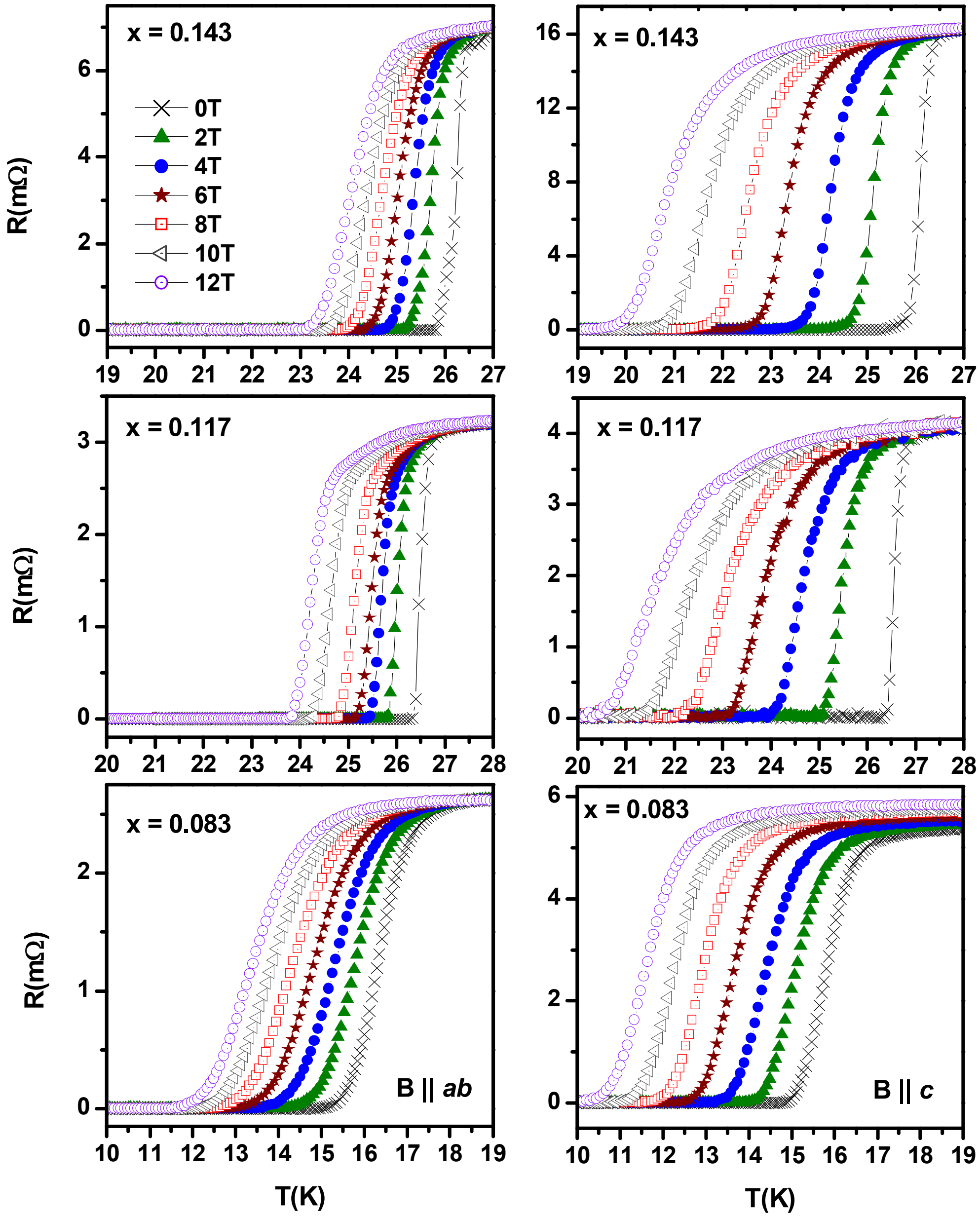

Figure 3.20: Resistance versus temperature for x = 0.082, 0.117 and 0.143 samples at different magnetic fields B = 0, 2, 4, 6, 8, 10 and 12 T with B || *ab* plane and B || *c*-axis.

The measurements were recorded in each of these samples for B || *ab* plane and B || *c*-axis. The current is applied perpendicular to the magnetic field in each of the cases. Upper critical field (H_{c2}) has been determined from the variation of the superconducting onset transition temperatures. From the graphs it is evident that the T_c systematically decreases with increase of B. Using the 90% criterion ($T_c = T_{R\,=\,0.9\,Rn}$), the upper critical field transition temperature is evaluated for each magnetic field (upper critical field at that temperature). The decrease in T_c is larger for applied field parallel to *c*-axis as compared to when it is parallel to *ab*-plane indicating anisotropy in upper critical field. Fig 3.21 shows the variation of upper critical field as a function of reduced temperature t (= T/T_c) for the three cobalt compositions with B || *ab* and B || *c*. As can be seen from Fig 3.21, for all the three cobalt compositions, H_{c2} exhibits almost linear temperature dependence in the measured field range for both B || ab and B || c although a weak positive curvature is observed near T_c. It has been shown that positive curvature is a signature of multi-band superconductivity and it has been observed in 1111 and 122 arsenide systems [17,18, 33, 34]. The slopes $[dH_{c2}/dT]_{Tc}$ obtained from the data for the three samples are listed in Table 2 and they are in very good agreement with previous reports [24, 34, 35]. $dH_{c2}/dT|_{Tc}$ increases for B || ab , where as it decreases for B || c.

	T_c (K)	ΔT_c(K)	$\lvert dH_{c2}/dT\rvert_{Tc}$ (T/K)	
			H || ab	H || c
0.082	17.1	1.1	5.3	3.3
0.117	26.9	0.4	5.4	3.1
0.143	26.4	0.4	5.7	2.8

Table 2: Superconducting parameters for $BaFe_{2-x}Co_xAs_2$ single crystals investigated

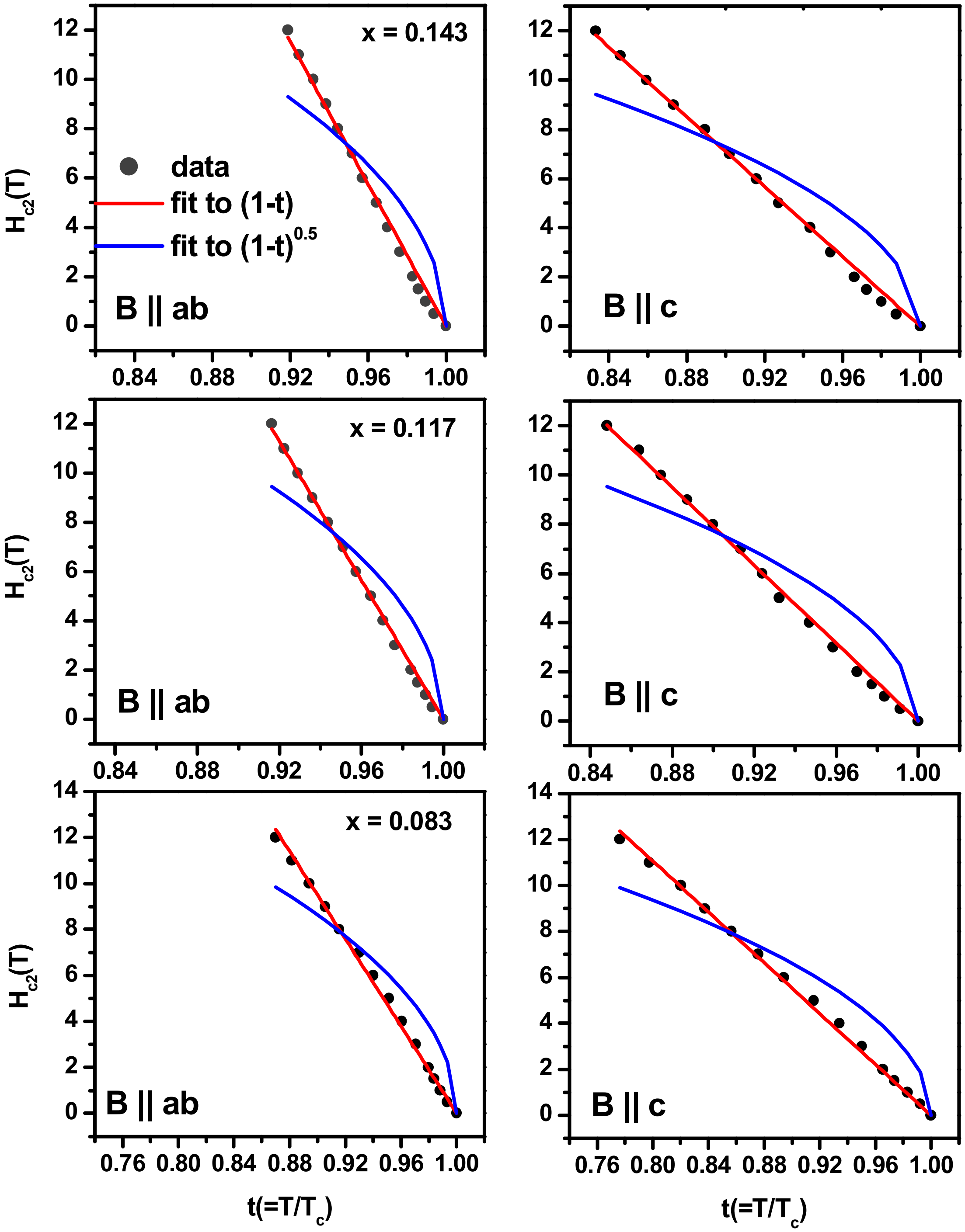

Figure 3.21: Upper critical field (H_{c2}) versus reduced temperature t (=T/T$_c$) of BaFe$_{2-x}$Co$_x$As$_2$ single crystals for x = 0.082, 0.117 and 0.143 with B || *ab* plane and B || *c*-axis. Red solid lines are fits to (1-t) and blue solid lines are fits to $(1\text{-t})^{0.5}$ for the respective samples.

Using the WHH formula H_{c2} (0) = $0.69T_c|dH_{c2}/dT|_{Tc}$, the evaluated values for B parallel to the *ab* plane, viz., H_{c2}^{ab} (0) for x = 0.082, 0.117 and 0.143 are respectively ~ 62 T, 100 T and 103 T respectively. Similarly the calculated values for B parallel to the c-axis, viz., H_{c2}^{c} (0) are respectively ~ 39 T, 57 T and 51 T. These values exceed the BCS paramagnetic limit ($H_P^{BCS}(0) = 1.84T_c$) values of 31 T, 49 T and 48 T for these compounds. But this BCS paramagnetic limit is without taking electron phonon coupling into account and it underestimates the actual paramagnetic limit. Including the electron phonon coupling $H_P \approx (1+\lambda)\ H_P^{BCS}$ [34, 36, 37], taking the λ value ~ 0.7 derived from first principle calculations [38] the paramagnetic limit values are ~ 53 T, 84 T and 82 T. These values exceed the orbital limit for B || *c*. So the upper critical field at T =0 K is limited by orbital effect for B || *c* and it is limited by paramagnetic effect for B || *ab* plane.

Gurevich explained the upper critical field behavior as a function of temperature for Fe-As superconductors using a model of two band superconductivity [21, 22]. According to which in the case of arsenide superconductors, where inter-band pairing is dominant over intra-band pairing the high temperature H_{c2} has two limiting forms. In the weak paramagnetic region, where orbital pair- breaking effect limits the upper critical field at a temperature, H_{c2} increases linearly with temperature as $H_{c2}\alpha(1-t)$, where t is reduced temperature (T/T_c). In the paramagnetic limited regime, H_{c2} varies as $\sqrt{1-t}$. From the Figure 3.21 it is clear the present data fit better with (1-t) for both B parallel to *ab* plane and *c*-axis configurations for all the three samples despite the weak positive curvature near T_c. The behavior is robust with respect to the T_c criterion employed to evaluate the H_{C2} versus reduced temperature curves.

The data could not be fitted well with $H_{c2}(t)\alpha\sqrt{(1-t)}$ as is evident from the discrepancy from experiment as shown in Figure 3.21

Assuming a two band model according to Gurevich [21, 22], H_{c2} in FeAs superconductors is sensitive to band parameters, in particular

$$\frac{1}{T_c}\left[\frac{dH_{c2}}{dT}\right]_{T_c}\alpha\left[\frac{1}{c_1v_1^2+c_2v_2^2}\right] \qquad (4)$$

where c_1 and c_2 are functions of inter and intraband coupling constants, and v_1 and v_2 depend on the Fermi velocity in the two bands. In the case of iron arsenides, since inter-band coupling is stronger compared to intra band coupling, $c_1 \approx c_2$ and

$$\frac{1}{T_c}\left[\frac{dH_{c2}}{dT}\right]_{T_c}\alpha\left[\frac{1}{v_1^2+v_2^2}\right] \qquad (5)$$

For the three Co compositions studied, $\frac{1}{T_c}\left[\frac{dH_{c2}}{dT}\right]_{Tc}$ has been calculated and the values are presented as a function of x in Fig 3.22. For comparison, the values obtained from the data of Ni *et al.* [24] and Kano *et al.* [34] are also shown in the same graph. An overall agreement between the $\frac{1}{T_c}\left[\frac{dH_{c2}}{dT}\right]_{Tc}$ values measured from our data and data from other groups is clearly evident from the figure. The value of $\frac{1}{T_c}\left[\frac{dH_{c2}}{dT}\right]_{Tc}$ decreases for both B || *ab* and B || *c* configurations as the cobalt content increases. $\frac{1}{T_c}\left[\frac{dH_{c2}}{dT}\right]_{Tc}$ is dependent on the Fermi velocities of electron and hole like bands as $(v_e^2 + v_h^2)^{-1}$. In $BaFe_{2-x}Co_xAs_2$ system, band structure calculations [3, 39] and angle resolved photo emission spectroscopy (ARPES) measurements [40, 41] revealed that with increase of Co concentration, the hole Fermi surface shrinks but the electron Fermi surface enlarges, and the effective mass of electron is smaller than that of the holes. Because of this, the value of electron Fermi velocity v_e^2 dominates over the hole Fermi velocity v_h^2. As electron Fermi velocity v_e increases with increase of Co content, $\frac{1}{T_c}\left[\frac{dH_{c2}}{dT}\right]_{Tc}$ could decrease as observed in Fig 3.22.

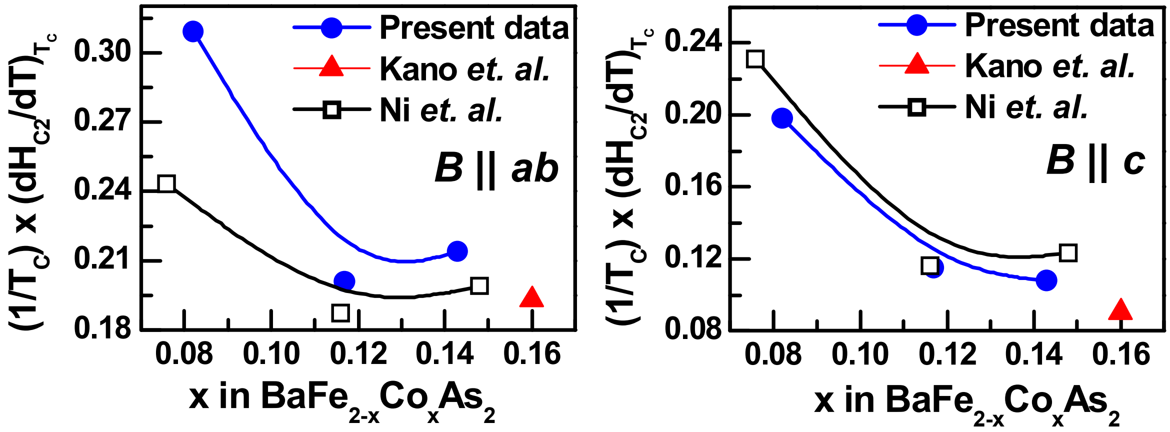

Figure 3.22: $\frac{1}{T_c}\left[\frac{dH_{c2}}{dT}\right]_{T_c}$ as a function of co concentration x for B || *ab* and B || *c* configurations. Circles show data from the present work. Squares and triangles are based on the data of Kano *et al* [34] and Ni *et al* [24].

3.6 Upper Critical Field (H_{c2}) Anisotropy (γ)

Figure 3.23 shows the upper critical field anisotropy (γ) defined as $\gamma = \frac{H_{c2}^{ab}}{H_{c2}^{c}}$, as a function of reduced temperature (t) for the three Co compositions. It is clear from the figure that the anisotropy systematically increases with increase of Co content. The values of γ for x = 0.082, 0.117 and 0.143 at t=0.95 are of the order of ~1.74, 1.92 and 2.18. These values are comparable to the values observed for $BaFe_{2-x}Co_xAs_2$ and $Ba_{1-x}K_xFe_2As_2$ [24, 27, 42] systems and is smaller compared to that in the oxyarsenide $NdFeAsO_{1-x}F_x$ system which is ~9-10 [18].

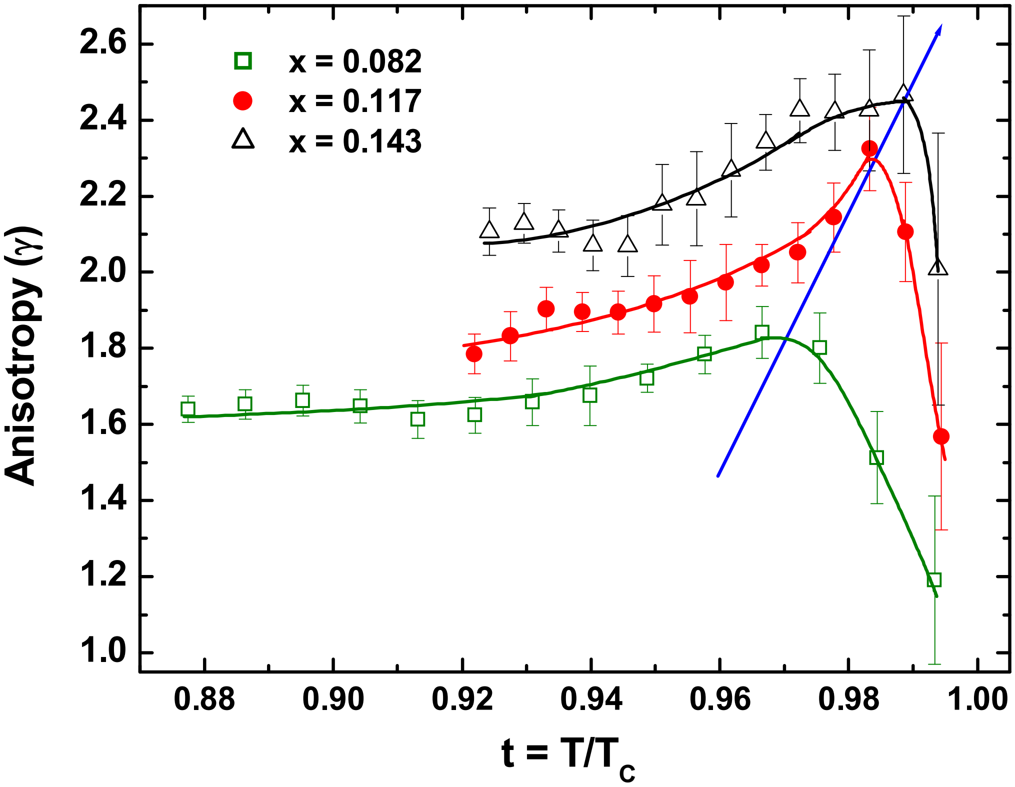

Figure 3.23: Upper critical field anisotropy (γ) versus reduced temperature t (=T/T_c) of $BaFe_{2-x}Co_xAs_2$ for x = 0.082, 0.117 and 0.143 samples. Data points are shown with symbols and lines are guides to the eye. Arrow indicates the shift in peak position with Co content.

From Fig 3.23 it is also apparent that anisotropy (γ) is almost flat at low 't' while at higher't' it is temperature dependent. As the temperature increases, the anisotropy increases and passes through a maximum near T_c and then again it decreases. Similar behavior has been observed for all the three Co compositions. The peak shifts to higher t with increase of Co content. Such a peak like anomaly has also been observed in $BaFe_{2-x}Co_xAs_2$ by other groups [24, 34], and in $Ba_{1-x}K_xFe_2As_2$ [42] and $NdFeAsO_{0.7}F_{0.3}$ [18] systems.

Band structure calculations and ARPES experiments indicated that in $BaFe_{2-x}Co_xAs_2$, the hole Fermi surface strongly disperses along the crystallographic *c*-axis and bands become more isotropic with increase of Co content [41]. Therefore, it is expected that the anisotropy should decrease with increase of Co content, whereas the measured anisotropy of upper critical field increases with temperature. The increase in anisotropy with Co content may arise due to increase in the ratio of inter/intraband scattering. It has been shown by band structure calculations that with increase of Co doping, scattering increases in the hole band compared to electron band and the inter-band scattering is relatively weak [38].

For an isotropic superconductor, γ is independent of temperature. For two band and multi-band superconductors, γ is not constant with temperature and arises because of temperature dependent diffusivities in different bands [22, 43]. In the case of MgB_2, which is a two band superconductor, anisotropy decreases with increase of temperature in clean single crystals [43, 44, 45]. In the dirty limit, γ is an increasing function of T [43, 44]. Calculations indicate that the temperature dependence of γ depends on the relative diffusivities in the two bands which can be changed by substitution and introduction of disorder [43]. The increase in γ with T and peak like anomaly near T_c in $BaFe_{2-x}Co_xAs_2$ single crystals is different from observations in MgB_2. In the case of MgB_2, intra-band scattering dominates over inter-band scattering [43] Contrary to this, for the multi-band arsenide superconductors, inter-band scattering is greater than the intra-band scattering [21, 22]. Theoretical calculations of anisotropy versus temperature in this system including inter-band scattering effects are needed to explain the observed behavior of γ.

3.7 Summary

Electrical transport measurements were carried out in the presence of temperature and magnetic field on single crystals of $BaFe_{2-x}Co_xAs_2$, in the SDW, SC and paramagnetic regimes of the phase diagram.

- In the SDW regime for $B \parallel c$, $BaFe_2As_2$ and doped crystals show MR that can be described by a field dependence of $\beta B+\alpha B^2$; the linear term arising from the quantum transport due to high mobility electrons, with Dirac cone dispersion and the B^2 arising from classical transport.
- With increase in temperature, β decreases implying that the contribution from quantum transport decreases for all the samples studied.
- At a given temperature, Quantum transport is seen to be suppressed significantly by Co substitution, whereas it is not so in the case of Ru substitution.
- α, which depends on the various mobilities and charge densities of the different carriers present in the system, shows a non-monotonic variation with temperature.
- In the $BaFe_{2-x}Co_xAs_2$ sample ($x = 0.082$) an interesting anisotropic MR in the SDW state is seen. The observed transverse MR is negative when magnetic field is parallel to *ab* plane, arises due to detwinning effect.
- Upper critical field (H_{c2}) shows anisotropy for the application of field parallel and perpendicular to the *ab* plane. H_{c2} is larger when B is parallel to *ab* plane and anisotropy (γ) is of the order of ~1.7-2.2. The anisotropy increases with increase of Co composition.

- The value of slope of the upper critical field with temperature $|dH_{c2}/dT|_{T_c}$ normalized to transition temperature (T_c) decreases with increase of Co content due increase in electron Fermi velocity (v_e) with Co substitution.
- Anisotropy (γ) is temperature dependent due to multi-band superconductivity. With increase of temperature γ increases and shows a peak near T_c. The peak shifts to higher temperature with increase of Co content.

References

1. A. A. Abrikosov, *Fundamentals of the Theory of Metals* (North-Holland, Amsterdam, 1988)
2. J. M. Ziman, *Principles of the Theory of Solids*, 2nd edn. (Cambridge University Press, Cambridge, (1972))
3. D. C. Johnston, *Advances in Physics 59, 803* (2010)
4. Z. P. Yin, K. Haule and G. Kotliar, *Nature Physics* **7**,294 (2011)
5. P. Richard, K. Nakayama, T. Sato, M. Neupane, Y.M. Xu, J. H. Bowen, G. F. Chen, J. L. Luo, N. L. Wang, X. Dai, Z. Fang, H. Ding, and T. Takahashi, *Phys. Rev. Lett.* **104**, 137001 (2010)
6. M. D. Johannes and I. I. Mazin, *Phys. Rev.* B **79**, 220510(R) (2009)
7. Hsueh-Hui Kuo, Jiun-Haw Chu, Scott C. Riggs, Leo Yu, Peter L. McMahon, Kristiaan De Greve, Yoshihisa Yamamoto, James G. Analytis, and Ian R. Fisher, *Phys. Rev.* B **84**, 054540 (2011)
8. N. Harrison and S. E. Sebastian, *Phys. Rev.* B **80**, 224512 (2009)
9. V. Brouet,1 M. Marsi, B. Mansart, A. Nicolaou,1, A. Taleb-Ibrahimi, P. Le Fèvre, F. Bertran, F. Rullier-Albenque, A. Forget, and D. Colson, *Phys. Rev.* B **80**, 165115 (2009)
10. Khuong K. Huynh, Yoichi Tanabe, and Katsumi Tanigaki, *Phys. Rev. Lett.* **106**, 217004 (2011)
11. A. A. Abrikosov, *J. Phys. A: Math. Gen.* **36,** 9119 (2003)
12. Y. Tanabe, K. K. Hyunh, S. Heguri, G. Mu, T. Urata, J. Xu, R. Nouchi, N. Mitoma, and K. Tanigaki, *Phys. Rev.* B **84**, 100508(R) (2011)

13. I. Pallecchi, F. Bernardini, M. Tropeano, A. Palenzona, A. Martinelli, C. Ferdeghini, M. Vignolo, S. Massidda, and M. Putti , *Phys.Rev.B* **84,** 134524 (2011)
14. D. Bhoi, P. Mandal, P. Choudhury, S. Pandya, and V. Ganesan , *Appl. Phys. Lett.* **98**, 172105 (2011)
15. N. R. Werthamer, E Helfand, and P C Hohenberg, *Phys. Rev* **147**, 295 (1966)
16. A. M. Clogston, *Phys. Rev. Lett*. **9**, 266 (1962);
17. G. Fuchs, S-L Drechsler, N Kozlova, M Bartkowiak, J E Hamann-Borrero, G Behr, K Nenkov, H-H Klauss, H Maeter, A Amato, H Luetkens, A Kwadrin, R Khasanov,J Freudenberger, A Köhler, M Knupfer, E Arushanov, H Rosner, B Büchner and L Schultz, *New Journal of Physics* **11** 075007 (2009)
18. J. Jaroszynski, F. Hunte, L. Balicas, Youn-jung Jo, I. Raičević, A. Gurevich, and D. C. Larbalestier, *Phys. Rev.* B 7**8**, 174523 (2008)
19. C. Senatore, R. Flükiger, M. Cantoni, G. Wu, R. H. Liu, and X. H. Chen, *Phys. Rev.* B **78**, 054514 (2008)
20. G. F. Chen, Z. Li, G. Li, J. Zhou, D. Wu, J. Dong, W. Z. Hu, P. Zheng, Z. J. Chen, H. Q. Yuan, J. Singleton, J. L. Luo, and N. L. Wang, *Phys. Rev. Lett.* **101,** 057007 (2008)
21. A. Gurevich, *Phys. Rev. B* **82**, 184504 (2010)
22. A Gurevich, *Rep. Prog. Phys*. **74,** 124501 (2011)
23. Marianne Rotter, Marcus Tegel, Dirk Johrendt, Inga Schellenberg, Wilfried Hermes, and Rainer Pöttgen, *Phys. Rev. B* **78**, 020503(R) (2008)
24. N. Ni, M. E. Tillman, J.Q. Yan, A. Kracher, S. T. Hannahs, S. L. Bud'ko, and P. C. Canfield , *Phys. Rev. B* **78**, 214515 (2008)

25. Jiun-Haw Chu, James G. Analytis, Chris Kucharczyk, and Ian R. Fisher, *Phys. Rev. B* **79**, 014506 (2009)
26. Chang Liu, Takeshi Kondo, Rafael M. Fernandes, Ari D. Palczewski, Eun Deok Mun1, Ni Ni, Alexander N. Thaler, Aaron Bostwick, Eli Rotenberg, Jörg Schmalian, Sergey L. Bud'ko, Paul C. Canfield and Adam Kaminski, *Nature Physics* **6**, 419 (2010)
27. M. A. Tanatar, N. Ni, C. Martin, R. T. Gordon, H. Kim, V. G. Kogan, G. D. Samolyuk, S. L.Bud'ko, P. C. Canfield and R. Prozorov, *Phys. Rev.* B **79**, 094507 (2009)
28. Yasuyuki Nakajima, Toshihiro TAEN, and Tsuyoshi Tamegai, *J. Phys. Soc. Jpn.* **78**, 23702 (2009)
29. S. Ran, S. L. Bud'ko, W. E. Straszheim, J. Soh, M. G. Kim, A. Kreyssig, A. I. Goldman, and P. C. Canfield, *Phys. Rev.* B **85**, 224528 (2012)
30. N. Ghosh, A. Bharathi, A.T. Satya, S. Sharma, Awadhesh Mani, R.M. Sarguna, D. Sornadurai, V.S. Sastry, C.S. Sundar, Solid State Communications **150,** 1940 (2010)
31. Jiun-Haw Chu, James G. Analytis, David Press, Kristiaan De Greve, Thaddeus D. Ladd,Yoshihisa Yamamoto, and Ian R. Fisher, *Phys. Rev.* B **81**, 214502 (2010)
32. Jiun-Haw Chu, James G. Analytis, Kristiaan De Greve, Peter L. McMahon, Zahirul Islam, Yoshihisa Yamamoto and Ian R. Fisher*, Science* **329**, 824 (2010)
33. F. Hunte, J. Jaroszynski, A. Gurevich, D. C. Larbalestier, R. Jin, A. S. Sefat, M. A. McGuire, B. C. Sales,D. K. Christen2 & D. Mandrus, *Nature Letters* **453**, 903 (2008)

34. Mika Kano, Yoshimitsu Kohama, David Graf, Fedor Balakirev, Athena S. Sefat, Michael A. McGuire, Brian C. Sales, David Mandrus, and Stanley W. Tozer, *J. Phys. Soc. Jpn.,* **78**, 84719 (2009)
35. A. Yamamoto, J. Jaroszynski, C. Tarantini, L. Balicas, J. Jiang, A. Gurevich, D. C. Larbalestier, R. Jin, A. S. Sefat, M. A. McGuire, B. C. Sales, D. K. Christen, and D. Mandrus, *Appl. Phys. Lett.* **94**, 062511 (2009)
36. A Gurevich, *Physica C*, **456**, 160 (2007)
37. Hyun-Sook Lee, Marek Bartkowiak, Jae-Hyun Park, Jae-Yeap Lee, Ju-Young Kim, Nak-Heon Sung, B. K. Cho, Chang-Uk Jung, Jun Sung Kim, and Hu-Jong Lee, *Phys. Rev. B* **80**, 144512 (2009)
38. Athena. S. Sefat, D. J. Singh, R. Jin, M. A. McGuire, B. C. Sales, and D. Mandrus, *Phys. Rev .B* **79**, 024512 (2009)
39. Athena S. Sefat, Rongying Jin, Michael A. McGuire, Brian C. Sales, David J. Singh, and David Mandrus, *Phys. Rev. Lett.* **101**, 117004 (2008)
40. P. Vilmercati, A. Fedorov, I. Vobornik, U. Manju, G. Panaccione, A. Goldoni, A. S. Sefat, M. A. McGuire, B. C. Sales, R. Jin, D. Mandrus, D. J. Singh, and N. Mannella1, *Phys. Rev.* B **79**, 220503(R) (2009)
41. S. Thirupathaiah, S. de Jong, R. Ovsyannikov, H. A. Dürr, A. Varykhalov, R. Follath, Y. Huang, R. Huisman, M. S. Golden, Yu-Zhong Zhang, H. O. Jeschke, R. Valentí, A. Erb, A. Gloskovskii, and J. Fink, *Phys. Rev.* B **81**, 104512 (2010)
42. Zhao-Sheng Wang, Hui-Qian Luo, Cong Ren, and Hai-Hu Wen, *Phys. Rev.* B **78**, 140501(R) (2008)
43. A. Gurevich, *Phys. Rev.* B **67**, 184515 (2003)

44. A. A. Golubov and A. E. Koshelev, *Phys. Rev.* B **68**, 104503 (2003)

45. V.G. Kogan and S.L. Budko , Physica C **385**, 131 (2003)

Chapter 4

Pressure and Chemical Substitution (P and Yb) dependent Resistivity behavior of $BaMn_2As_2$

Resistivity and X-ray diffraction studies are carried out on $BaMn_2As_2$ as a function of pressure (P). ρ(T,P) shows semiconducting behavior up to 4.5 GPa. Energy gap (Δ) estimated using Arrhenius equation is found to decrease from 38 meV to 3 meV as pressure increases from 0 to 4.5 GPa. At 4.5 GPa, an insulator to metal transition is also observed at ~35 K. Complete metallization in the range 4.2 to 300K occurs at ~5.8 GPa. XRD studies as a function of pressure at room temperature shows an anomaly in the pressure versus volume at ~ 5.5 GPa with out change in the crystal structure, indicative of an electronic transition. A clear precipitous drop is also seen in ρ(T) for $P \geq 5.8$ GPa. At ambient pressure, ρ(T) studies under magnetic field are carried out on polycrystals with P substitution at As site and Yb at Ba site. The semiconducting energy gap decreases with increase of P and Yb substitutions suggestive of possible metallization. Magnetoreistance (MR) is negative both for the pristine and the substituted samples, which decreases with increase of temperature.

In AFe_2As_2 (A= Ca, Sr, Ba) system, application of pressure significantly alters the structural, magnetic and electrical properties [1-7]. The Fe-Fe and Fe-As interatomic distances decrease with increase of pressure both in SDW as well as in paramagnetic state [4]. Application of chemical pressure with Co or Ni substitution at the Fe site and K at the Ba site also shows similar changes in the phyical propeties of these systems [8, 9, 10]. However, in addition to the lattice compression produced because of their smaller radii, these substitutions add charge carriers to the system, electrons for Co/Ni substitution and holes in the case of K substitution [11]. Contrary to the electron doping with Co/Ni at the Fe site, hole doping with Mn/Cr at the Fe site does not induce superconductivity [12, 13]. The Fe-As interatomic distances in the unit cell increases with increase of Mn [14] and the system tranforms to an insulating ground state [14, 15]. These observations highlight the importance of Fe-Fe and Fe-As interatomic distances for the occurance of superconductivity rather than the addition of charge carriers into the system [14,15,16].

Among the class of $ThCr_2Si_2$ - type arsenide compounds, $BaMn_2As_2$ is an interesting compound because it exhibits local moment antiferromagnetic insulating ground state similar to parent compounds of high T_c superconductors [17-20] . The unit cell volume is (234.12 Å^3) is very high compared to unit cell volume (204.38 Å^3) of $BaFe_2As_2$ [11]. As a reduction in Fe-Fe and Fe-As distances reduce the magnetic order leading to superconducivity in AFe_2As_2, the reduction of Mn-Mn and Mn-As distances by applying pressure/chemical substitution could decrease the magnetic moment of Mn and give rise to an insulator to metal transtion and superconductivity in this compound. It is suggested that this compound may have a higher T_c compared to AFe_2As_2 by substitution/pressure because its properties are intermediate to parent compounds of arsenide superconductors, which are itinerant antiferromagnetic metals, and high T_c superconductors, which are antiferromagnetic Mott insulators [11, 18]. Several substitutions were tried at Mn and As site to induce metallicity in this compound but the attempts were not successful for the lack of solubility. Metallisation was observed for 5% K substitution at the Ba site [21]. Here we examine the possibility of metallization of $BaMn_2As_2$ by applying external pressure up to 8 GPa. Substitutions of P at the As site and Yb site Ba site have been carried out to investigate chemical pressure effects.

Single cyrstals of $BaMn_2As_2$ were synthesized using stochiometirc proportions of Ba and MnAs without using flux and slow cooling this stoichiometric mixture from high temperature as described in Chapter 2. Synthesis of polycrystalline $BaMn_2As_{2-x}P_x$ and $Ba_{1-x}Yb_xMn_2As_2$

have already been described in detail in Chapter 2. Room temperature XRD measurements were carried out using Cu Kα radiation using Bragg-Brentano geometry. Lattice parameters have been evaluated using STOE software and PCW software[22]. High pressure resistivity measurements were carried out in home-built, opposed anvil pressure locked cell [23] using steatite as a pressure transmitting medium and pyrophyllite washers as the gasket. Magnetoresistance measurements were carried out from 0 to 12 T. High pressure XRD measurements for pristine $BaMn_2As_2$ at room temperature were done with Mo Kα radiation using a Mao-Bell type diamond anvil cell in an angle-dispersive mode up to 10 GPa [24].

4.1 Structural Characterization of $BaMn_2As_2$ Single Crystals

At room temperature X-ray diffraction (XRD) measurements of the powdered single crystals of $BaMn_2As_2$ were carried out using STOE diffractometer with Cu Kα radiation. The

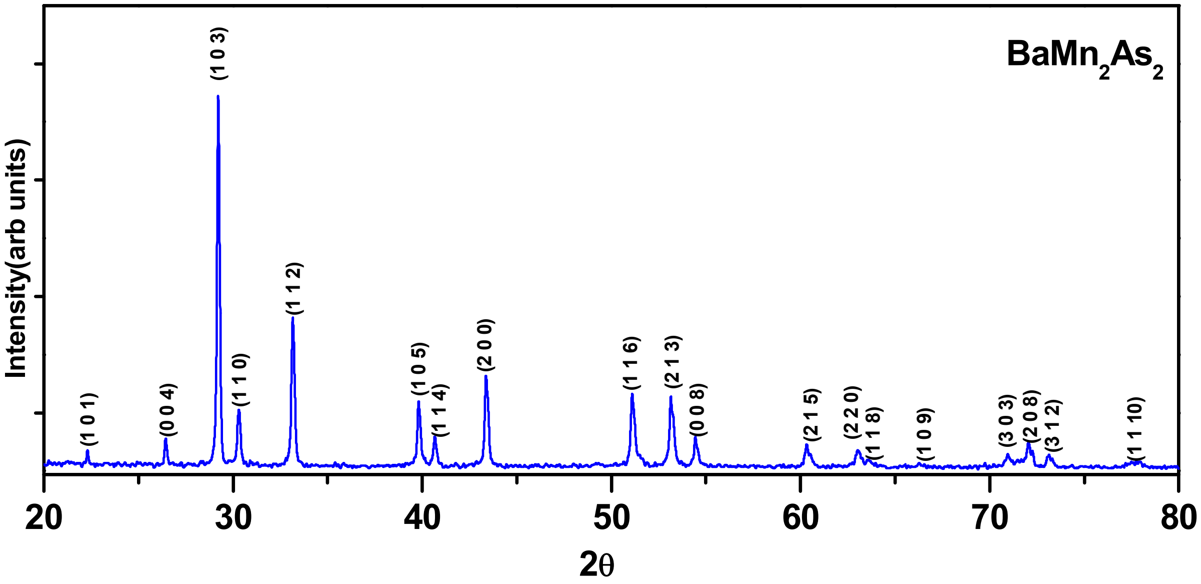

Figure 4.1: X-ray diffraction pattern at ambient temperature taken on powdered single crystals of $BaMn_2As_2$, indexed to I4/mmm space group.

pattern is shown in Fig 4.1. It is evident from the figure that apart from $BaMn_2As_2$ there are no other phases. The XRD pattern could be indexed to tetragonal structure with space group symmetry *I4/mmm* (space group number 139). The lattice parameters were refined using STOE software and they are a = 4.1644(5) Å, c = 13.458(3) Å and V = 233.39(5) Å^3. These results are in good agreement with previous reports [18-20].

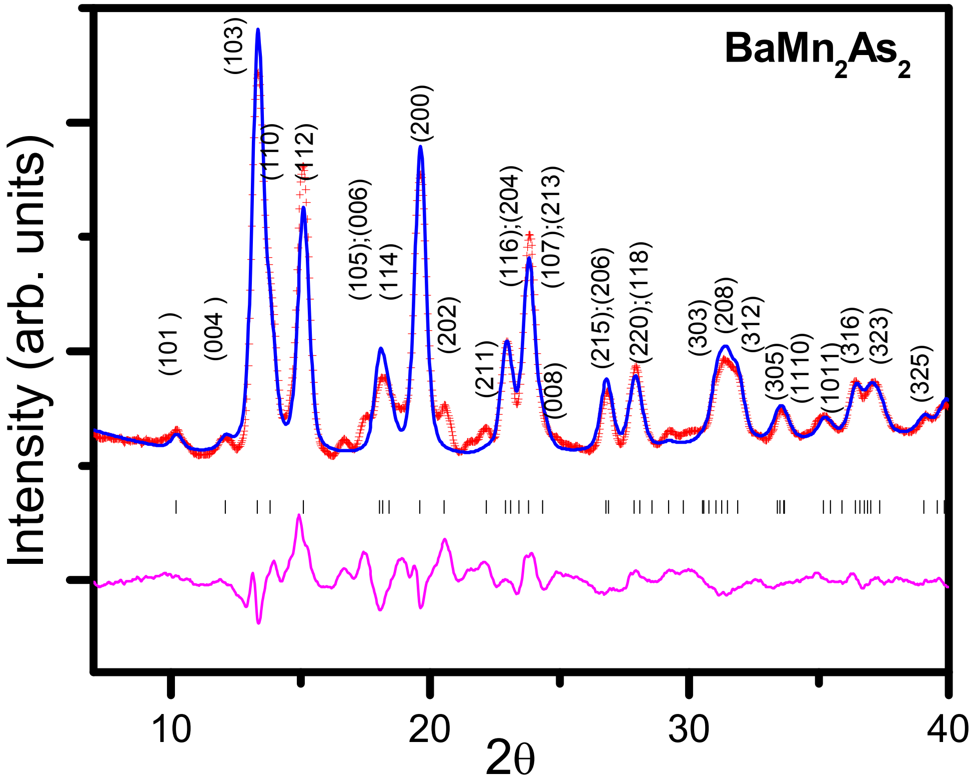

Figure 4.2: X-ray powder diffraction pattern at ambient pressure obtained by powdering $BaMn_2As_2$ single crystals embedded in the melt, using Mo X-ray beam and a Rigaku ULTRAX (18kW) rotating anode X-ray generator, monochromatised with graphite. The plot shows the observed (red +) and the calculated (blue solid line) intensity versus 2θ values, and the difference (pink solid line) obtained from Rietveld refinement.

XRD measurements at ambient temperature were also carried out using Mo Kα radiation. Fig 4.2 shows the powder XRD pattern of the $BaMn_2As_2$ at ambient pressure and temperature measured with Mo Kα in the parallel beam transmission geometry. It is evident from the figure that $BaMn_2As_2$ is phase pure excepting for a small intensity of impurity lines arising from inadvertent contamination during grinding. The lattice parameters were obtained by Rietveld refinement employing GSAS program and they are a = 4.1652(6) Å, c = 13.464(5) Å and V = 233.6(5) Å^3. These values are comparable with the values obtained by XRD measurements using Cu Kα radiation. The Rietveld fits are very good as seen in Fig 4.2.

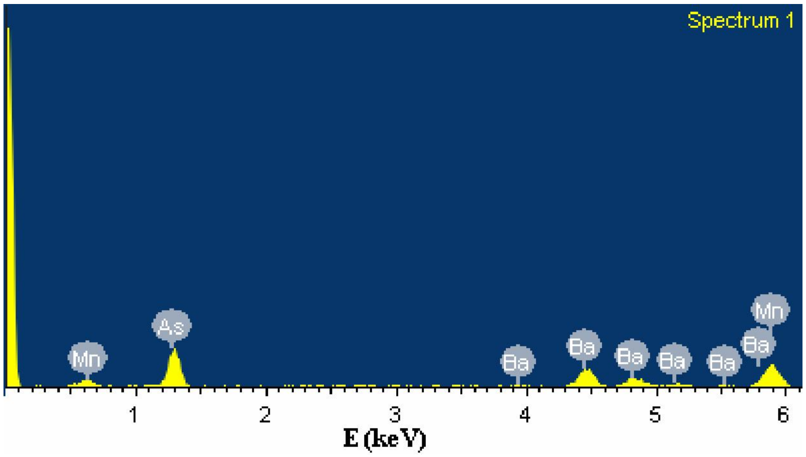

Figure 4.3: EDX spectrum taken on $BaMn_2As_2$ single crystal

Energy dispersive X-ray spectroscopy (EDX) measurements were carried out using Zeiss Supra 55 scanning electron microscope to verify the composition of $BaMn_2As_2$ single crystals. Fig 4.3 shows representative EDX spectrum taken on $BaMn_2As_2$ single crystals. The spectrum shows peaks corresponding to elements of Ba, Mn and As. No other impurity elements were observed. The composition of the single crystals estimated from the analysis of the EDX measurements is consistent with the $BaMn_2As_2$ stochiometry.

4.2 Resistivity ρ(P,T) behaviour

High-pressure resistance measurements R(T) carried out as a function of temperature in the 4.2-300 K range on $BaMn_2As_2$ single crystal sample are shown in Fig 4.4 for a few representative pressures (P) between 0 and 8.2 GPa. At ambient pressure [see Fig 4.4(a)], the

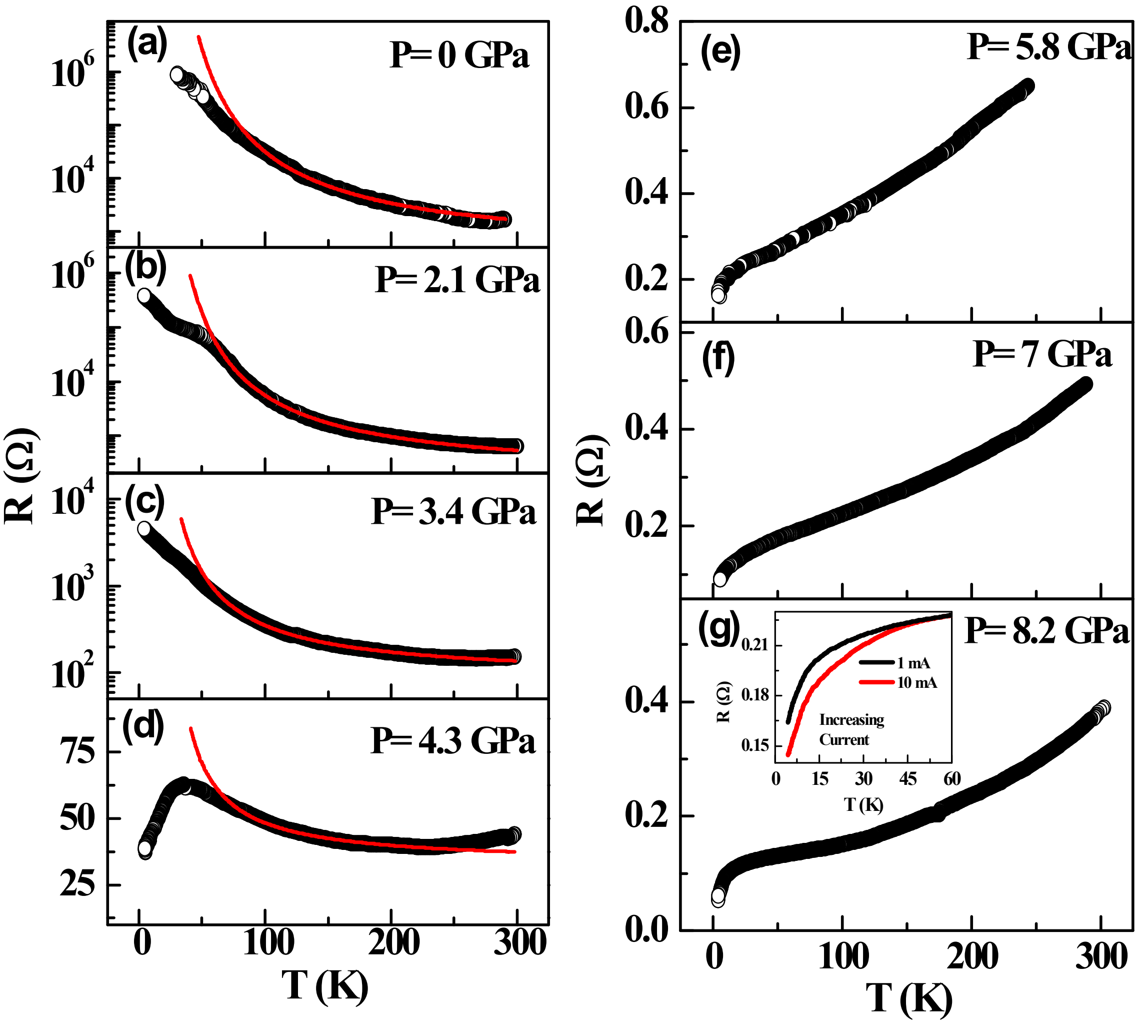

Figure 4.4: Resistance versus temperature for $BaMn_2As_2$ at different pressures between 0 to 8.2 GPa for representative pressures. Left panels indicate the pressure regime in which the samples show a semiconducting behavior. Red solid lines in the Figs 4.3 (a) – 4.3 (d) are fits to $\rho = \rho_0 \exp(\Delta/K_BT)$ in the 70-300 K temperature range. The right panels indicate R(T) in the pressure regime in which the sample shows metallicity. Inset in the Fig 4.3 (g) shows the current dependence of the fall in resistance at 17 K.

resistance increases with decrease of temperature characteristic of a semiconductor. Resistance could not be measured below 30 K at ambient pressure as the value exceeded the measurement limit of the instrument. It must be emphasized that no metallic regime was observed in the R(T) data at ambient pressure, in contrast with the observation of metallic behavior seen above 100 K for single crystals of $BaMn_2As_2$ synthesized by MnAs flux, and above 250 K for Sn flux-grown $BaMn_2As_2$ [18,20]. These metallic behaviors have been attributed to the inclusion of MnAs or Sn in to the lattice [18, 20]. As the pressure increases to P=0.8 GPa (not shown), the R(T) shows insulating behavior in the 70-300 K temperature range, although a significant drop in resistance with respect to ambient pressure data was seen at low temperature. With a further increase in applied pressures to 2.1 and 3.4 GPa [see Figs 4.4 (b) and 4.4 (c)], the resistance at low temperature decreases with a discernible two-step variation of R(T). Interestingly, at 4.3 GPa pressure a remarkable change in R(T) behaviour is seen below 36 K, depicting positive temperature coefficient of resistance, indicating a pressure induced insulator to metal transition at low temperatures. However, a complete metallization in entire measured temperature range is observed for P ≥ 5.8 GPa pressure (cf. Fig 4.4(e)). It should be mentioned that in pressure range of 5.8 to 8.2 GPa, the R(T) exhibit considerable reduction at all temperatures while maintaining the metallic behaviour (see Fig 4.4(e)-(g)). The variation of the resistance as a function of pressure is plotted for various fixed temperatures of 30, 50 and 290 K in Fig. 4.5 (a). The resistance at 30 K is observed to reduce by seven orders of magnitude, at 50 K by five orders of magnitude, and at 290 K by three orders of magnitude as the pressure increases from 0 to 8.2 GPa.

The R(T) data in the insulating regime is fitted to activated behavior [$\rho = \rho_0 \exp(\Delta/K_B T)$] in the 70-300K temperature range. The fitted curves are shown as solid line in the Figs 4.4 (a) -4.4 (d). Below 70 K, at ambient pressure the R(T) data fit to variable range-hopping (VRH) transport [$\rho(T)=\rho_0\exp(T_0/T)^{1/4}$], probably arising from defects states in the semiconducting gap. But for higher pressures this regime does not fit to VRH transport. The activation energies have been obtained form the Arrhenius fits in the 70-300 K

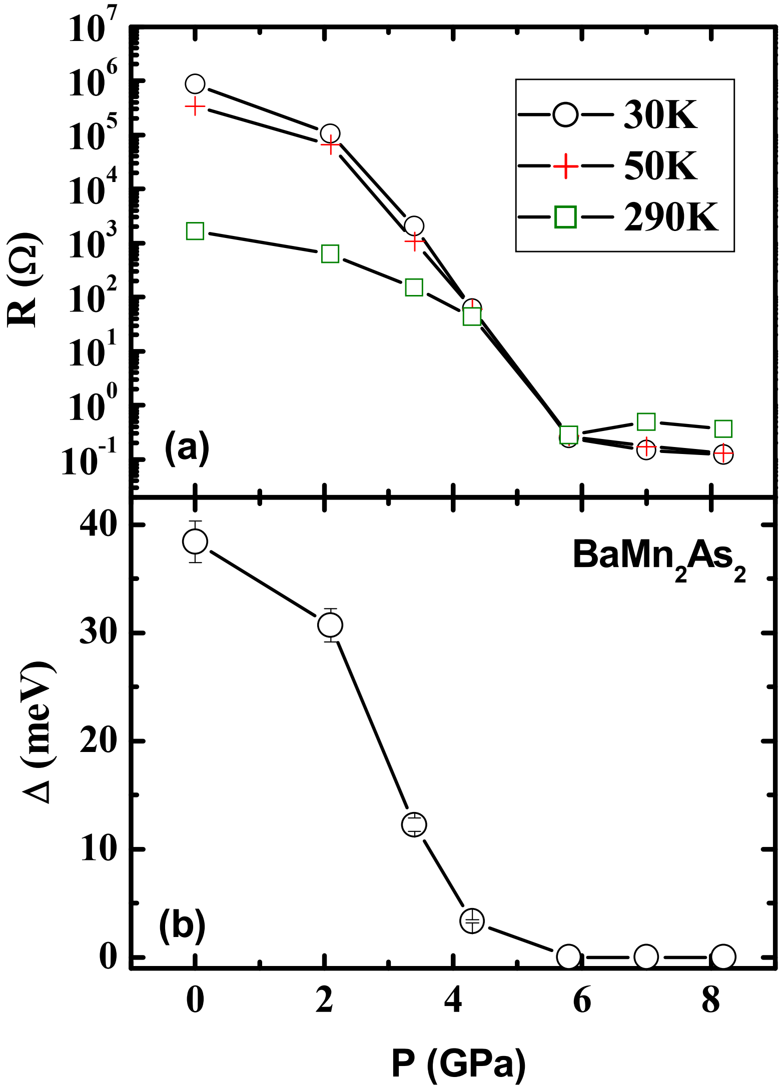

Figure 4.5: (a) Resistance as a function of applied pressure at different temperatures 30, 50 and 290 K to highlight the transition from insulating and metallic behavior at high pressures. (b) The activation energy gap as a function of pressure determined from Arrhenius fits of the R(T) data in the 70-300 K temperature range.

temperature range. Fig 4.5 (b) shows the activation energy (Δ) as a function of applied pressure. It is evident from the figure that the activation energy systematically decreases with increase of pressure. In particular, it decreases from 38.4 ± 2 meV at ambient pressure to 3 ± 0.2 meV at 4.3 GPa, beyond which the crystal shows metallic behavior. The magnitude of the ambient pressure semiconducting gap obtained is comparable to the earlier reports [18, 25].

In addition to the observation of metallicity by application of pressure at 5.8 GPa, a notable fall in resistance was observed at temperature ~ 17 K, which is visible in all the graphs in the right panel of Fig 4.4(e)-(g). The magnitude of the fall in resistance increases with increase of pressure and it is more clearly seen in the R(T) measured at the highest applied pressure of 8.2 GPa. The fall in resistance is shown in the expanded form in the inset of Fig 4.4 (g) at two different currents 1mA and 10 mA. It is clear from the figure that there is a current dependent broadening in the onset of the fall in resistivity. Such a current dependent shift was observed to occur in single crystals of $BaFe_2As_2$ at ~ 3.5 GPa, preceeding the stabilization of a more robust superconducting state at ~ 6.4 GPa, where no current dependence was observed [5]. The present results shown in Fig 4.4 (g), when seen in light of those in Ref [5], could imply that superconductivity occurs in a small fraction of the sample at 8.2 GPa and that superconductivity could be more robust at higher pressures. Unfortunately, the experiments could not be carried out at higher pressures to provide unambiguous evidence for a superconducting transition on account of the limitation of the pressure cell. High-pressure low temperature magnetization measurements are required to be carried out to confirm superconductivity like anomaly seen at 5.8 GPa by measuring the associated diamagnetic signal.

4.3 High Pressure XRD of $BaMn_2As_2$

In the light of the observation of metallization of $BaMn_2As_2$, high pressure XRD measurements at room temperature were carried out to see if the metallization is associated with a structural transition. Fig 4.6 shows the XRD patterns taken on powdered single crystals of $BaMn_2As_2$ using Mo Kα at different pressures from 0.34 GPa to 10 GPa using Mao-Bell type diamond anvil cell (DAC) in an angle dispersive mode. An image-plate based mardtb345 diffractometer was used. The sample to detector distance was calibrated using a standard specimen like LaB_6. The equation of state of silver was used as a pressure calibrant. Two- dimensional data from the Mar 345 IP detector was converted to one dimensional intensity versus 2θ plots using FIT2Dprogram [26]. From the figure it is clear that the diffraction peaks corresponding to both $BaMn_2As_2$ and Ag systematically shift to higher 2θ with increase of pressure. Each data could be indexed with a tetragonal lattice with space group *I4/mmm*. Accurate lattice parameters were obtained by Rietveld refinements employing GSAS program [27]. The detector-to-sample distances for ambient and high pressure were different leading to slight changes in resolution seen in Fig 4.2 and Fig 4.6. The variation of lattice parameters a, c and unitcell volume V with external pressure is shown in Fig 4.7 (a) and (c). While both the lattice parameters a and c decrease monotonically with increasing pressure, there is a distinct change in the pressure variation of lattice parameters, with a crossover region at about ~ 5 GPa.

The volume versus pressure data have been fitted to third order Birch-Murnaghan (BM) equation of state to get the bulk modulus of this material at room temperature. The equation of state of a material gives a relation between volume and applied pressure at a constant temperature [28]. There are several equations of state for volume versus pressure relation in a

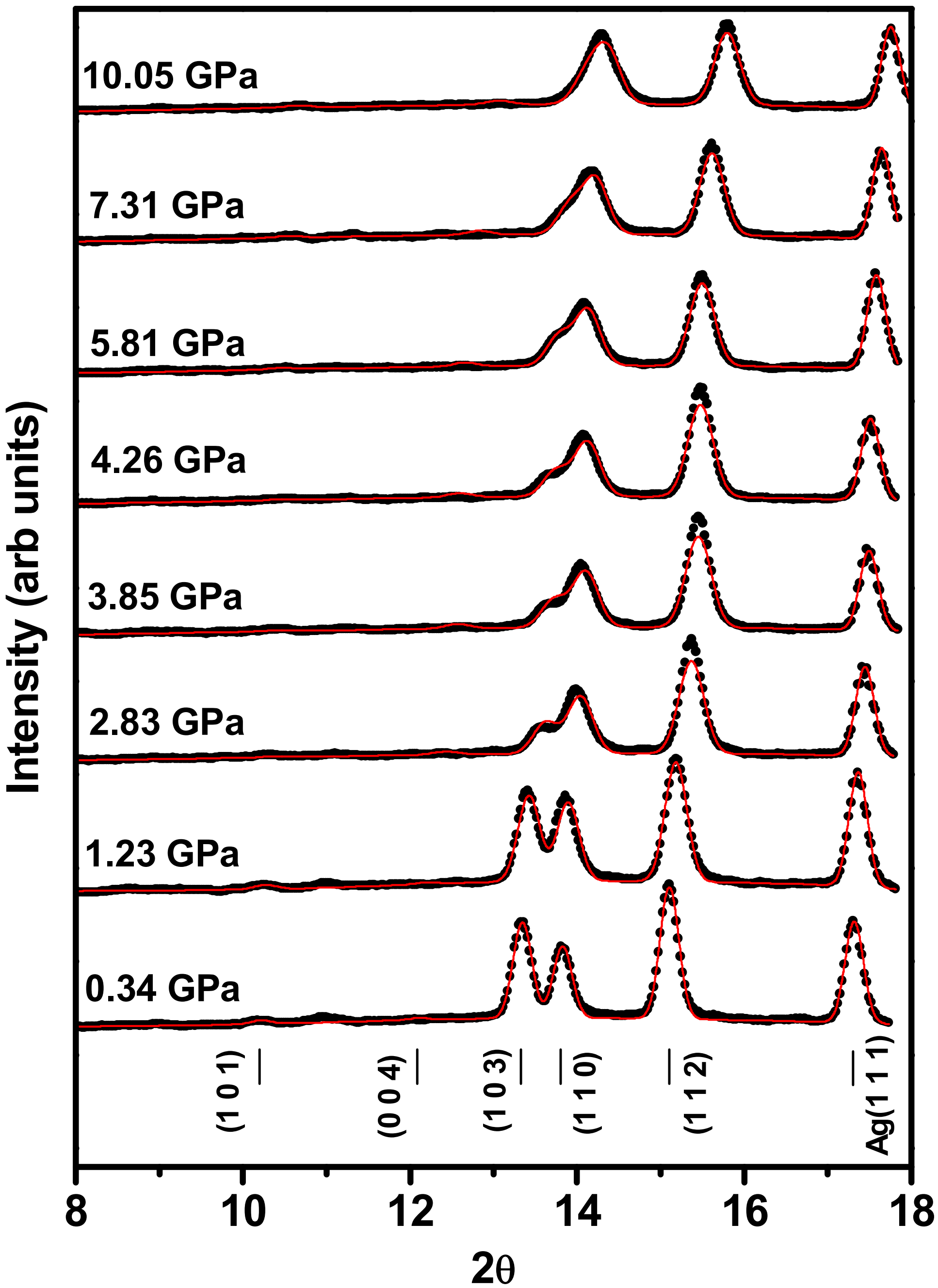

Figure 4.6: XRD patterns at different pressures form 0.34 GPa to 10.05 GPa obtained from powdered single crystals of $BaMn_2As_2$ using Mo x-ray beam and Rigaku ULTRAX (18 kW) rotating anode x-ray generator, monochromatised with graphite. The plots show intensity versus 2θ values, of the observed (black solid circles) and the calculated (red solid line), obtained from Rietveld refinement. Shift of diffraction peak for Ag (1 1 1) at different pressures is also shown.

solid [28]. BM equation of state is one such equation which is widely used in solids. This equation has also been used for the pressure versus volume relation in AFe_2As_2 (Ca, Sr, Ba) systems [1, 4]. According to BM equation [28, 29], pressure versus volume relation in a solid is given by

$$P(V)=\frac{3}{2}K_0.\left[\left(\frac{V}{V_0}\right)^{-\frac{7}{3}}-\left(\frac{V}{V_0}\right)^{-\frac{5}{3}}\right].\left[1-\frac{3}{4}(K_p-4)\left(1-\left(\frac{V}{V_0}\right)^{-\frac{2}{3}}\right)\right] \qquad (1)$$

where V_0 is volume at ambient pressure, K_0 is the bulk modulus and K_P is the first derivative of bulk modulus with pressure, for $P = 0$ or $V=V_0$.

We have fitted cubes of the individual lattice parameters a and c to the BM equation of state and the fits are shown as solid lines in the Fig 4.7 (a). The zero-pressure compressibilities of the individual lattice parameters $\beta_{a0}=\frac{1}{a}\frac{da}{dP}$ and $\beta_{c0}=\frac{1}{c}\frac{dc}{dP}$ are calculated from the values K_{a^3} and K_{c^3} obtained from the fits and they are indicated in the Fig 4.7 (a). The lattice parameter a becomes less compressible at higher pressures, whereas, the compressibility of the lattice parameter c shows slight increase at higher pressures. Fig 4.7 (c) shows the variation of unit cell volume versus applied pressure, and the fits to Birch-Murnaghan equation of state. The difference in the compressibility behavior at low and high pressures with the crossover region at ~ 5 GPa is clearly evident. Interestingly the insulator to metal transition observed in high pressure resistance measurements occurs at ~ 5.8 GPa indicating the metal-insulator transition is related to changes associated with electronic structure. The bulk modulus values obtained from the fits of PV data to BM equation of state are 37 GPa for $P < 5$ GPa and 39 GPa for $P > 6$ GPa. These values are smaller compared to K_0

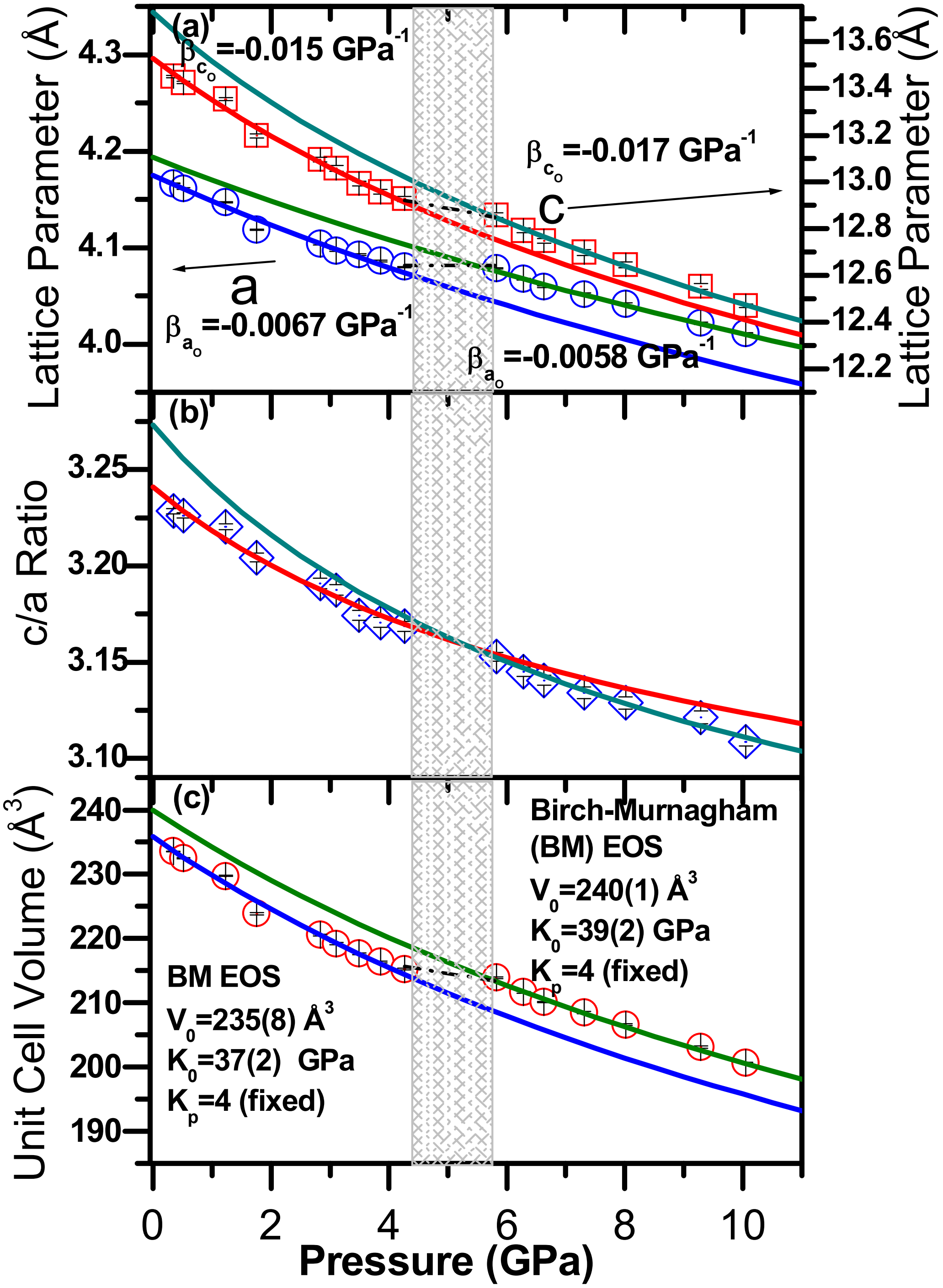

Figure 4.7: (a) The tetragonal lattice cell parameters of $BaMn_2As_2$, *a* and *c* versus applied pressure. (b) The *c/a* ratio versus applied pressure. (c) Unit cell volume (V) versus applied pressure. The solid lines are the fits to the third order Birch-Murunaghan equation of state. The refined values of the zero-pressure volumes as well as the bulk modulus values are shown in the figure. The dotted lines in (a)-(c) are guides to the eye.

obtained in the tetragonal phase of $CaFe_2As_2$ (56 GPa) , $SrFe_2As_2$ (64 GPa) and $BaFe_2As_2$ (66 GPa) systems [1, 4].

The structural parameter of importance in the arsenide system is the *c/a* parameter [1]. Fig 4.7 (b) shows the variation of *c/a* ratio as a function of applied pressure. The magnitude of *c/a* and its smooth variation with pressure indicates that the metallization observed in the present study is not associated with the collapsed tetragonal phase. Another structural transition which is observed in 122 systems is tetragonal (*I4/mmm*) to orthorhombic (*Fmmm*) transition [30, 31]. Fig 4.8 a shows the generated XRD patterns with Mo Kα for $BaMn_2As_2$ with tetragonal *I4/mmm* and orthorhombic *Fmmm* space group symmetries. In case of tetragonal to orthorhombic structural transition with above space group symmetries, the diffraction peaks corresponding to tetragonal (1 1 0) and (1 1 2) planes should split in the

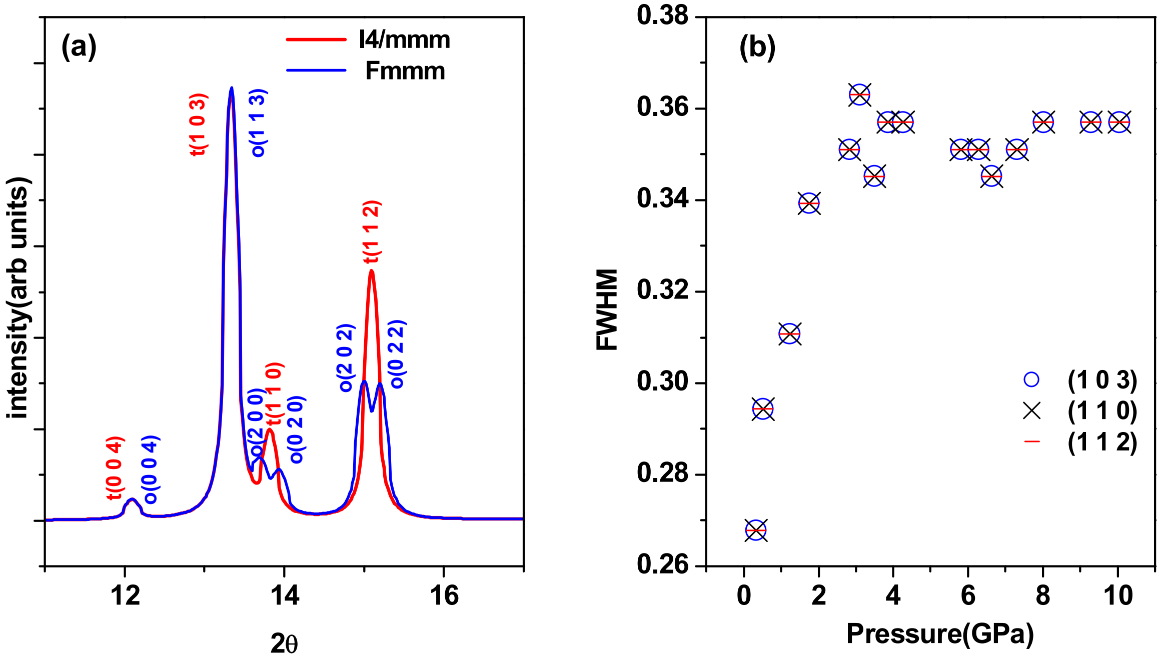

Figure 4.8: (a) Generated XRD patterns of $BaMn_2As_2$ for tetragonal structure with space group *I4/mmm* and orthorhombic structure with space group *Fmmm* by PCW software.
(b) FWHM observed for diffraction peaks corresponding to (1 0 3) , (1 1 0) and (1 1 2) planes at different pressures.

orthorhombic phase. But such a splitting is not observed in the diffraction pattern shown in Fig 4.6. This is also supported by the constant value of the full width half maxima (FWHM) for these reflections in the pressure range 2 to 10 GPa shown in Fig 4.8 b. Increase in the FWHM is expected for (1 1 0) and (1 1 2) planes for a tetragonal to orthorhombic transition. The initial increase in FWHM up to 2 GPa is due to increase in strain because of the application of pressure. The diffraction pattern could be very well fitted with *I4/mmm* space group symmetry at all pressures. So the anomalous change observed at ~ 5 GPa in Fig 4.7 is not associated with tetragonal to orthorhombic structural transition as observed in $BaFe_2As_2$ and $SrFe_2As_2$ systems [30, 31]. Therefore, the insulator-to-metal transition observed in the high pressure resistance measurements is associated with an isostructural transition and points to an electronic topological transition (ETT) induced by pressure. Isostrucural transitions have been observed in many systems where volume anomalies correspond to electronic topological transitions involving large variation of density of states at the Fermi level [32-35]. The occurrence of ETT has also been observed in the arsenide family [36].

The room temperature cell volume in $BaTm_2As_2$, where Tm is a 3d transition element from Cr to Cu, shows an anomalous increase at Tm = Mn, that is linked to its high spin state[11]. It is noteworthy that the cell volumes observed upon metallization of $BaMn_2As_2$ are very close to the cell volumes of $BaCr_2As_2$ and $BaFe_2As_2$, both of which are itinerant antiferromagnets. These observations suggest that cell volume plays an important role in the stabilization of metallic state in this system. The magnetic moments of $BaCr_2As_2$ (~ 2 μ_B) [37] and $BaFe_2As_2$ (~ 0.9 μ_B) [11] are smaller as compared to magnetic moment of $BaMn_2As_2$ (3.9μ_B) [19] indicating that decrease in unit cell volume could reduce the magnetic moment, due to delocalization of localized *d*-bands. The observation of metallicity in high pressure resistivity measurements in $BaMn_2As_2$ therefore might have its origin in the suppression of magnetic moment on account of broadening and overlapping of conduction and valence bands with increase of pressure. Insulator to metal transition and superconductivity has also been observed by suppression of magnetic order in the parent compound of high T_c superconductor $YBa_2Cu_3O_{6+x}$ by changing the oxygen content [38]. Band structure calculations and neutron diffraction measurements at high pressure in $BaMn_2As_2$ would be worthwhile to elucidate the nature of the electronic transition, as also studies on the evolution of the magnetic state of $BaMn_2As_2$ as it metallizes under the application of pressure.

4.4 $BaMn_2As_{2-x}P_x$ polycrystals

4.4.1 Structural characterization

Taking the cue from the study of external pressure effect on the resistivity behavior of $BaMn_2As_2$, P substitution at As site is attempted to investigate whether chemical pressure also induces metallization in this compound. Polycrystalline samples of $BaMn_2As_{2-x}P_x$ were synthesized by solid state method as detailed in Chapter 2. Powder X-ray diffraction measurements were carried out using STOE X-ray diffractometer with Cu Kα radiation and XRD patterns for different samples are shown in Fig 4.9. The diffraction peaks could be indexed to the tetragonal structure with space group symmetry *I4/mmm* for all the samples. Small amounts of impurities viz., MnO and MnAs are observed for x = 0.3 sample. For x = 0.4 sample, some extra diffraction peaks are also observed in addition to these impurities. The lattice parameters were refined using STOE software and the variation of lattice parameters with P content is shown in Fig 4.10. It is evident from the figure that the P substitution with x

= 0.2 leads to a decrease in the lattice parameters *a* & *c* as compared to that of the pristine compound. However with further increase in x > 0.2, no appreciable variation in the lattice parameters is observed (cf. Fig 4.10).

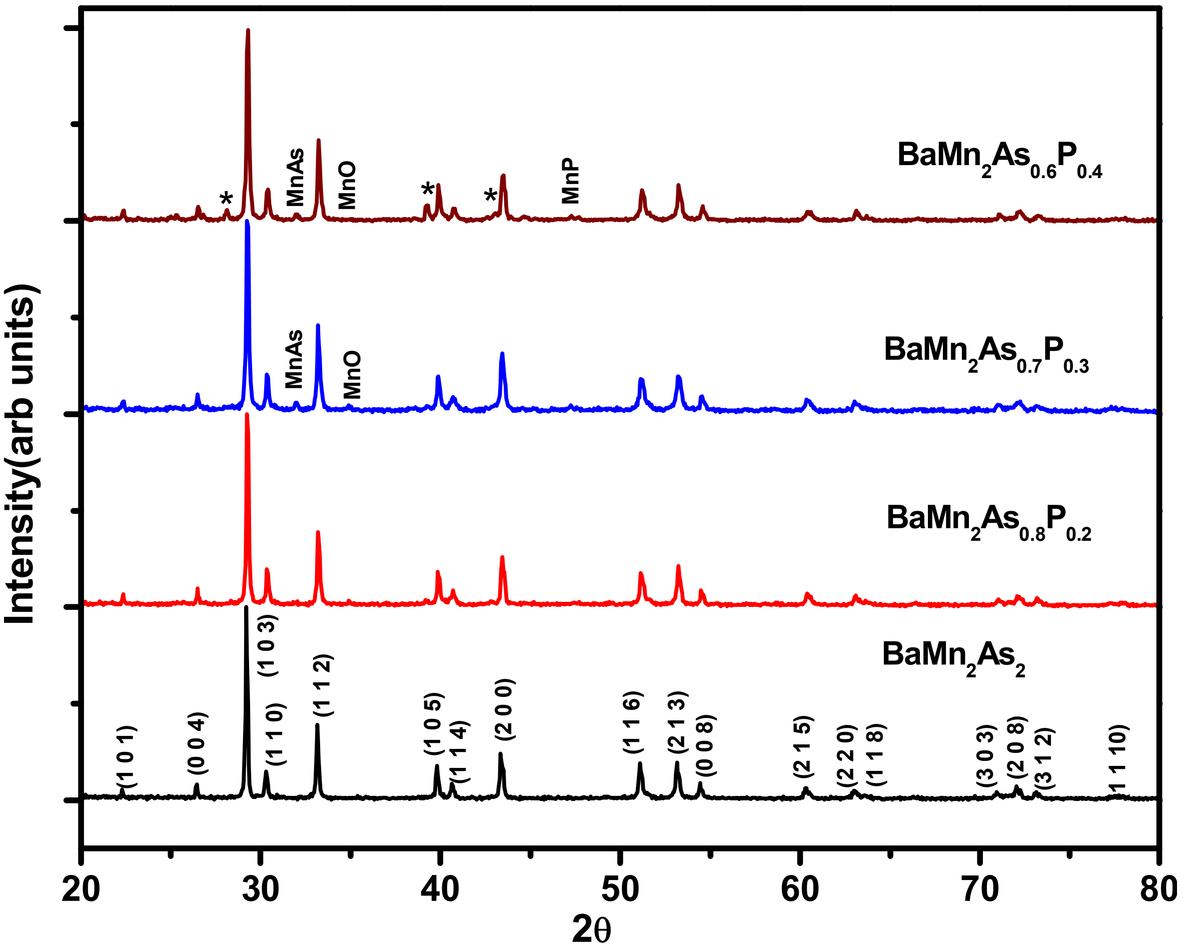

Figure 4.9: XRD patterns for polycrystalline samples of BaMn$_2$As$_{2-x}$P$_x$. Diffraction peaks are indexed to tetragonal space group symmetry *I4/mmm*.

4.4.2 Resistivity behaviour

Temperature dependent resistivity measurements ρ(T) carried out from 4.2 K to 300 K are shown in Fig 4.11 and Table.1. The room temperature resisitivity for the pristine

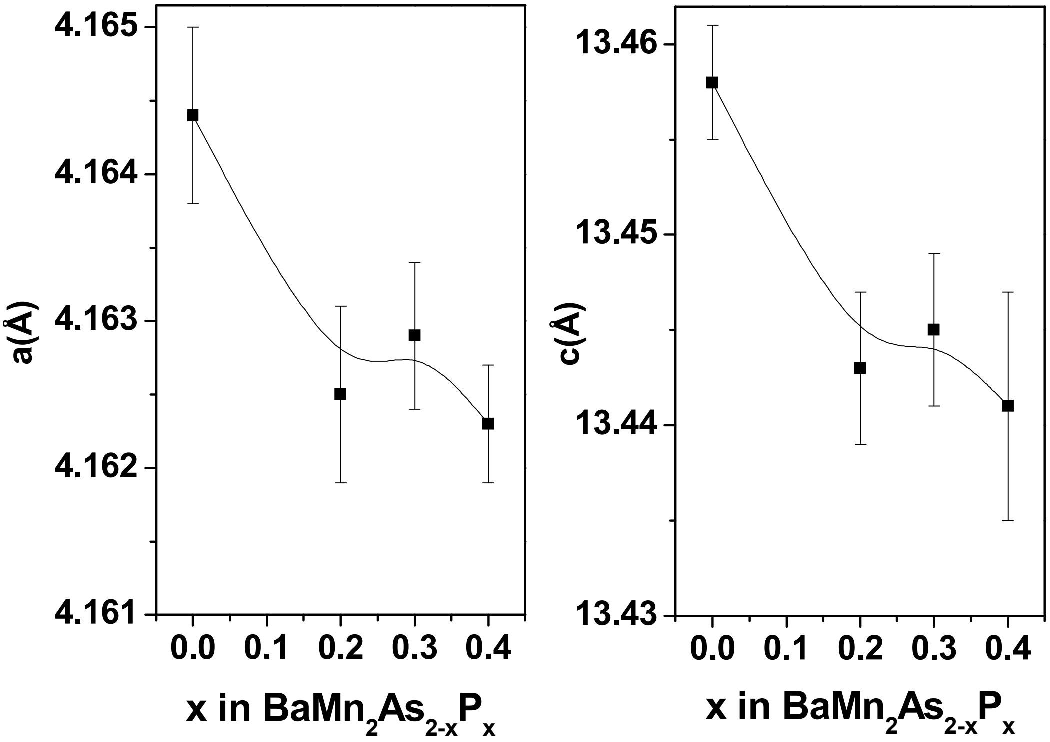

Figure 4.10: Variation of lattice parameters *a* and *c* as a function of P content x in $BaMn_2As_{2-x}P_x$

Samples	*a* (Å)	*c* (Å)	*V* (Å^3)	ρ_{300K} (Ω-cm)	Δ (meV)	$\dfrac{\rho(15K)}{\rho(300K)}$
$BaMn_2As_2$	4.1644 (6)	13.458 (3)	233.39 (4)	30	43	1.5 x 10^4
$BaMn_2As_{1.8}P_{0.2}$	4.1625 (6)	13.443 (4)	232.92 (3)	2	15	134
$BaMn_2As_{1.7}P_{0.3}$	4.1629 (5)	13.445 (4)	233.00 (3)	0.2	2.5	1.2
$BaMn_2As_{1.6}P_{0.4}$	4.1623 (4)	13.442(2)	232.92 (4)	3	110	1.8 x 10^4

Table 1: Lattice parameters *a, c* and unitcell volume *V,* room temperature resistivity ρ_{300K} and energy gap Δ and resistivity ratio ρ(15K)/ρ(300K) for $BaMn_2As_{2-x}P_x$.

$BaMn_2As_2$, was deduced using van der Pauw technique, is found to be ~ 30 Ω-cm. It is evident from Fig 4.11 that the resistivity ρ(T) of all the samples exhibit semiconducting behavior in the measured temperature range. The resistivity ratio (RR) defined as $\frac{\rho(15K)}{\rho(300K)}$ is found to be $1.5\text{x}10^4$ for the pristine sample. The resistivity is fitted to the Arrhenius equation $\rho = \rho_0 \exp(\Delta/k_BT)$ in the temperature range 75 to 300 K to get the activation energy which is found out to be 43 meV (see Fig 4.11(a)). This value is in good agreement with the Δ values from single crystal resistivity measurements [18, 25]. With the substitution of P fraction of x = 0.2, the room temperature resistivity reduces to ~ 2 Ω-cm and at 15 K it reduces by three orders of magnitude as compared to that in the pristine compound (see Fig 4.11(b)) giving RR=134. The activation energy gap decreases to ~ 15 meV (see Table.1), as was the case under the application of pressure. With further increase in P content to x =0.3, the resistivity at 300 K reduces further to 0.2 Ω-cm and at 15K it reduces by 6 orders, giving RR=1.2 as seen from Fig 4.11(c). The ρ(T) fits to the activated behavior in the temperature range 150 to 300 K yielding the energy gap of ~ 2.5 meV. In the range 50 to 130 K, the resistivity shows a plateau like behavior and below 50 K it further increases exponentially. Such a two step like increase in ρ(T) has been observed in many semiconducting systems and arises because of defect states that populate the gap in the system [40-42].

The observed decrease in resistivity in $BaMn_2As_2$ with P substitution for x = 0.2 and 0.3 is intrinsic in nature as the impurities present in the samples MnO and MnAs are very small. MnO is a Mott insulator [43] so it does not contribute to decrease in resistivity observed for these samples. Although impurity MnAs is a ferromagnetic metal, the estimated volume fraction obtained from refinement of the XRD data using PCW software is of the order ~ 6 % which is small and does not corroborate with the observed negative temperature co-efficient of resistivity seen in Fig. 4.11, since the resistivity of MnAs continuously decreases in the temperature range 4 to 300 K [44]. Therefore, the two step increase in resistivity observed for $BaMn_2As_{1.7}P_{0.3}$ can be intrinsic to that compound. The x= 0.4 sample had a large fraction of impurity phases, implying that x=0.3 is possibly the solubility limit in this system.

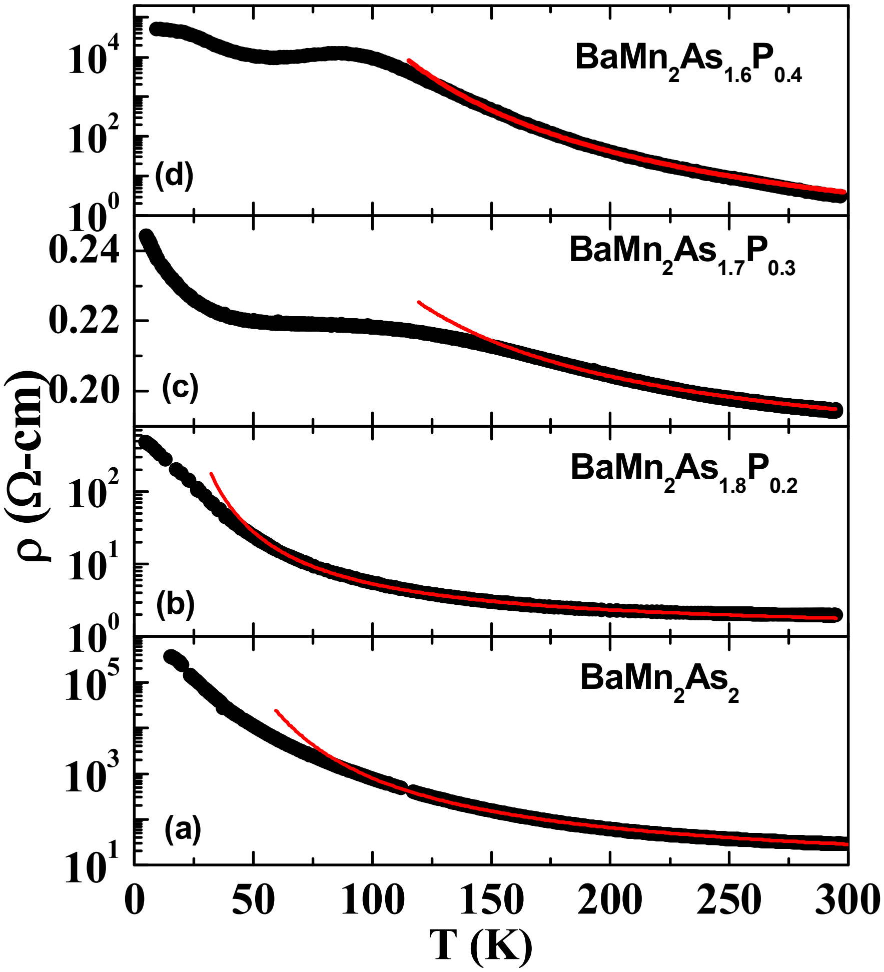

Figure 4.11: Resistivity versus temperature for poly crystalline $BaMn_2As_{2-x}P_x$ samples in the range 4.2 to 300 K. The red solid lines are fits to the Arrhenius equation $\rho = \rho_0 \exp(\Delta/K_BT)$.

4.5 $Ba_{1-x}Yb_xMn_2As_2$ polycrystals

4.5.1 Structural characterization

Having performed P substitution studies at As site, we have further investigated the effect of chemical pressure of the ground state properties of $BaMn_2As_2$ by substituting of Yb at the Ba site. Yb exists in two ionic states Yb^{+2} and Yb^{+3} with their radii 1.94 Å and 1.74 Å respectively, which are smaller than the ionic radius 2.24 Å of Ba^{2+} [39]. Here again the substitution of Yb is equivalent to applying chemical pressure in the system. $Ba_{1-x}Yb_xMn_2As_2$ poly crystals were synthesized using solid state method as described in Chapter 2. Results of

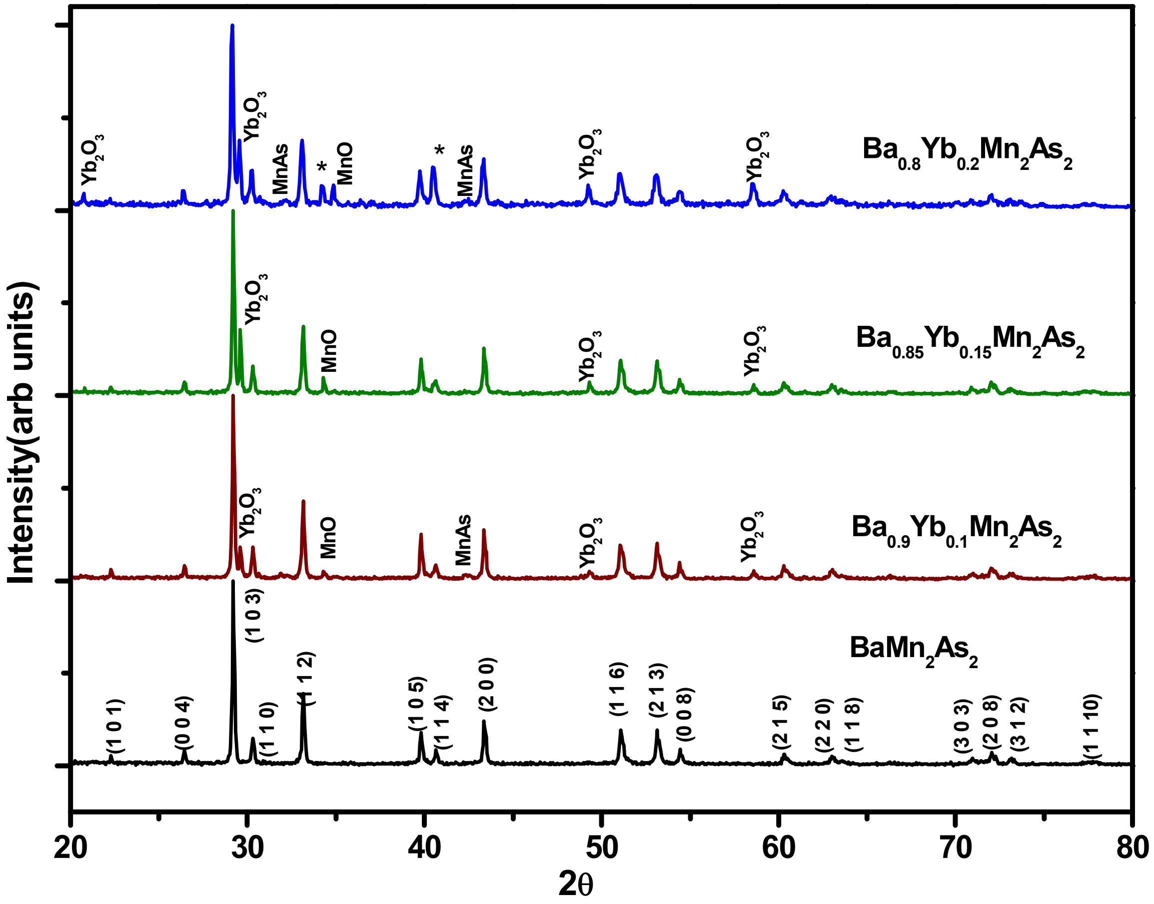

Figure 4.12: XRD patterns for polycrystalline samples of $Ba_{1-x}Yb_xMn_2As_2$. Diffraction peaks are indexed to tetragonal space group symmetry *I4/mmm*.

powder XRD measurements are shown in the Fig 4.12 and Table. 2. For x = 0.1 and 0.15 samples, small amount of impurities Yb_2O_3, MnAs and MnO are observed. For x =0.2 sample, some additional un-indexable diffraction peaks are also observed. The lattice parameters *a* and *c* refined from the XRD data using STOE and PCW software, show an increase with increase of Yb content x up to x = 0.2 (see Fig 4.13& Table 2). The increase in lattice parameters with increase of x is contrary to the decrease expected based on the ionic radii. With further increase in x, the lattice parameters do not change and the volume fractions of impurities Yb_2O_3, MnAs and MnO found to increase indicating that the solubility limit of Yb fraction is x=0.2.

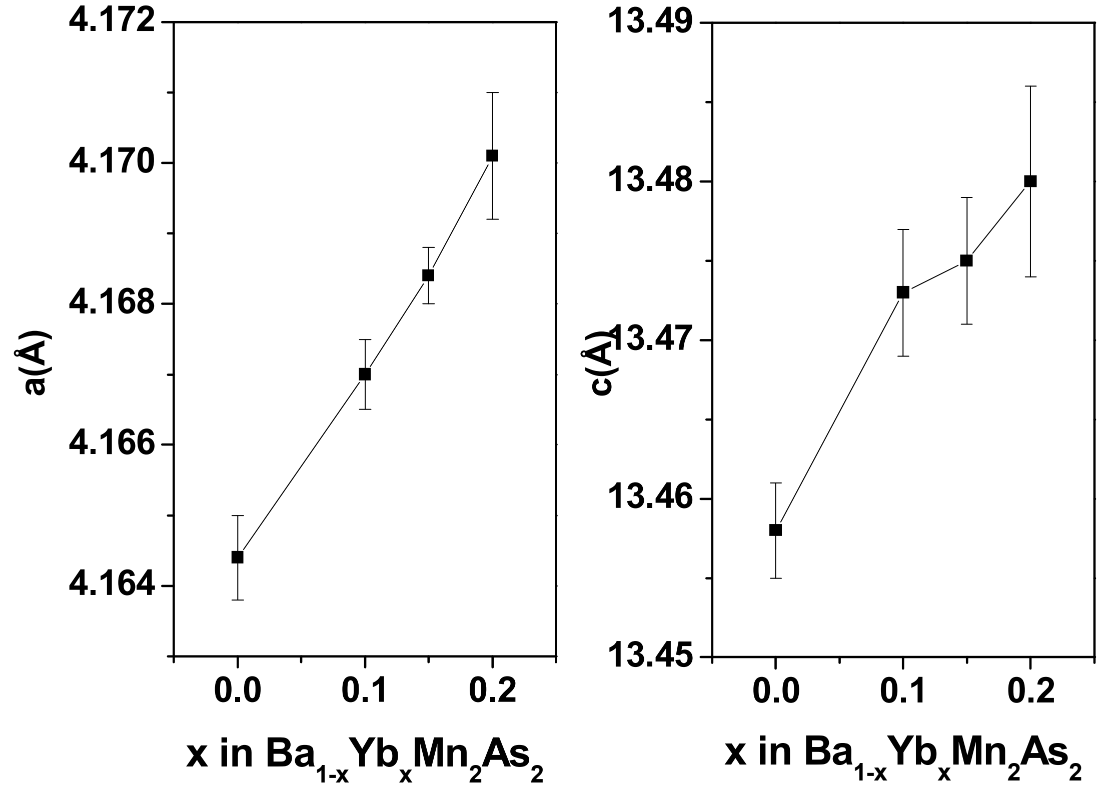

Figure 4.13: Variation of lattice parameters *a* and *c* as a function of Yb content x in $Ba_{1-x}Yb_xMn_2As_2$.

	a (Å)	c (Å)	V (Å^3)	ρ_{300K} (Ω-cm)	Δ (meV)	$\frac{\rho(15K)}{\rho(300K)}$
$BaMn_2As_2$	4.1644 (6)	13.458 (3)	233.39 (4)	30	43	1.5 x 10^4
$Ba_{0.9}Yb_{0.1}Mn_2As_2$	4.1670 (5)	13.473 (2)	233.94 (4)	6	16	10
$Ba_{0.85}Yb_{0.15}Mn_2As_2$	4.1684 (4)	13.475 (2)	234.12 (4)	4	7	1.75
$Ba_{0.8}Yb_{0.2}Mn_2As_2$	4.1701(9)	13.478 (4)	234.40 (7)	0.24	-	0.064

Table 2: Lattice parameters a, c and unitcell volume V, room temperature resistivity ρ_{300K} and energy gap (Δ) and resistivity ratio ρ(15K)/ρ(300K) for $Ba_{1-x}Yb_xMn_2As_2$.

4.5.2 Resistivity behaviour with Yb substitution

Figure 4.14 shows the temperature dependent resistivity behavior of $Ba_{1-x}Yb_xMn_2As_2$ polycrystalline samples in the range 4.2 to 300 K. With increase of Yb content from x = 0 to 0.2, the room temperature resisitivity decreases from 30 Ω-cm to 0.24 Ω-cm. ρ(300 K) values for different samples are presented in Table 2. For x =0.1 sample, ρ(T) shows insulating behavior from 4.2 to 300 K (see Fig 4.14(b)). The activation energy gap is deduced by fitting ρ(T) data to Arrhenius equation in the temperature range 75 to 300K. The energy gap (Δ) (see Table 2) is found to be 16 meV, which is smaller than that of the pristine compound. With further increase in x to 0.15, the energy gap is further reduced to 7 meV. The resistivity at 15 K decreases by four orders of magnitude at 15 K compared to pristine compound (see Fig 4.14(c)). For x =0.2 sample, ρ(T) shows positive temperature coefficient in the temperature range 4.2 to 300 K. The monotonic change in the resistivity behaviour and systematic variation in the lattice parameter values with Yb substitution gives ample evidence for the substitution of Yb in $BaMn_2As_2$ and suggests that metallization could be intrinsic to the substitution of Yb in the lattice.

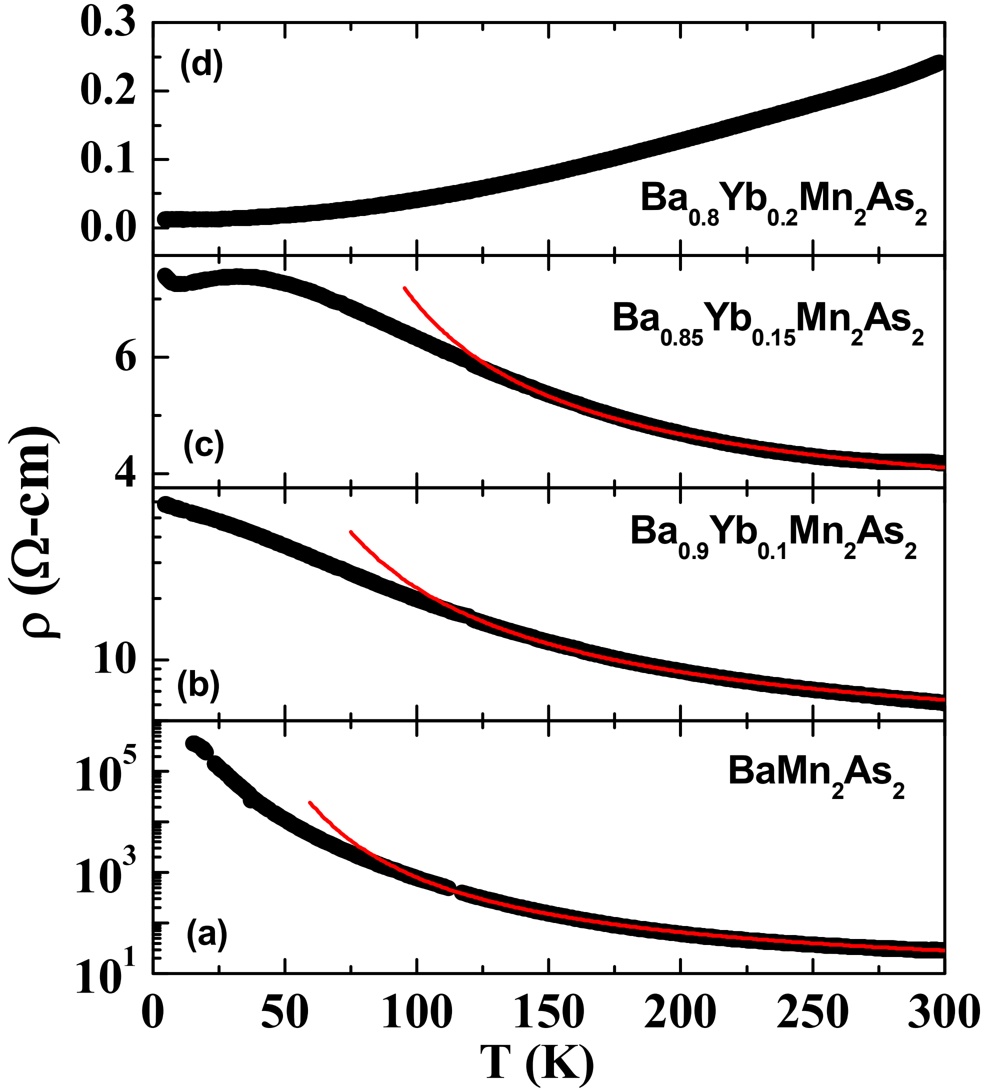

Figure 4.14: Resistivity versus temperature for poly crystalline $Ba_{1-x}Yb_xMn_2As_2$ samples in the range 4.2 to 300 K. The red solid lines are fits to the Arhenius equation $\rho = \rho_0 \exp(\Delta/K_BT)$.

4.6 Magnetoresistance behavior of $BaMn_2As_2$, $BaMn_2As_{1.8}P_{0.2}$ and $Ba_{0.9}Yb_{0.1}Mn_2As_2$

MR measurements were carried out on polycrystalline $BaMn_2As_2$, $BaMn_2As_{1.8}P_{0.2}$ and $Ba_{0.9}Yb_{0.1}Mn_2As_2$ samples from 0 to 10 T in the temperature range 15 to 200 K.

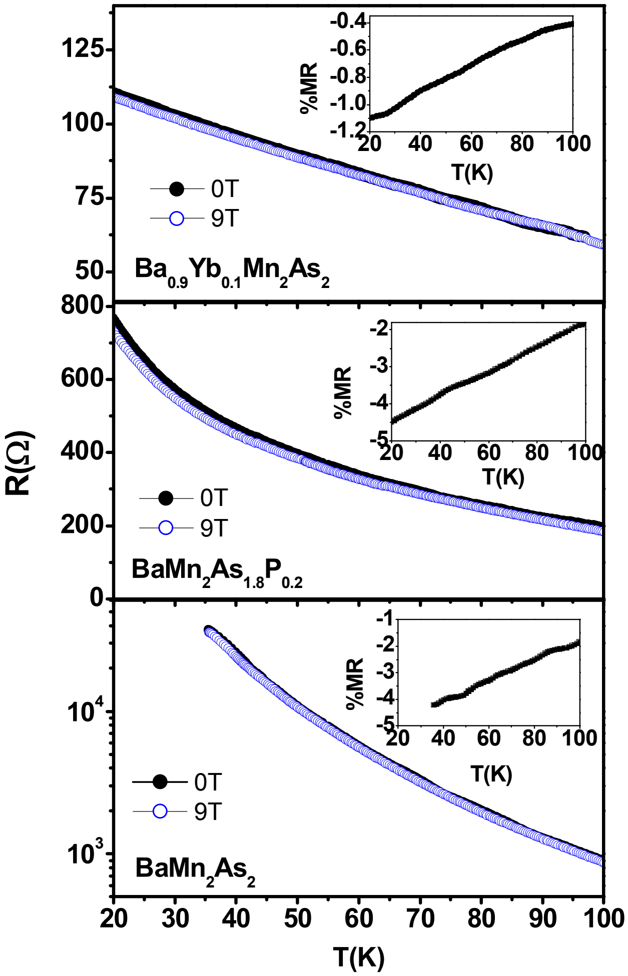

Figure 4.15: Resistivity versus temperature for polycrystalline $BaMn_2As_2$, $BaMn_2As_{1.8}P_{0.2}$and $Ba_{0.9}Yb_{0.1}Mn_2As_2$ samples in the range 20 to 100 K at applied fields 0 and 9T. The insets in each graph shows the MR versus temperature at 9T for the respective samples.

Fig 4.15 shows the temperature dependent resistances for different samples from 20 to 100 K at applied fields 0 and 9 T. For all the three samples the resistance decreases by the application of 9 T field giving negative MR at a given temperature and the magnitude of MR decreases with increase of temperature. The magnitude of MR for pristine and P doped samples at 35 K are of the order ~- 4.5% and for Yb doped sample it is ~-1%. Recently Huan Li et al predicted negative MR with fields parallel to ab plane and positive MR with field parallel to c-axis for G- antiferromagnetic metal $Ba_{1-x}K_xMn_2As_2$ using J_1-J_2-J_c Heisenberg model [43].

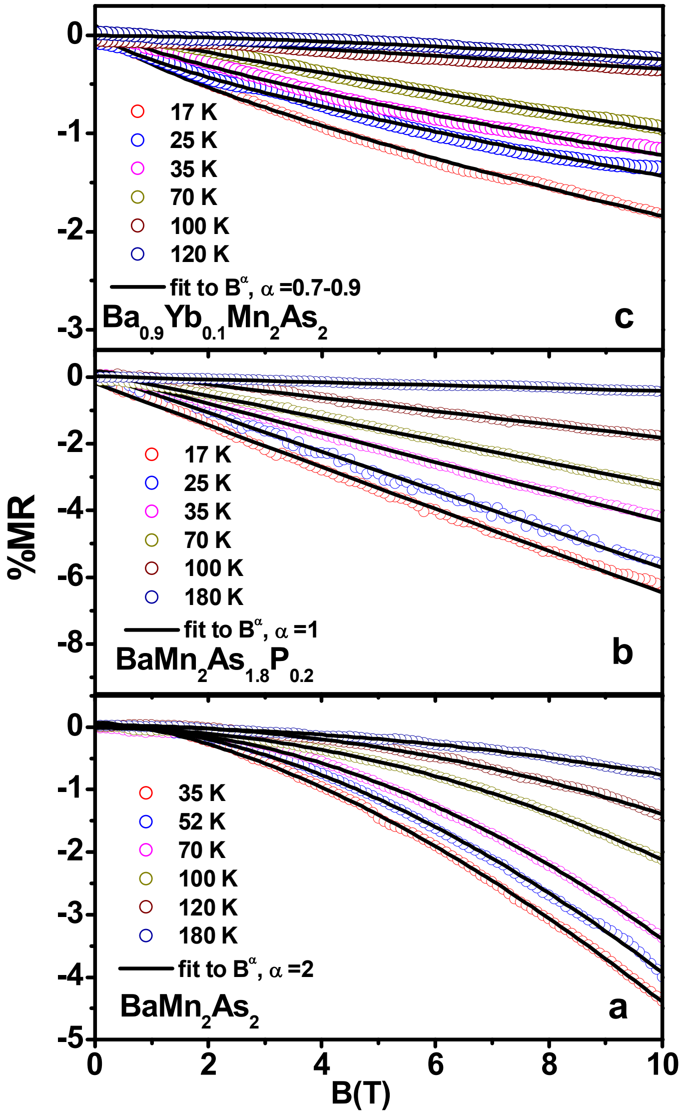

Figure 4.16: MR versus magnetic field for poly crystalline $BaMn_2As_2$, $BaMn_2As_{1.8}P_{0.2}$and $Ba_{0.9}Yb_{0.1}Mn_2As_2$ samples from 0 and 9T at different temperatures. Symbols are the experimental points and solid black line is fit to $aB^{\alpha} + b$.

Fig 4.16 shows isothermal MR measurements from 0 to 10 T at different temperatures for the three samples. MR has been fitted to B^{α} dependence and the fits for different samples are shown as solid lines in the Fig.4.16. The value of the exponent α is found out to be ~2 for the pristine compound at all the temperatures. For $BaMn_2As_{1.8}P_{0.2}$, the exponent α is ~ 1. For $Ba_{0.9}Yb_{0.1}Mn_2As_2$, it varies as ~ $B^{0.7}$ and the exponent changes from 0.7 to 0.9 at higher temperatures for this sample. Further work on single crystals may be required to get ascertain the observed behaviour of MR in the pristine $BaMn_2As_2$ and samples with Yb and P substitutions.

4.7 Summary

Resistivity behavior of $BaMn_2As_2$ has been studied as a function of pressure, magnetic field and temperature. The effect of substitution with P at the As site and Yb at the Ba site on resistivity behavior have also been investigated. The main conclusions of this study are

- $BaMn_2As_2$ is a narrow gap semiconductor with Δ ~ 40 meV, in which the gap decreases with increase of pressure leading to metal insulator transition at 5.5 GPa.
- Metal insulator transition is not associated with structural transition but it is due to isostructural electronic topological transition in the system with different compressibilities above and below the critical pressure of ~ 5.5 GPa.
- The anomalous resistance fall observed at ~ 17 K for $P > 5.5$ GPa in the resistivity could be due to superconducting transition.
- P and Yb doping induce the reduction in the energy gap with increase of doping indicating possibility of metallization. Complete metallization in the temperature

range of investigation from 4.2 to 300 K is not observed for P substitution up to 20 %. Complete metallization is observed for 20% Yb substitution, although there is possibility that it could be extrinsic due to the presence of impurities.

- MR is negative and varies quadratically for pristine compound.

References

1. Deepa Kasinathan, Miriam Schmitt, Klaus Koepernik, Alim Ormeci, Katrin Meier, Ulrich Schwarz, Michael Hanfland, Christoph Geibel, Yuri Grin, Andreas Leithe-Jasper, and Helge Rosner , *Phys. Rev. B* **84**, 054509 (2011)
2. E. Colombier, S. L. Bud'ko, N. Ni, and P. C. Canfield*,* *Phys. Rev. B* **79**, 224518 (2009)
3. Fumihiro Ishikawa, Naoya Eguchi, Michihiro Kodama, Koji Fujimaki, Mari Einaga, Ayako Ohmura, Atsuko Nakayama, Akihiro Mitsuda, and Yuh Yamada, *Phys. Rev. B* **79**, 172506 (2009)
4. R. Mittal, S. K. Mishra, S. L. Chaplot, S. V. Ovsyannikov, E. Greenberg, D. M. Trots, L. Dubrovinsky, Y. Su,Th. Brueckel, S. Matsuishi, H. Hosono,and G. Garbarino, *Phys. Rev. B* **83**, 054503 (2011)
5. S. K. Kim, M. S. Torikachvili, E. Colombier, A. Thaler, S. L. Bud'ko, and P. C. Canfield, *Phys. Rev. B*, **84**, 134525 (2011)
6. Takehiro Yamazaki, Nao Takeshita, Ryosuke Kobayashi, Hideto Fukazawa, Yoh Kohori, Kunihiro Kihou, Chul-Ho Lee, Hijiri Kito, Akira Iyo and Hiroshi Eisaki, *Phys. Rev. B*, **81**, 224511 (2010)
7. A. I. Goldman, A. Kreyssig, K. Prokeš, D. K. Pratt, D. N. Argyriou, J. W. Lynn, S. Nandi, S. A. J. Kimber, Y. Chen, Y. B. Lee, G. Samolyuk, J. B. Leão, S. J. Poulton,4,5 S. L. Bud'ko,1,2 N. Ni,1,2 P. C. Canfield, B. N. Harmon, and R. J. McQueeney, *Phys. Rev. B* **79**, 024513 (2009)
8. Jiun-Haw Chu, James G. Analytis, Chris Kucharczyk, and Ian R. Fisher, *Phys. Rev. B*, **79**, 014506 (2009)

9. N. Ni, A. Thaler, J. Q. Yan, A. Kracher, E. Colombier, S. L. Bud'ko, and P. C. Canfield, S. T. Hannahs, *Phys. Rev. B* **82**, 024519 (2010)
10. Marianne Rotter, Marcus Tegel, and Dirk Johrendt, *Phys. Rev. Lett.* **101**, 107006 (2008)
11. D C Johnston, *Advances in Physics 59, 803* (2010)
12. A. Thaler, H. Hodovanets, M. S. Torikachvili, S. Ran, A. Kracher, W. Straszheim, J. Q. Yan, E. Mun,1, and P. C. Canfield, *Phys. Rev. B* **84**, 144528 (2011)
13. Athena S. Sefat, David J. Singh, Lindsay H. VanBebber, Yurij Mozharivskyj, Michae A. McGuire, Rongying Jin, Brian C. Sales, Veerle Keppens, and David Mandrus*,* *Phys. Rev. B* **79**, 224524 (2009)
14. J. S. Kim, Seunghyun Khim, H. J. Kim, M. J. Eom, J. M. Law, R. K. Kremer, Ji Hoon Shim, and Kee Hoon Kim , *Phys. Rev. B* **82**, 024510 (2010)
15. M. G. Kim, A. Kreyssig, A. Thaler, D. K. Pratt, W. Tian, J. L. Zarestky, M. A. Green, S. L. Bud'ko, P. C. Canfield, R. J. McQueeney, and A. I. Goldman, *Phys. Rev. B* **82**, 220503(R)(2010)
16. Sandra Drotziger, Peter Schweiss, Kai Grube, Thomas Wolf, Peter Adelmann, Christoph Meingast, and Hilbert v. Lohneysen, *J. Phys. Soc. Jpn.* **79**, 124705 (2010)
17. Abhishek Pandey, V. K. Anand, and D. C. Johnston, *Phys. Rev. B* **84**, 014405 (2011)
18. Yogesh Singh, A. Ellern and D. C. Johnston, *Phys. Rev. B* **79**, 094519 (2009).
19. Yogesh Singh, M. A. Green, Q. Huang, A. Kreyssig, R. J. McQueeney, D. C. Johnston and A. I. Goldman, *Phys. Rev. B* **80**, 100403(R) (2009).
20. Jiming An, A. S. Sefat, D. J. Singh, and Mao-Hua Du, *Phys. Rev.B* **79**, 075120 (2009)

21. Abhishek Pandey, R. S. Dhaka, J. Lamsal, Y. Lee, V. K. Anand, A. Kreyssig, T.W. Heitmann, R. J. McQueeney, A. I. Goldman, B. N. Harmon, A. Kaminski, and D. C. Johnston, *Phys. Rev. Lett.* **108**, 087005 (2012)
22. W. Krause, G. Nolze, Powder Cell for windows, version 2.3 (1999)
23. A Mani , A.Bharathi , V.S.Sastry , T.S. Radhakrishnan and Y.Hariharan, ICEC18: Proc. 18th Int. Cryogenic Engineering Conf. 2000 ed K G Narayankhedkar (New Delhi: Narosa Publishing House), p 615
24. Dayana Lonappana,b, N.V. Chandra Shekara, T.R. Ravindrana and P. Ch. Sahua, *Mat. Chem. Phys.* **120**, 65 (2010)
25. A. Antal, T. Knoblauch, Y. Singh, P. Gegenwart, D. Wu, and M. Dressel, *Phys. Rev.B* **86**, 014506 (2012)
26. A. P. Hammersley, S. O. Svensson, M. Hansfland, A. N. Fitch, and D. Hausermann, *High Press. Res*. **14**, 235 (1996).
27. A. C. Larson and R. B.V. Dreele, ‘‘*GSAS: General Structural Analysis System*,’’ LANSCE, Los Alamos National Laboratory, 1994.
28. G. N. Peggs, *High Pressure Measurement Techniques*, Applied Sceince Publishers Ltd 1983
29. Francis Birch, *Phys. Rev*. **71**, 809 (1947)
30. Marianne Rotter, Marcus Tegel, Dirk Johrendt, Inga Schellenberg, Wilfried Hermes, and Rainer Pöttgen, *Phys. Rev. B* **78**, 020503(R) (2008)
31. Marcus Tegel, Marianne Rotter, VeronikaWeiß1Falko,M Schappacher, Rainer Pottgen and Dirk Johrendt, *J. Phys. Condens. Matter*. **20**, 452201 (2008)

32. N. V. Chandra Shekar, D. A. Polvani, J. F. Meng and J. V. Badding, *Physica B* **358** 14 (2005)
33. B. K. Godwal, A. Jayaraman, S. Meenakshi, R. S. Rao, S. K. Sikka, and V. Vijayakumar, *Phys.Rev. B* **57**, 773 (1998)
34. Pallavi Teredesaia, D.V.S. Muthua, N. Chandrabhasb, S. Meenakshic, V. Vijayakumarc,P. Modakc, R.S. Raoc, B.K. Godwalc, S.K. Sikkac, A.K. Sooda,b, *Solid State Communications* **129**, 791 (2004)
35. Alka B Garg, Ashok K Verma, V Vijayakumar, R S Rao and B K Godwal, *J. Phys. Condens. Matter.* **18,** 8523 (2006)
36. Chang Liu, Takeshi Kondo, Rafael M. Fernandes, Ari D. Palczewski, Eun Deok Mun, Ni Ni, Alexander N. Thaler, Jörg Schmalian, Sergey L. Bud'ko, Paul C. Canfield & Adam Kaminski , *Nature Physics* **6**, 419 (2010)
37. D. J. Singh, A. S. Sefat, M. A. McGuire, B. C. Sales, D. Mandrus, L. H. VanBebber and V. Keppens, *Phys. Rev. B* **79**, 94429 (2009)
38. J. M. Tranquada, A. H. Moudden, A. I. Goldman, P. Zolliker, D. E. Cox, G. Shirane, S. K. Sinha, D. Vaknin, D. C. Johnston, t M. S. Alvarez, A. J. Jacobson, J. T. Lewandowski, and J. M. Newsam, *Phys. Rev. B* **38**, 2477 (1988)
39. Charles Kittel, *Introduction to Solid State Physics*, (John Wiley & Sons, Inc., Newyork 1976)
40. Awadhesh Mani, Shilpam Sharma, Sharat Chandra and A Bharathi, *J. Phys. Condens. Matter.* **23**, 205802 (2011)
41. Brian C. Sales, Andrew F. May,1 Michael, A. McGuire, Matthew B. Stone, David J. Singh, and David Mandrus, *Phys. Rev. B* **86**, 235136 (2012)

42. H. Fritzsche, *Phys. Rev.* **99**, 406 (1955)
43. J. R. Patterson, C. M. Aracne, D. D. Jackson, V. Malba, S. T. Weir, P. A. Baker and Y. K. Vohra*, Phys.Rev. B* **69**, 220101(R) (2004)
44. Bayrammurad Saparov, Jonathan E Mitchell and Athena S Sefat, *Supercond. Sci. Technol.* **25,** 084016(2012)
45. Huan Li, *Phys.Rev.B* **85**, 134426 (2012)

Chapter 5

High Pressure and Chemical Substitution (Ni) dependent Resistivity behavior of $FeSb_2$

Resistivity behavior of $FeSb_2$ has been investigated as a function of temperature (4.2-300 K), magnetic field (0-12 T) and external pressure (0-8.8 GPa)/chemical substitution with Ni upto 10%. ρ(T) exhibits activated behavior in the range 70 to 300K and variable range hopping behavior(VRH) below 45 K. The activation energy gap(Δ) shows non-monotonic variation with external pressure and shows monotonic increase with Ni content. The VRH hopping parameter T_0 decreases monotonically with increase of pressure/Ni content and disappears beyond 5GPa/5 % Ni. The delocalization of electronic states in the gap with increase of pressure/Ni content leads to an insulator to metal transition (MIT) for pressure ≥ 6 GPa /Ni substitution > 5 %. The magnetoresistance (MR) is found to be positive. The analysis of the resistivity behavior with pressure/Ni and magnetic field indicates that the former induces delocalization, while the latter tends to assist localization of the defect states in the gap of $FeSb_2$.

In this chapter we present the evolution of the ground state properties of a binary pnictide system namely $FeSb_2$ by subjecting it to external pressure as well as chemical substitution by Ni at the Fe site via temperature dependent electrical resistivity studies. $FeSb_2$ is a narrow gap semiconductor which crystallizes in the orthorhombic marcasite structure with space group symmetry *Pnnm* [1, 2]. Based on the similarities of its physical properties with that of FeSi, this material is proposed to be another d-electron based Kondo insulator. The energy gap is found to be ~ 300 K from the resistivity measurements, which is in good agreement with the optical spectroscopy measurements [1-6]. However optical spectroscopy indicates the presence of strong correlations in this system [5, 6]. Chemical substitutions of different elements at the Fe and Sb sites have been performed to study the evolution of ground state properties of $FeSb_2$ [7-11]. Substitution with Te at Sb site shows metallicity for concentrations less than 20 % at low temperatures below 200 K [7]. The energy gap in the insulating regime does not show systematic variation [7]. With Co substitution, the system shows metallic behavior with weak ferromagnetism for concentrations up to 50% [8, 9]. Hole doping with Sn at the Sb site transforms $FeSb_2$ in to a heavy fermion metal [10]. With hole doping by Cr at the Fe site, the system evolves from paramagnetic to antiferromagnetic semiconductor [11]. For smaller concentrations up to 20% it also shows metallic behavior along the b-axis in the paramagnetic region [11]. First principles calculations using Density functional Theory (DFT) predicted that within the marcasite structure the energy gap increases with increase of pressure up to 10 GPa and then decreases leading to the appearance of weak metallicity [12]. Although the substitutions with Co and Te are equivalent to applying chemical pressure in the system; the energy gap variation is not concomitant with the calculations. High pressure measurements are very good tools to study the evolution of ground state of a system as they do not introduce any chemical complexity, charge carriers / defects in the system to modify the electronic structure unlike the chemical substitution. Initial High pressure x-ray diffraction (HPXRD) measurements performed on $FeSb_2$ did not show any structural phase transition up to a pressure of 7 GPa [2]. The subsequent HPXRD measurements confirmed retention of the orthorhombic phase of $FeSb_2$ even up to a pressure of ~28 GPa.[13] which is in consonance with the theoretical calculations predicting structural transition only beyond a pressure of 38 GPa [12]. While structural properties of $FeSb_2$ under pressure has been well studied, high pressure transport studies examining the evolution of its insulating ground state properties into a possible metallic state has not yet been investigated.

In the present study we explore the possibility of pressure induced insulator to metal transition in $FeSb_2$ by performing temperature dependent electrical resisitivity studies up to an external pressure of 8.8 GPa, within which the system retains its orthorhombic marcasite structure. Our studies indeed reveal a pressure induced insulator to metal transition whose details will be presented in this chapter. Having studied the effect of lattice contraction by external pressure on pristine sample and observing an insulator to metal transition, it was of interest to enquire whether substitution of Fe by an appropriate element having smaller atomic radius and capable of donating extra electron to the system can induce metallicity in this system. Toward achieving this objective, we chose Ni substitution forming $Fe_{1-x}Ni_xSb_2$ system owing to the fact that the atomic size of Ni is smaller than Fe which in addition to mimicking the effect similar to external pressure also can donate two extra electrons to the system. Polycrystalline $Fe_{1-x}Ni_xSb_2$ samples were synthesized using solid state method as described in detail in chapter 2. Room temperature XRD measurements were carried out using Cu Kα radiation using Bragg-Brentano geometry. The composition was determined by energy dispersive X-ray spectroscopy. High pressure resistivity measurements were carried out in home-built, opposed anvil pressure locked cell using steatite as a pressure transmitting medium and pyrophyllite washers as the gaskets. Magnetoresistance measurements were carried out from 0 to 12 T in the home built exchange gas cryostat.

5.1 Structural Characterization

Figure 5.1 shows the room temperature X-ray diffraction (XRD) patterns of $Fe_{1-x}Ni_xSb_2$ obtained from STOE X-ray diffractometer for x = 0, 0.02, 0.05 and 0.1. The diffraction peaks could be indexed to orthorhombic marcasite structure with space group *Pnnm* (space group number 58). The samples are found to be single phase and are isostructural to $FeSb_2$ with the marcasite structure. The unit cell parameters are refined using

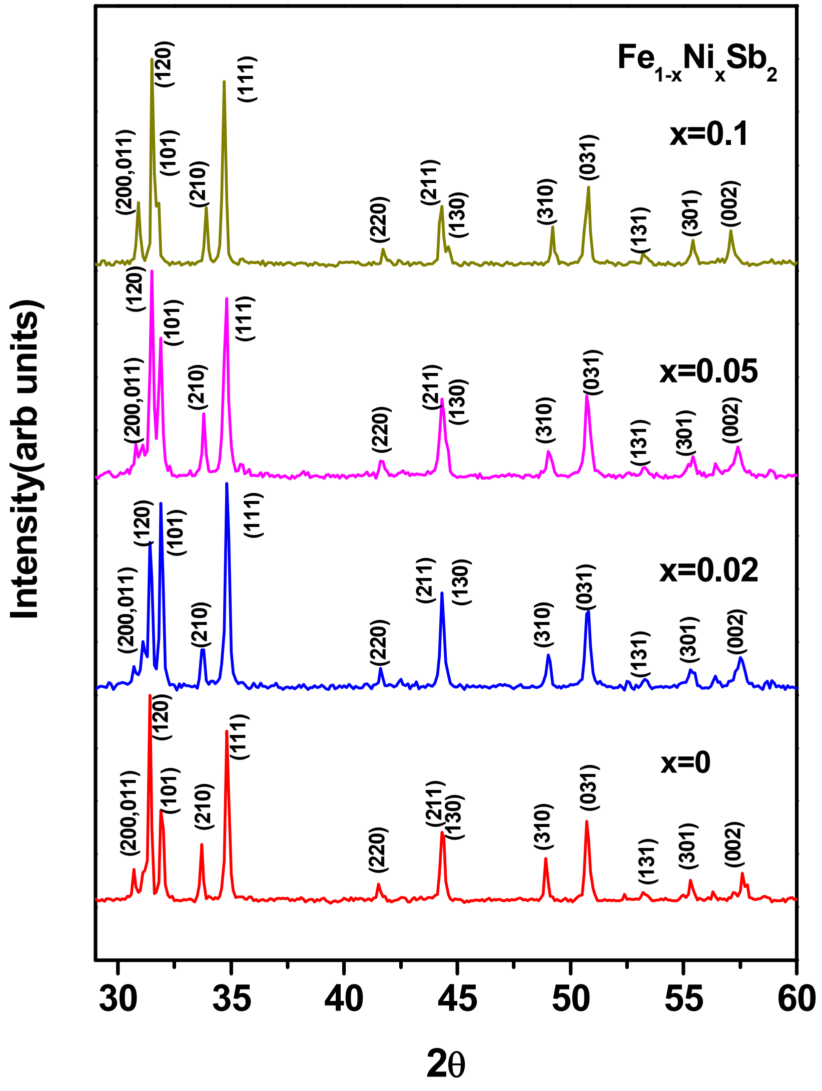

Figure 5.1: XRD patterns for powder $Fe_{1-x}Ni_xSb_2$ samples, indexed to *Pnnm* symmetry. The intensity is normalized to the maximum value. For successive changes in Ni fraction, the XRD patterns are shifted along the intensity axis for clarity.

STOE software. The orthorhombic lattice parameters of the pristine $FeSb_2$ are found to be *a* = 5.8218(18) Å, *b* = 6.527(4) Å and *c* = 3.1944(10) Å which are in very good agreement with the reported values [1, 2].

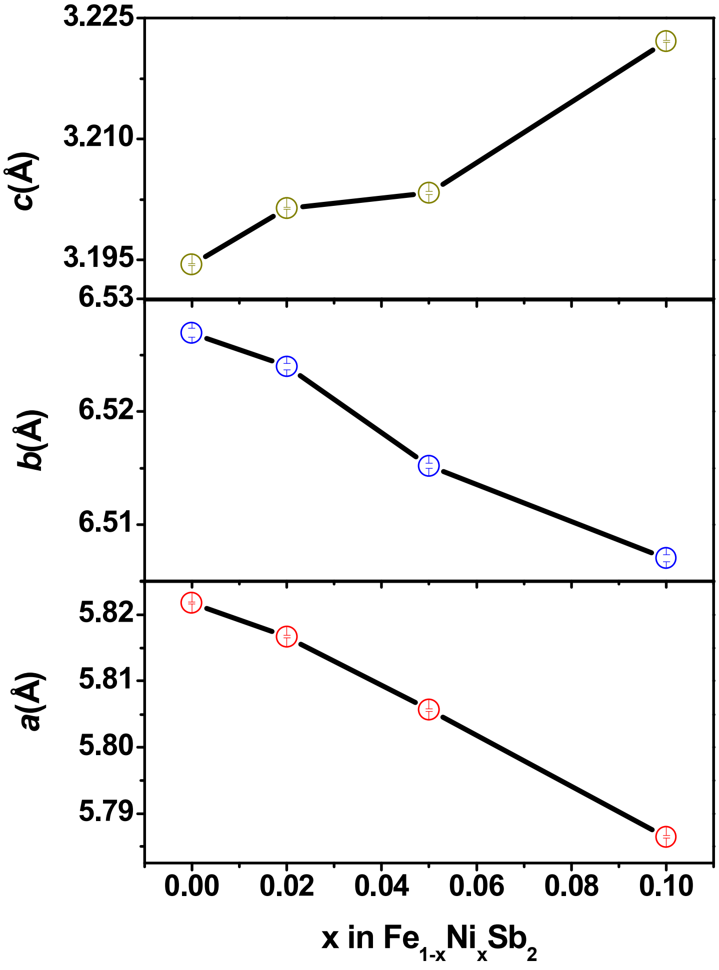

Figure 5.2: The variation in lattice parameters with Ni content x for $Fe_{1-x}Ni_xSb_2$

The variation of lattice parameters *a, b* and *c* with Ni content x are shown in Fig 5.2. The lattice parameters *a* and *b* systematically decrease with increase of Ni content while lattice parameter *c* increases with increase of x as per Vegard’s law indicating random solid solution. The decrease in lattice parameters *a* and *b* is consistent with the smaller ionic radius of Ni as compared to Fe.

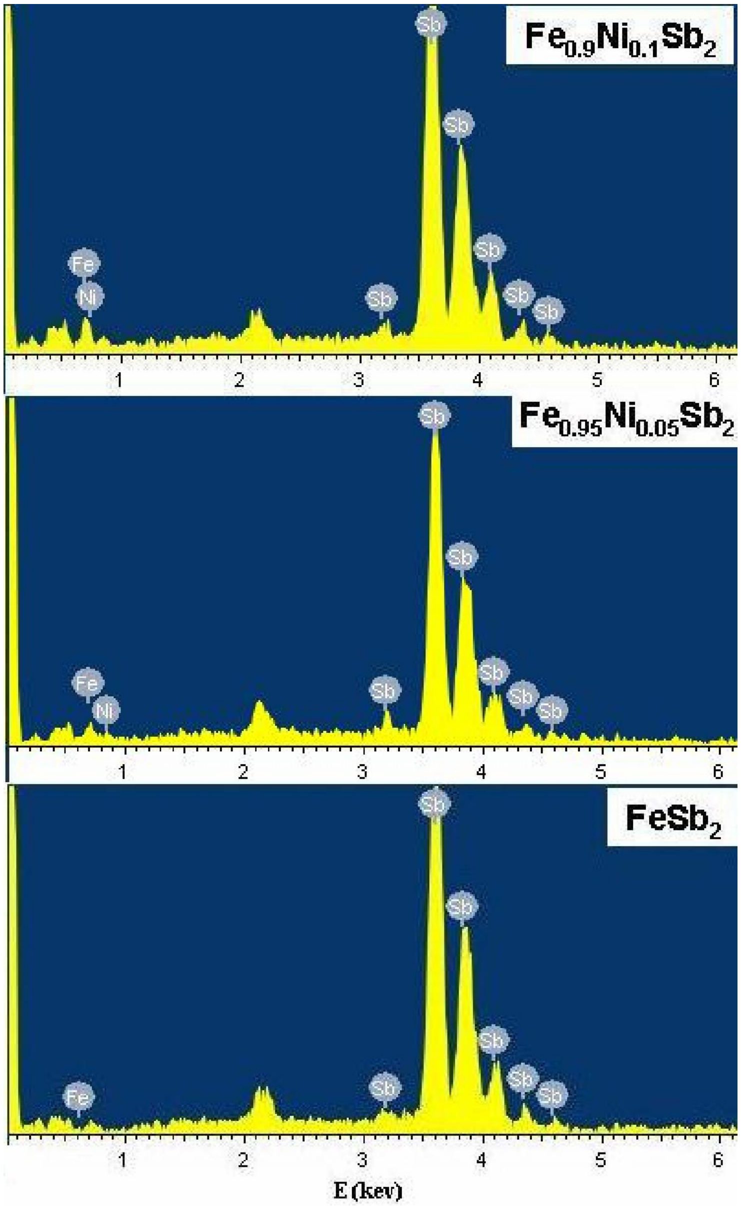

Figure 5.3: EDX spectra taken on $Fe_{1-x}Ni_xSb_2$ polycrystals for x = 0.0, 0.05 and 0.1

Energy dispersive X-ray spectroscopy (EDX) measurements were carried out using Zeiss Supra 55 scanning electron microscope to find the Ni content of $Fe_{1-x}Ni_xSb_2$. Fig 5.3 shows representative EDX spectra for x = 0, 0.05 and 0.1. The spectra show peaks corresponding to elements of Fe and Sb for x = 0 and Fe, Ni and Sb for x = 0.05 and 0.1. No impurity elements were observed indicating the samples are pure. The estimated Ni composition from EDX measurements are presented in Table 1. It can be seen from the table that the nominal composition matches very well with the actual composition values.

Nominal composition	Fe (at %)	Ni (at %)	Sb (at %)	actual composition
$FeSb_2$	33	0	67	~ $FeSb_2$
$Fe_{0.95}Ni_{0.05}Sb_2$	30	2	68	~ $Fe_{0.94}Ni_{0.06}Sb_2$
$Fe_{0.9}Ni_{0.1}Sb_2$	29	4	67	~ $Fe_{0.88}Ni_{0.12}Sb_2$

Table1: Estimated Ni content from EDX measurements for nominal x = 0.0, 0.05 and 0.1 of $Fe_{1-x}Ni_xSb_2$

5.2 Studies on Pristine $FeSb_2$

5.2.1 Resistivity behaviour of $FeSb_2$

Figure 5.4a shows the variation of electrical resistivity (ρ) as a function of temperature for $FeSb_2$ in the range 4.2 K to 300 K. ρ(T) is seen to increase with decrease of T displaying negative temperature coefficient from 4.2 to 300 K. Since the measurements were carried out on the pellets of powder samples, the extent of variation of resistivity from 300 K to 4.2 K is observed to be two orders of magnitude which is smaller than the change seen in the single crystals [1, 2] however, it is similar to that results observed in polycrystalline $FeSb_2$ [10]. It can be seen from the Fig 5.4 a that the ρ(T) shows three distinct behaviors in the studied temperature range. (i) The high temperature (HT) regime ($T > 60$ K) where ρ(T) exhibits activated behavior (ii) the intermediate temperature (IT) regime ($10 < T < 45$ K) , in which ρ(T) is governed by variable range hopping (VRH) behavior and (iii) low temperature region (T < 10 K) where ρ(T) does not follow activated or VRH behavior, however conductivity varies linearly with T in this regime as shown in inset of Fig 5.4 a. In the HT range, for T > 60 K, the activation energy was deduced by fitting ρ(T) data to the Arrhenius equation

$$\rho(T) = \rho_0 \exp(\Delta / 2k_B T) \qquad (1)$$

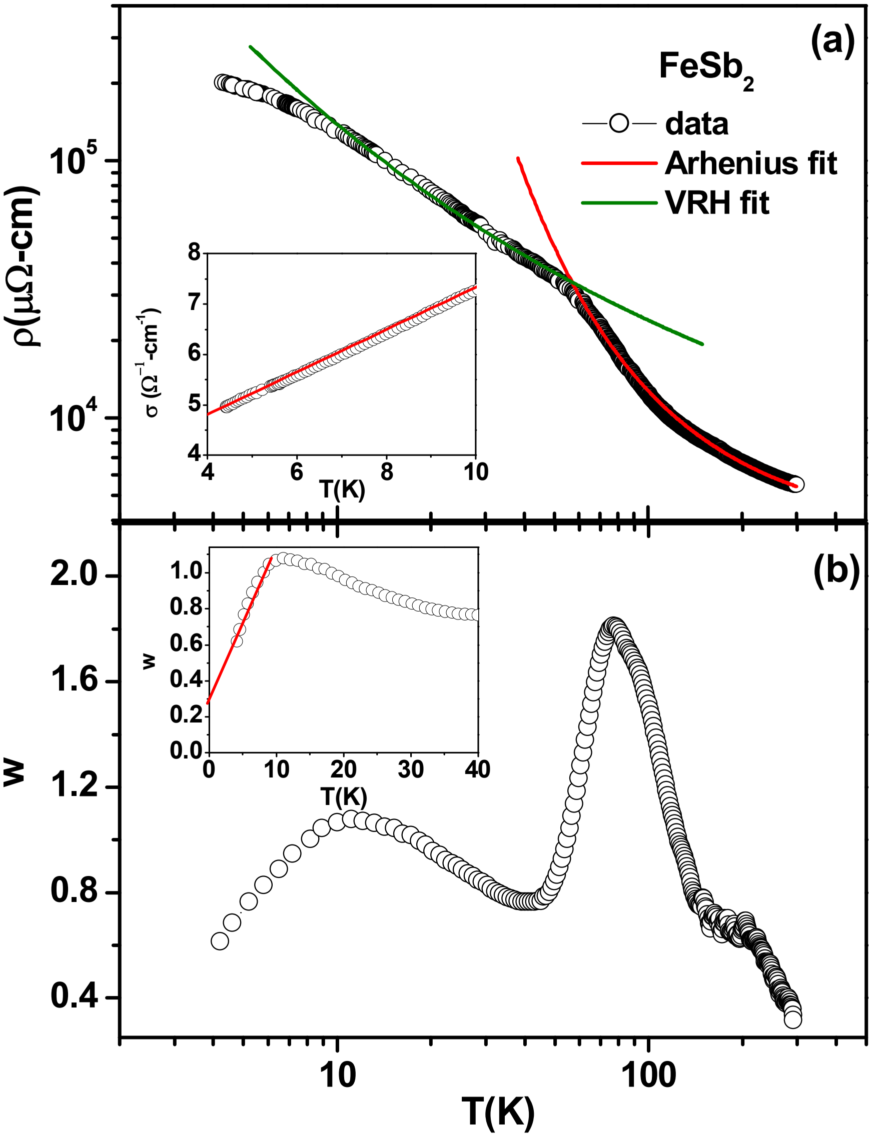

Figure 5.4: (a) The variation of resistivity with temperature for $FeSb_2$ polycrystal. The red and green solid lines indicate the Arrhenius and VRH fits as described in the text. The inset show the conductivity versus temperature below T = 10 K.

(b) w= dlnσ/dT versus T plot as described in the text. The inset shows enlarged view of variation of w (T) in the temperature range 0 to 40 K.

where Δ is the energy gap and k_B is the Boltzmann constant. The Δ deduced from the Arrhenius fit is found out to be 255 K which is in very good agreement with the previous reports [1, 10]. In the IT range of 10-45 K, the ρ(T) data does not follow activated behavior and it fits to Mott VRH equation

$$\rho(T) = \rho_0 \exp([T_0 / T]^{1/4}) \qquad (2)$$

where T_0 is the hopping parameter and is given by the relation

$$T_0 = p / N_F k_B \xi^3 \qquad (3)$$

where p ~ 21 is a dimensionless constant [15], N_F is the density of states in the gap and ξ is the localization length. The VRH behavior indicates the presence of localized states inside the gap due to the presence of disorder. As the VRH behavior is related to the quality of the sample, we have investigated the resistivity behavior of various batches of $FeSb_2$ samples. The VRH parameters deduced from the resistivity data in the IT regime for different samples were found to be T_0 ~ 1890-1995 K, indicating reproducible good quality of the samples. The sample with T_0 ~ 1995 K was chosen for the rest of the studies reported in this chapter.

5.2.2 Logarithmic Derivative plot analysis of ρ(T) data

The logarithmic derivative of conductivity, i.e., w(T) = dln(σ(T))/dln(T) versus temperature plot analysis [14] provides a very useful method to discriminate metallic and insulating samples at low temperatures. Ideally a material is defined as a metal if it has finite conductivity at zero temperature, i.e., $\sigma \neq 0$ at T = 0 K and for an insulating material, the conductivity is zero at T = 0 K. In reality, the experimental measurements of σ(T) terminate at finite temperatures, necessitating extrapolation of σ up to T = 0 K to identify the nature of conduction [14]. In the presence of disorder, it is quite difficult to clearly identify the metal-insulator transition MIT from simple zero temperature extrapolation of σ (T) [14]. However, MIT can be identified with least ambiguity from w(T) plot analysis [14] which we demonstrate by following examples.

In the presence of disorder conductivity exhibits exponential T dependence like VRH behavior in insulating regime and a power law behavior in the metallic regime [14]. For a material exhibiting VRH behavior

$$\sigma(T) = \sigma_0 \exp(-[T_0 / T]^{1/4}) \qquad (4)$$

gives $\sigma = 0$ at $T = 0$ K, indicating sample is insulating. Similarly for a material exhibiting activated behavior

$$\sigma(T) = \sigma_0 \exp(-\Delta_0 / k_B T) \qquad (5)$$

shows $\sigma = 0$ at $T = 0$ K. On the other hand, considering that the temperature dependence of σ follows a power law behavior,

$$\sigma(T) = a + bT^P \qquad (6)$$

with a >0, 'b' a positive or negative value and exponent 'p', a positive number results in $\sigma \neq 0$ at $T = 0$ K, indicating metallic behavior of the sample. Taking the logarithmic derivative $w(T) = d\ln(\sigma(T))/d\ln(T)$ of Eq (4) and Eq (5) results in $w(T) = 1/4.[T_0/T]^{1/4}$ and Δ/T respectively for the insulating samples, implying that $w(T) \rightarrow \infty$ as $T \rightarrow 0$ K. Where as if the conduction is metallic, one gets from Eq (6), $w(T) = pbT^p/(a+bT^p)$. Here $w(T) \rightarrow 0$ as $T \rightarrow 0$ K. In fact w(T) is an increasing function of temperature i.e. $dw/dT > 0$ for metallic conduction, whereas for insulating samples w(T) decreases with increasing temperature, i.e., $dw/dT \leq 0$. These properties of w(T) are very useful in identifying MIT.

Figure 5.4 b shows the plot of w versus T deduced from σ(T) of $FeSb_2$. All the three regimes of transport are clearly captured in this plot. The negative slope of d*w*/dT in the 70-

300 K range indicates the activated conduction regime while the emergence of positive slope in the 50-70 K range indicates the admixture of the activated and VRH regimes in which the former progressively vanishes at the cost of the latter. The slope becomes again negative in 10-45 K range where the VRH conductivity fully dominates. Below 10 K, d*w*/dT again becomes positive consistent with the power law behavior. The inset in Fig 5.4 b shows the enlarged view of *w* in the 10-40 K range. It can be seen the extrapolated *w* has a non zero value for T → 0 K which indicates that the ground state of $FeSb_2$ is non-metallic at ambient pressure.

5.2.3 Magnetoresistance behaviour of $FeSb_2$

The temperature dependent resistivity at various magnetic fields for $FeSb_2$ from 0 to 12 T is shown in Fig 5.5 a. The magneto resistance (MR) is positive and decreases with increase of temperature. The effect of magnetic field is strong in LT regime and weak in the in the IT regime as shown in the inset of Fig 5.5a. In the HT regime, MR is found to be very small. In the LT regime, the σ(T) behavior exhibits linear T dependence at different fields as shown in the Fig 5.5b. In the IT regime, the VRH behavior persists and overall R(T) increases with increase of field. This gives rise to a marginal positive MR which is evident from the linearity of the R versus $T^{-1/4}$ plot as shown in the Fig 5.5c.

The positive MR in the VRH regime can be understood based on the Shklovskii-Efros model [15], according to which under magnetic field the wavefunction of the localized electrons are squeezed in the transverse direction leading to a sharp decrease in overlap of the neighboring wavefunction tails which helps in further localization of states giving rise to a

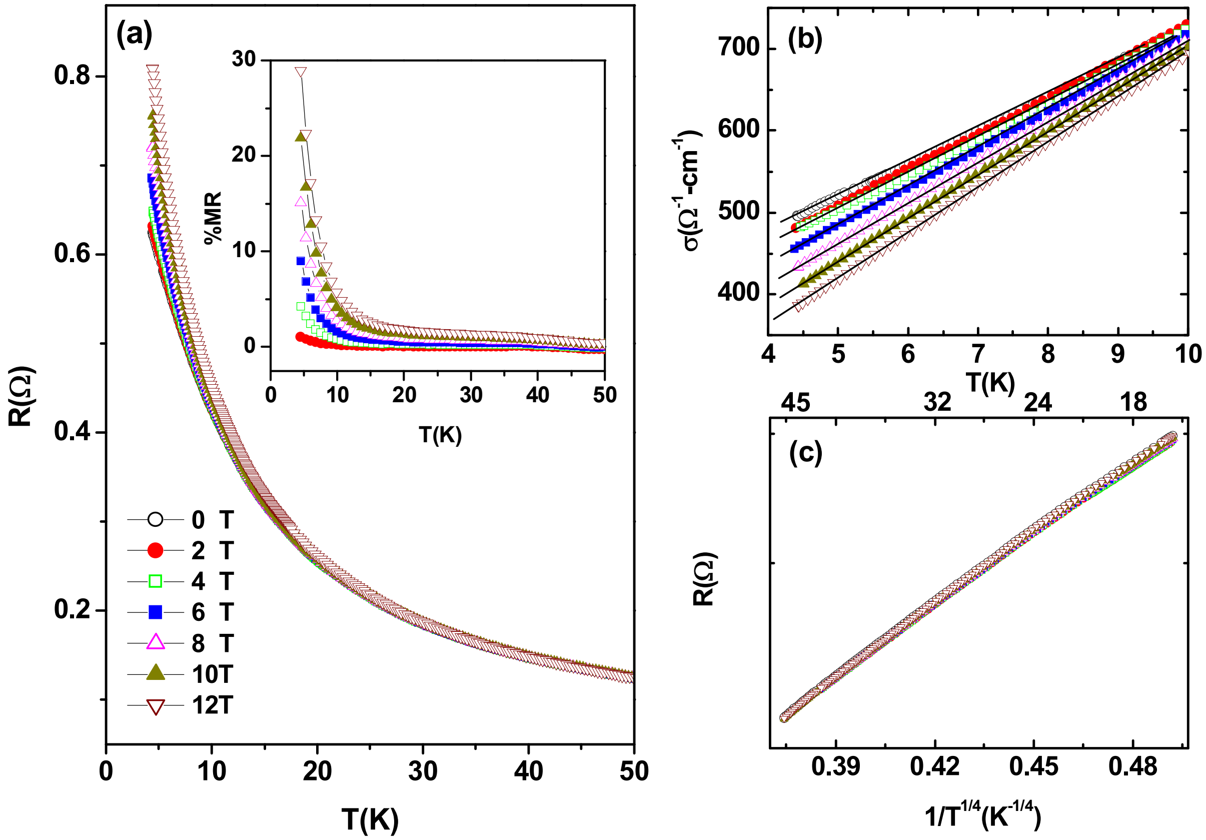

Figure 5.5: (a) The variation of resistance with temperature for $FeSb_2$ polycrystal at different magnetic fields B = 0, 2, 4, 6, 8, 10 and 12 T. The inset shows the variation of MR with T.
(b) The linear Conductivity σ(T) at different magnetic fields from 0 to 12 T in the LT regime
(c) ln R versus $1/T^{1/4}$ at different magnetic fields from 0 to 12T in the IT regime indicating the VRH type behavior.

positive MR. This can be expressed in terms of the following equation [15]:

$$\ln(\rho(B)/\rho(0)) = \alpha B^2 \qquad (7)$$

where $\alpha = t_1 e^2 \xi^4 \hbar^{-2} (T_0 / T)^{3/4}$, t_1 = 2.4 x 10^{-3} and T_0 is taken as the value of the hoping energy at B = 0T [16]. Isothermal MR measurements were carried out in the VRH regime and Fig 5.6 shows ln(ρ(B)/ρ(0)) versus B^2 at different fixed temperatures. The slope α has been deduced from the linear fits. The inset in Fig 5.6 shows the variation of α with $(T_0/T)^{3/4}$. The data could be fitted to a linear equation and the slope (β) is found to be 5.476 x 10^{-6} T^{-2}. From the value of the slope $\beta = t_1 e^2 \xi^4 \hbar^{-2}$, the localization length (ξ) is found to be ~ 55.8 Å. The localization length (ξ) is clearly 8.5 times larger than the largest lattice parameter of the $FeSb_2$ unit cell. This indicates that the wave functions of the localized carriers spreads over several unit cells of the system. Using the value of ξ in Eq (3), the value of density of states (DOS) of the localized states N_F is deduced to be 7.08 x 10^{20} $eV^{-1}cm^{-3}$.

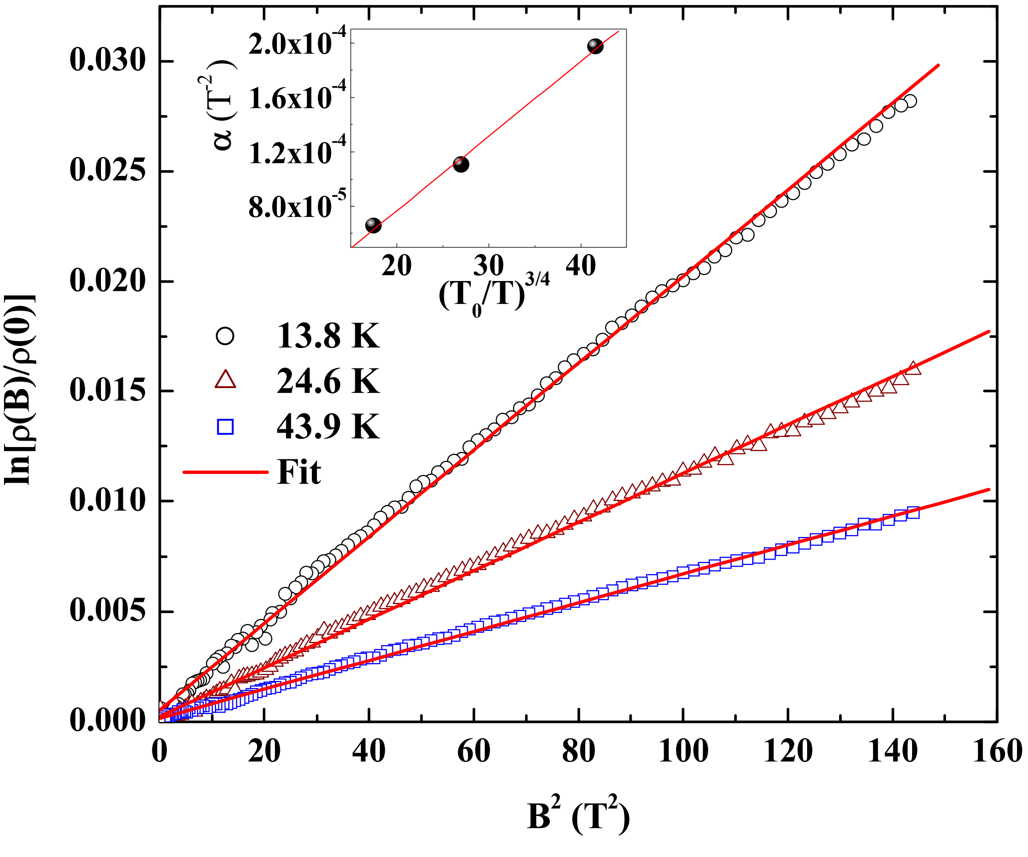

Figure 5.6: ln(ρ(B)/ρ(0)) versus B^2 for $FeSb_2$ at three different temperatures in the VRH regime. Symbols are experimental data points and red solid lines are linear fits. slope (α) has been deduced from these linear fits. The insets shows a linear plot of α versus $(T_0/T)^{3/4}$

5.2.4 Pressure dependant Resistivity behavior of FeSb$_2$

Figure 5.7 (a)-(f) show temperature dependent normalized electrical resistivities (ρ(T)/ρ(300 K) at different pressures from 0 to 8.8 GPa. The effect of pressure on ρ(T) is observed to be very peculiar in different pressure regimes. In the HT regime, the overall resistivity is observed to increase with increase of pressure up to ~ 6 GPa and decrease beyond this pressure. ρ(T) shows activated behavior in this regime although the temperature range of activation reduces from 60-300 K at 0 GPa to 165-300 K at 7 GPa with increase of pressure. This is evident from the ln ρ(T) versus 1/T plots as shown in the insets (i) of Fig 5.7 (a)- (e) at different pressures which are linear. The energy gap Δ has been obtained from the slopes of the linear fits and the variation of energy gap has been depicted in Fig 5.8(a) as a function of pressure up to 7.8 GPa. It is observed that the energy gap Δ initially increases from 255 K at 0 GPa to 310 K at 6.2GPa and then decreases to 160 K at 7.8 GPa. The non monotonic variation of energy gap with increase of pressure is in agreement with the band structure calculations on FeSb$_2$ [12]. At the pressure of 8.8 GPa, ρ(T) shows positive temperature coefficient of resistivity for $T < 240$ K and insulating behavior persists above this temperature.

Contrary to the increase in overall resistivity in the HT regime, it decreases with increase of pressure in the IT and LT regimes. In the IT regime, the VRH behavior persists only up to 5 GPa. This is evident from the ln ρ(T) versus $T^{-1/4}$ plots shown in the insets (ii) of Fig 5.7 (a)- (c). The value of the hopping parameter T_0 has been deduced from the linear fits and the variation of T_0 is plotted as a function of pressure in Fig 5.8 b. It is observed that the hopping parameter T_0 decreases with increase of pressure up to 5 GPa and vanishes beyond this

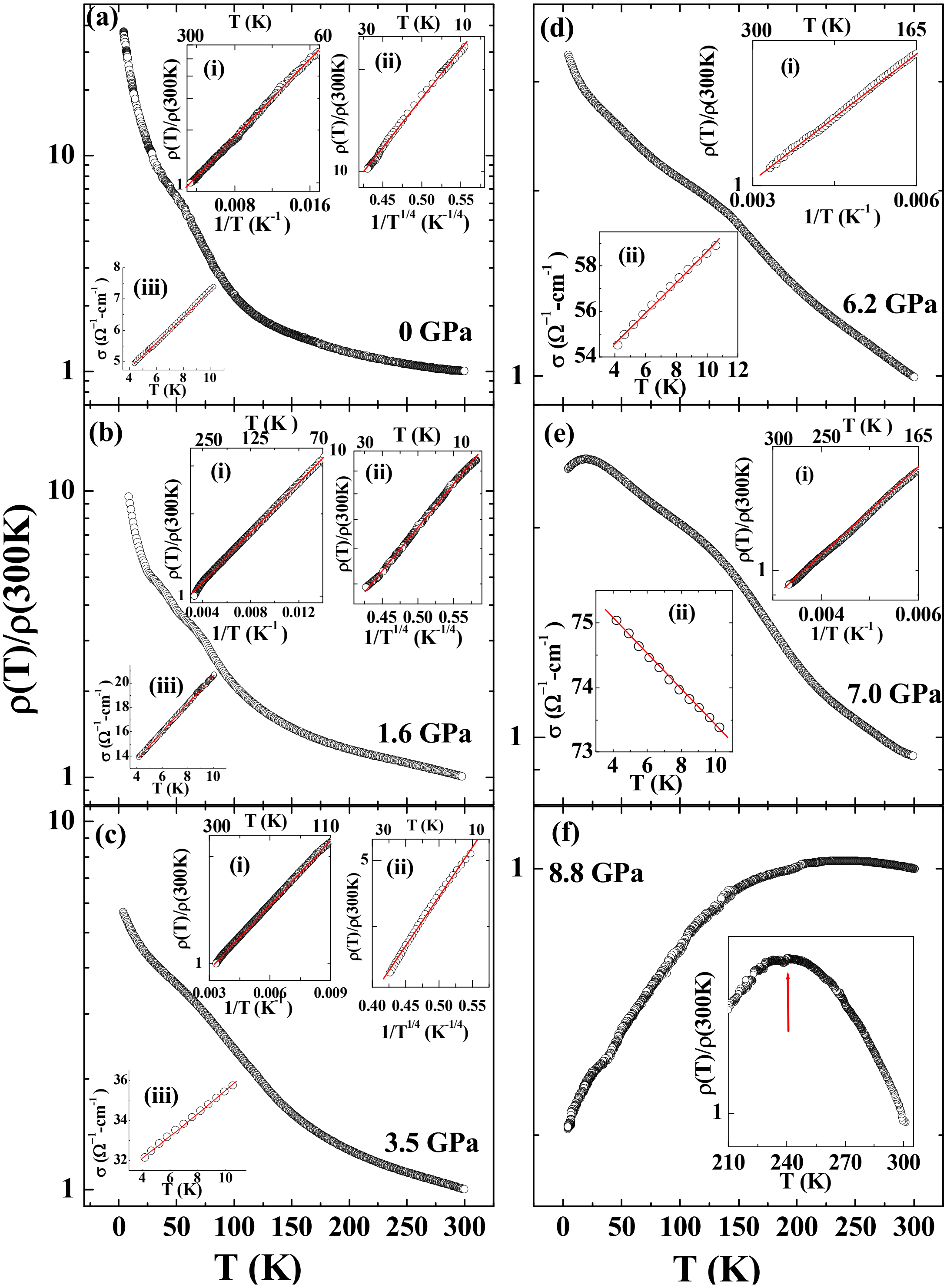

Figure 5.7: (a)-(f) Temperature dependent normalized resistivities $\rho(T)/\rho(300\ K)$ at different pressures from 0 to 8.8 GPa. Insets (i) in (a)-(e) are ln $\rho(T)/\rho(300\ K)$ versus T^{-1} plots to extract energy gap Δ in the HT regime at various pressures. Insets (ii) in (a)-(c) are ln $\rho(T)/\rho(300\ K)$ versus $T^{-1/4}$ plots to extract T_0 in the VRH regime. Insets (iii) in (a)-(c) are linear dependence of conductivity σ in the LT regime. The solid lines are fits. The inset in (f) exhibits a closer view of MIT in an expanded temperature scale.

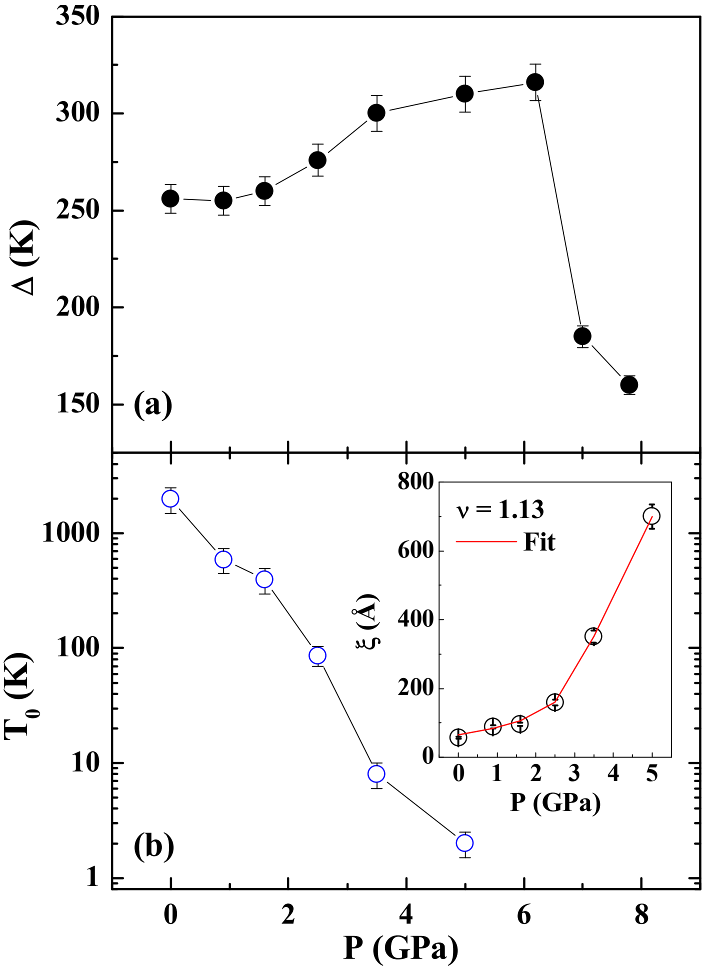

Figure 5.8: (a) Variation of energy gap Δ with pressure for $FeSb_2$.Solid lines are guides to the eyes (b) Variation of hopping parameter T_0 with pressure. The inset shows localization length (ξ) versus P plot. The solid line is the fit to equation $\xi \ \alpha \ | P\text{-}P_c|^{-\nu}$

pressure. Assuming that the value of N_F does not change under pressure the value of localization length ξ was calculated at different pressures using equation (3). This assumption is based on the fact that the external pressure does not introduce disorder or additional defect states inside the gap unlike the chemical pressure as long as the crystal structure is retained. The value N_F obtained from MR analysis was used. It is found that the localization length ξ increases from 55.8 Å to 700 Å as the pressure increases from 0 to 5 GPa as shown in the inset of Fig 5.8 b. This result indicates that pressure induced metal to insulator (MIT) transition observed at low temperatures is a consequence of delocalization of localized states as these states overlap under pressure giving rise to a broad impurity band.

5.2.5 Logarithmic Derivative plot analysis of ρ(P,T) data

To find the pressure at which the MIT occurs, w(T) has been calculated at different pressures and it is shown in Fig 5.9. w(T) shows a minima at about T ~ 45 K at ambient pressure below which VRH regime sets in. This minimum shifts to lower temperature with

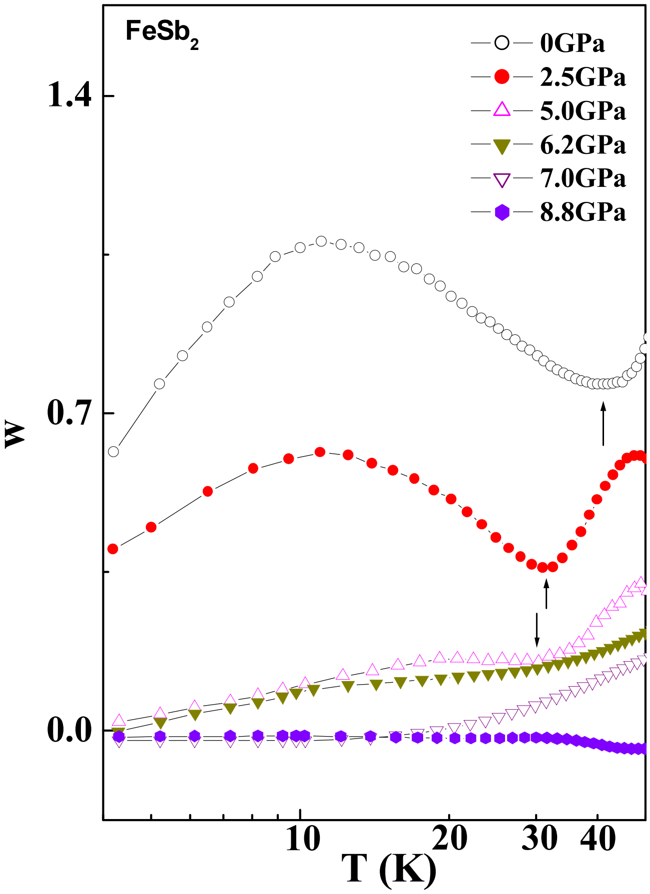

Figure 5.9: w versus ln(T) plots at different pressures to find the pressure at which MIT occurs

increase of pressure and vanishes above P ~ 5 GPa. This behavior is expected since the characteristic hopping energy T_0 tends to zero as the MIT is approached, so the hopping dominates at lower and lower temperatures [14]. From the Fig 5.9 it is clear that for P ~ 6 GPa, w(T) tends to zero as $T \rightarrow 0$ indicating that the MIT occurs at about 6 GPa. It should be noted that a clear MIT is observed at P ~ 7 GPa with transition temperature T_{MIT} ~ 20 K as shown in Fig 5.7e. The MIT transition increases from 20 K to 250 K as the pressure increases from 7GPa to 8.8 GPa. But a complete metallization in the temperature range of investigation is not observed up to the maximum pressure of 8.8 GPa. The electrical conductivity σ versus T plot in the LT regime below 10 K is shown in the insets (iii) of Fig 5.7 (a)-(c) and insets (ii) of (d) and (e) which clearly exhibits the linear T dependence of conductivity at various pressures.

5.2.6 Analysis of Pressure Induced Metallization of $FeSb_2$

In order to get further insight into the metal insulator transition, the present results are analyzed in terms of the scaling theory of localization [16-19]. According to this theory, as the MIT transition is approached from metallic side, the zero temperature conductivity σ_0 is expected to vanish according to the equation

$$\sigma_0 \ \alpha \ | P-P_c |^{\mu} \qquad (8)$$

where P is the control parameter which is pressure in the present case. P_c is the critical pressure at which MIT occurs and μ is the critical exponent. On the other hand if the transition is approached from insulating side then the localization length ξ diverges as

$$\xi \ \alpha \ | P-P_c|^{-\nu} \qquad (9)$$

where ν is the critical exponent and usually $\mu = \nu$ [17]. The theoretically predicted value of $\mu = 1$ [19] for non-interacting electrons for dimension $d > 2$ is generally attributed to Anderson transition while the exponent 1/2 ascribed to the presence of local magnetic moments induced by Coulomb interaction [17]. Since the measurements were carried out up to 4.2 K, it is not reasonable to linearly extrapolate σ (T) down to T = 0 K to get σ_0 at various pressures. But, the ξ versus P data in insulating regime ($P < P_c$) have been best fitted to equation (9) as shown in the inset of Fig 5.8 b. The value of ν obtained from the fit is 1.13 which is close to 1. This indicates that the MIT in $FeSb_2$ is of Anderson type.

5.3 Effect of Ni substitution on $FeSb_2$

5.3.1 Resistivity behavior of $Fe_{1-x}Ni_xSb_2$

Figure 5.10 shows the temperature dependent resistivity $\rho(T)$ for x = 0.02, 0.05 and 0.1 of $Fe_{1-x}Ni_xSb_2$ in the range 4.2 to 300 K. For x = 0.02 and 0.05, $\rho(T)$ shows resistivity behavior similar to $FeSb_2$. For x = 0.1 sample, a metal to insulator transition is observed at T_{MIT} ~ 85 K. For x = 0 to 0.02, the HT regime exhibits activated behavior and fits to Arrhenius equation (1). As the Ni concentration increases the temperature range of activation decreases as shown in the Fig 5.10 similar to the effect observed for application of pressure. The variation of energy gap as a function of x is shown Fig 5.11a. The energy gap increases from 255 K to 540 K as x increases from 0 to 0.1. In the IT regime, x = 0.02 and 0.05 samples exhibit variable range hopping (VRH) behavior and fits to the equation (2) similar to the behavior observed in the pristine sample $FeSb_2$. The value of T_0 obtained from the fits decreases drastically from 1995 K to 3 K as x increases from 0 to 0.05 as shown in Fig 5.11b and vanishes beyond x > 0.05. This indicates delocalization of defect states on account of Ni substitution which eventually give metallicity for x = 0.1 for T < 85 K.

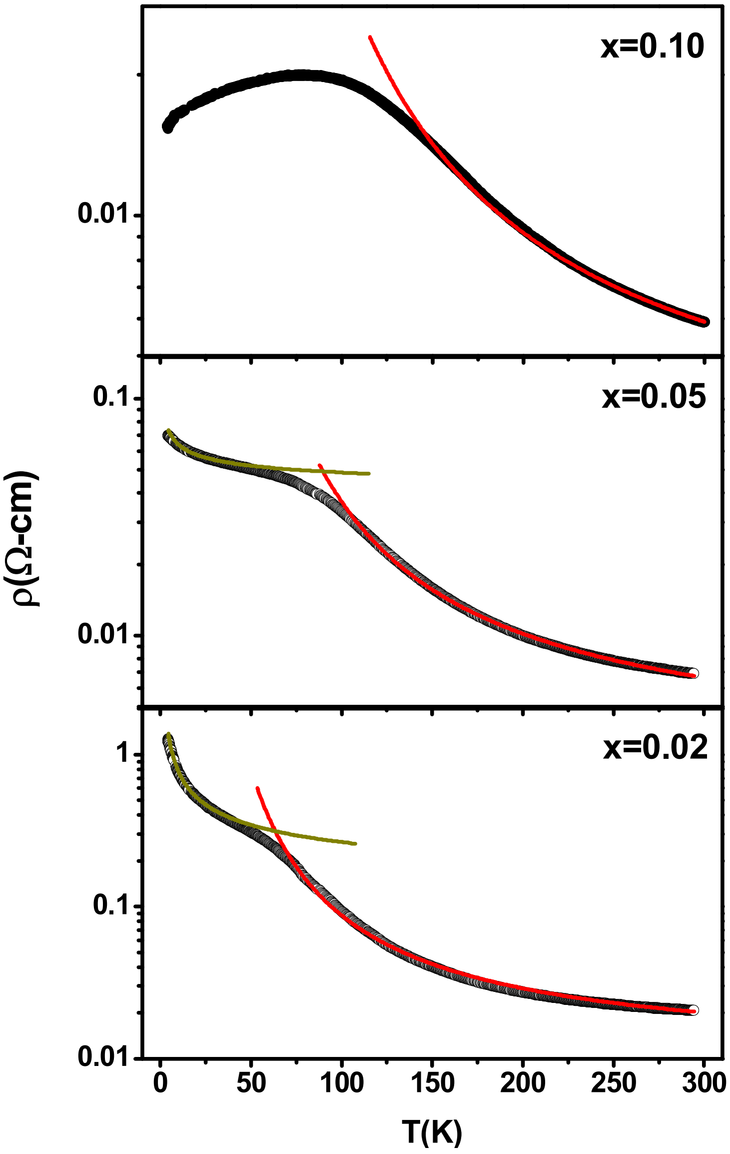

Figure 5.10: ρ versus T for $Fe_{1-x}Ni_xSb_2$ in the range 4.2 to 300 K for x = 0.02, 0.05 and 0.1. red and green solid lines are fits to Arrhenius and VRH behavior.

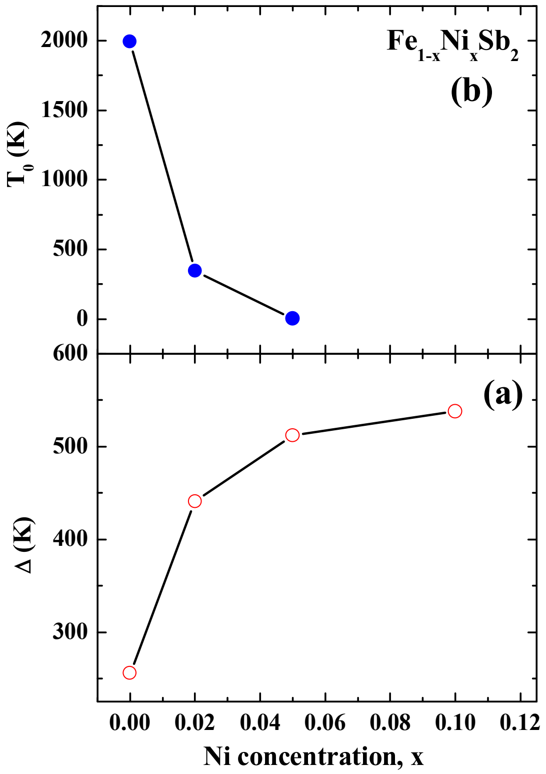

Figure 5.11: Variation of (a) energy gap Δ and (b) hopping parameter T_0 as a function of Ni content x

5.3.2 Magneto Resistance behavior of $Fe_{1-x}Ni_xSb_2$

Figure 5.12 shows the temperature dependant resistance of $Fe_{1.95}Ni_{0.05}Sb_2$ in the range 4.2 to 50 K for the applied magnetic fields of 0, 6 T and 12 T. It is evident from the inset (a) of Fig 5.12 that the MR of $Fe_{1.95}Ni_{0.05}Sb_2$ is positive and it decreases with increasing temperature, exhibiting similarity with that observed for the pristine $FeSb_2$. In the IT range, VRH behavior persists and the overall resistance R increases with increase of field. This is evident from the linearity of R versus $T^{-1/4}$ plot as shown in the inset Fig 5.12 (b). The positive MR in the VRH regime has been analyzed using Shklovskii-Efros model as described for $FeSb_2$. Fig 5.13 shows the variation of $\ln(\rho(B)/\rho(0))$ as a function of B^2 at three different

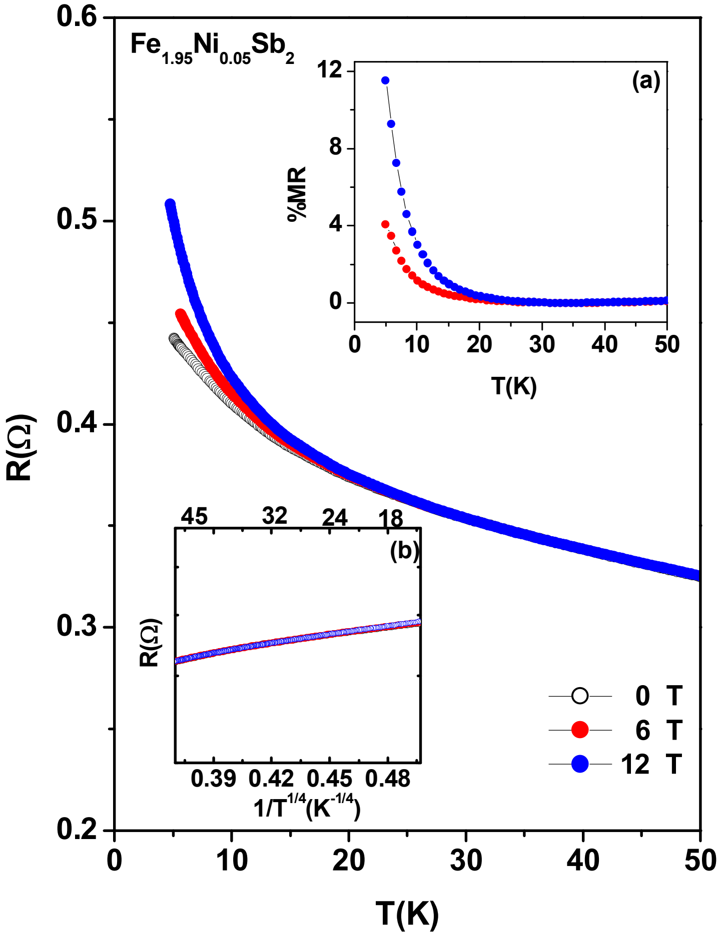

Figure 5.12: Variation of resistance with T at B = 0, 6 and 12 T for $Fe_{0.95}Ni_{0.05}Sb_2$. inset (a) shows variation of MR with T for 6 and 12T and inset (b) shows ln(R) versus $1/T^{1/4}$ at B = 0, 6 and 12T indicating VRH behavior

temperatures 13.8, 24.6 and 43.9 K in the VRH regime. ln(ρ(B)/ρ(0)) varies linearly with B^2 at all the measured temperatures. The slope (α) has been found using linear fits. The inset in the Fig 5.13 shows the variation of slope (α) as a function of $(T_0/T)^{3/4}$ which is seen to be linear. The slope of this linear equation (β) is found to be 3.571 x 10^{-4} T^{-2}. From the value of β ($=t_1 e^2 \hbar^{-2} \xi^4$), the localization length (ξ) is found out to be 498 Å which is nine times larger than the localization length (55.8 Å) of $FeSb_2$. The observed increase in ξ for $Fe_{0.95}Ni_{0.05}Sb_2$

compared to $FeSb_2$ suggests the increase in spatial extent of the wavefunction of localized states, which can arise on account of increase in disorder caused by the Ni substitution.

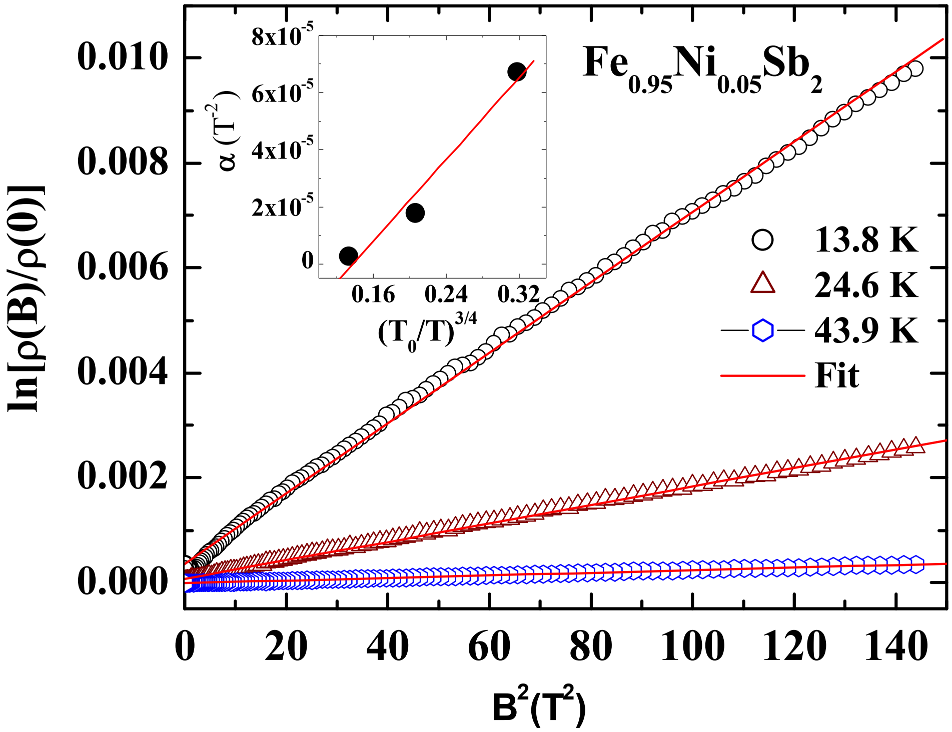

Figure 5.13: ln(ρ(B)/ρ(0)) versus B^2 for $Fe_{0.95}Ni_{0.05}Sb_2$ at three different temperatures in the VRH regime. Symbols are experimental data points and red solid lines are linear fits. slope (α) has been deduced from these linear fits. The insets shows a linear plot of α versus $(T_0/T)^{3/4}$

Fig 5.14 shows the variation of resistance as a function of temperature in the metallic regime for $Fe_{0.9}Ni_{0.1}Sb_2$ in the range 4 to 50 K at different magnetic fields from 0 to 12 T. Evidently the MR is positive which decreases with increase of temperature. At low temperatures for fields greater than 2 T, resistance shows a minima at T_{min}, below which R(T) shows negative temperature coefficient of resistance. The T_{min} shifts to higher temperatures with increase of applied field as shown in the Fig 5.14. The behavior of R(T) for B = 4 - 12 T

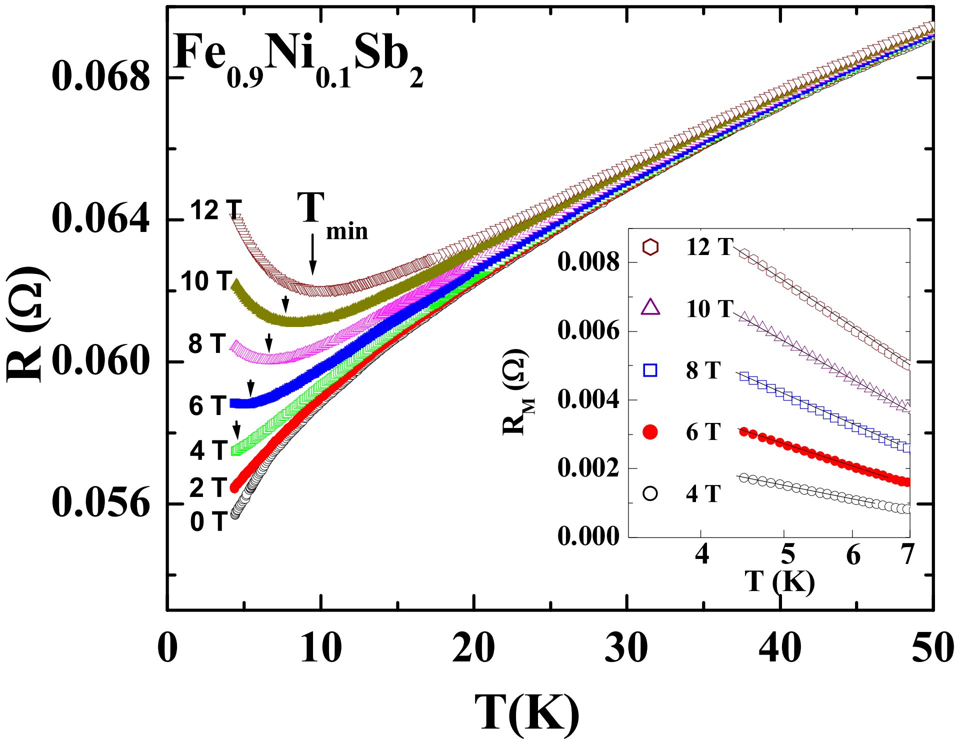

Figure 5.14: Resistance versus Temperature for $Fe_{0.9}Ni_{0.1}Sb_2$ at B = 0, 2, 4, 6, 8 10 and 12 T The inset shows R_M versus T at B = 4, 6, 8, 10 and 12 T as described in the text.

appears similar to the temperature dependent resistivity of Kondo metals at the low temperatures [20]. In order to ascertain whether resistance below T_{min} arises due to Kondo scattering, the magnetic scattering term R_M has been extracted by subtracting R at B=0T from R at B = 4-12 T (i.e. $R_M = R(B) - R(B=0T)$). In the inset of Fig 5.14 shows the R_M versus ln(T) plot which is observed to be linear as expected under Kondo scattering. This may imply that application of field in metallic regime, brought about by Ni substitution, tends to align the spin of magnetic impurity ions Ni leading to Kondo scattering that give negative temperature coefficient of resistance at low temperatures.

In what follows we attempt to understand the evolution of energy gap under high pressure as well as Ni substitution in $FeSb_2$. First we rationalize the non-monotonic variation of the energy gap with increase of pressure in $FeSb_2$ with in the realm of existing theoretical studies [12, 21, 22]. The band structure calculations [12] predict the non-monotonic variation of energy gap, i.e. an increase followed by a decrease with increase of pressure which is in accordance with the present study. However the same non-monotonic variation of Δ can also be understood by taking the hybridization-correlation models dealing with the Kondo insulating (KI) systems [21, 22]. According to these models the energy gap of a KI system depends on the strength of the hybridization (V) which is responsible for the opening of the gap because of mixing of the narrow d/f band with broad conduction band and the bandwidth (W) of the hybridized bands. Application of pressure tends to increase the hybridization V by bringing the d-band and the conduction band closer, whose net effect is to increase the energy gap Δ, since $\Delta \sim |V|^2 / \Delta E$ where ΔE is the energy difference between the localized d/f level and the Fermi level [23, 24]. On the other hand, pressure also increases the bands overlap and hence the bandwidth W of the hybridized bands which tends to fill the gap resulting in a decrease in Δ. Therefore pressure has both effect of increasing and decreasing the band gap. For the initial pressures, the increase in V dominates over the broadening of the bands leading to an increase in Δ, but at higher pressure the opposite happens. Thus, the trade off between these two opposing effects explains the observed non-monotonic variation of Δ. In a nutshell, the pressure dependence of energy gap can be understood within the purview of both the one electron picture and the model applicable for a many-body interaction system. The monotonic increase of Δ under Ni substitution in $Fe_{1-x}Ni_xSb_2$ can be readily understood within the aforementioned hybridization gap model, i.e., $[\Delta\ \alpha\ |V|^2/\Delta E\ ]$. Since Ni has smaller radius as compared to iron, the substitution of Ni compresses the lattice which tends to increase the hybridization V and hence increases energy gap Δ with increasing x. Although metallization is evident under high pressure as well as 10% Ni doping in $Fe_{1-x}Ni_xSb_2$ at low temperatures on account of delocalization of states localized inside the gap, a complete insulator to metal transition in the entire temperature range of 4.2 to 300 K is not observed up to the available applied pressure and Ni substitution carried out in present study.

5.4 Summary

Temperature dependent resistivity behavior of polycrystalline $FeSb_2$ has been studied as a function of magnetic field and pressure. The effect of chemical pressure has been studied with Ni substitution up to 10%. The main conclusions of the present study are

- Resistivity of $FeSb_2$ shows activated behavior in the HT regime, VRH behavior in the IT regime and power law behavior in the LT regime.
- The energy gap (Δ) in the HT regime exhibits non-monotonic variation, i.e. it increases initially and then decreases with increase of pressure which agrees with the band structure calculations as well as the theoretical model dealing with electron correlations.
- The VRH parameter T_0 decreases while localization length ξ increases with increase in pressure up to 5 GPa due to increase in delocalization of impurity states. The logarithmic derivative conductivity analysis indicates a MIT to occur at around 6 GPa at low temperature.

- With increase of Ni content in $Fe_{1-x}Ni_xSb_2$, the energy gap (Δ) increases in the HT regime. The VRH parameter T_0 decreases while localization length ξ increases with increase of Ni content up to 5% due to increase in delocalization of impurity states. For substitution of 10 % Ni, a MIT is observed to occur at T_{MIT} ~ 85 K in low temperature regime.
- In the metallic regime for 10 % Ni substituted sample, R(T) follows logarithmic temperature dependence below T_{min} in the presence of magnetic field indicating the emergence of Kondo-like scattering with increasing field.
- Although MIT transition is observed by the application of pressure and Ni substitution, complete metallization is not observed up to the applied pressure of 8.8 GPa and 10 % Ni substitution.

References

1. C. Petrovic, J. W. Kim, S. L. Bud'ko, A. I. Goldman, P. C. Canfield, W. Choe and G. J. Miller, *Phys. Rev B* **67**, 155205 (2003)
2. C. Petrovic, Y. Lee, T. Vogt, N. Dj. Lazarov, S. L. Bud'ko, and P. C. Canfield, *Phys. Rev B* **72**, 045103 (2005)
3. A. Bentien, S. Johnsen, G. K. H. Madsen, B. B. Iversen and F. Steglich, *Eur. Phys. Lett.* **80**, 17008 (2007)
4. Peijie Sun, Niels Oeschler, Simon Johnsen, Bo Brummerstedt Iversen, and Frank Steglich, *Phys. Rev B* **79**, 153308 (2009)
5. A. Perucchi, L. Degiorgi, Rongwei Hu, C. Petrovic, and V.F. Mitrovi´c, *Eur. Phys. Lett.* **54**, 175 (2006)
6. A. Herzog, M. Marutzky, J. Sichelschmidt, F. Steglich, S. Kimura, S. Johnsen and B. B. Iversen, *Phys. Rev B* **82**, 245205 (2010)
7. Rongwei Hu, V. F. Mitrović, and C. Petrovic, *Phys. Rev B* **79**, 064510 (2009)
8. Rongwei Hu, V. F. Mitrović, and C. Petrovic, *Phys. Rev B* **74**, 195130 (2006)
9. Rongwei Hu, R. P. Hermann, F. Grandjean, Y. Lee, J. B. Warren, V. F. Mitrović, and C. Petrovic, *Phys. Rev B* **76**, 224422 (2007)
10. A. Bentien, G. K. H. Madsen, S. Johnsen, and B. B. Iversen, *Phys. Rev B* **74**, 205105 (2006)
11. Rongwei Hu, V. F. Mitrović, and C. Petrovic, *Phys. Rev B* **76**, 115105 (2007)
12. X Wu, G Steinle-Neumann, S Qin, M Kanzaki and L Dubrovinsky, *J. Phys.: Condens. Matter* **21,** 185403 (2009)

13. C.M.Poffo, S.M.Souza , D.M.Triches , J.C.deLima, T.A.Grandi, A.Polian, M.Gauthier, Physica B **407** , 4686(2012)
14. A. Mobius, C. Frenzel, R. Thielsch, R. Rosenbaum, C. J. Adkins, M. Schreiber, H.-D. Bauer, R. Gro¨tzschel, V. Hoffmann, T. Krieg, N. Matz, H. Vinzelberg and M. Witcomb, *Phys. Rev B* **60**, 14209 (1999)
15. B I Shklovskii and A L Efros, *Electronic Properties of Doped Semiconductor* (Berlin : Springer) (1984)
16. Patrick A. Lee and T. V. Ramakrishnan, *Rev. Mod. Phys* **57**, 287 (1985)
17. Bernhard Kramer and Angus MacKinnon, *Rep. Prog. Phys*. **56** ,1469 (1993)
18. Elihu Abrahams and Gabriel Kotliar, *Science* **274**, 1853 (1996)
19. D Volhardt and P Wolfle, *Electronic Phase Transitions*, ed W Hanke and Yu V Kopaev (Amsterdam : Elseivier) 1992
20. C Kittel, *Introduction to Solid State Physics* (John Wiley & Sons, Inc., Newyork 1976)
21. Castor Fu and S. Doniach, *Phys. Rev B* **51**, 17439 (1995)
22. M. V. Tovar Costa , A. Troper, N. A. de Oliveira, Gloria M. Japiassu and M. A. Continentino, *Phys. Rev B* **57**, 6943 (1998)
23. J D Thomson, *Phsica B* **223** & **224**, 643 (1996)
24. S H Liu, *Handbook on Physics and Chemistry of Rare Earths* Vol 17, ed K A Gschneidner Jr, L Eyring G H Lander and G R Choppin (North-Holland:Elsevier) p 87

Chapter 6

Summary and Future Outlook

This thesis examined three topics; the underlying theme being perturbation of a robust magnetic ground state by chemical substitution and applied pressure. The first example pertains to the study of the change in the ground state properties of $BaFe_2As_2$ that stabilizes in a Spin Density Wave (SDW) ground state. This ground state is progressively modified as Co is substituted into the system, bringing in superconductivity. In this study extensive resistivity measurements have been performed in single crystalline samples, in the SDW region, the paramagnetic region and the superconducting region of the phase diagram of $BaFe_{2-x}Co_xAs_2$. In the SDW region of the samples, transverse magneto-resistance for B || c is positive. The magneto-resistance as a function of applied magnetic field lends a good understanding of the electronic structure of the crystals. In particular, the power law dependence of the magneto-resistance is used to delineate contributions of the transport from parabolic classical bands, versus electrons with linear E versus k, the latter contributing to quantum transport [1, 2]. The linear magneto-resistance arises when quantum transport dominates at low temperature and high magnetic fields, whereas, magneto-resistance shows a parabolic variation with magnetic field, when the classical regime of transport is operative, viz., at low field and high temperatures. The large contribution from quantum transport is the origin of low resistivity and high positive magneto-resistance seen in the SDW regime of the crystals.

These results on the pristine system are compared with magnetoresistance behaviour seen in the electron doped $BaFe_{1.92}Co_{0.08}As_2$ samples and in isoelectronically substituted $BaFe_{1.6}Ru_{0.4}As_2$ samples. These substitutions are seen to alter the quantum and classical transport regimes, and in the case of Co substitution by ~ 4%, the bands with linear dispersion are greatly suppressed. The suppression although present, is not as significant in the case of Ru substitution of ~20% at Fe site. The results clearly bring out the fact that the electron addition in $BaFe_2As_2$, as in the case of Co substituted samples, is more conducive for the suppression of the Dirac cone dispersed bands. On the contrary, in isoelectronically Ru substituted samples, the suppression of Dirac cone states is less marked although the composition of Ru is large ~20%. The magneto-resistance in the paramagnetic regime of the samples is insignificant and is consistent with the fact that electrons with Dirac dispersions do not exist in this regime.

Another significant finding of this chapter is the anisotropy in the transverse magneto-resistance observed for B || *ab* and B || *c* directions with increase of temperature, well within the SDW region in the underdoped Co-doped sample. Negative MR for B || *ab* has been attributed to de-twinning of the orthorhombic twins on account of the energetically more favourable configuration, for the ferromagnetically aligned spins that lie along the b-axis, to align with the magnetic field axis [3]. Positive MR for B || *c* arises due to classical and quantum transport of charge carriers from parabolic and Dirac cone states.

In the superconducting regime of the samples, using in-field resistance measurements with magnetic field up to 12 T applied along, both parallel and perpendicular to *a-b* plane of the single crystals, the upper critical behavior and its anisotropy are determined in $BaFe_{2-x}Co_xAs_2$ for x=0.082, 0.117 and 0.143. The anisotropy (γ) in the upper critical field obtained from these measurements, is found to increase with Co concentration. For a specific Co content, the anisotropy versus reduced temperature ($t=T/T_c$) shows an increase with increase of t and passes through a maximum close to T_c. The peak shifts to higher t with increase of composition. The low upper critical field anisotropy observed despite, the large resistivity anisotropy of ρ_c/ρ_{ab} ~100, and clear evidence for the presence of two dimensional Fermi surface features, is surprising. The temperature dependence of the upper critical field anisotropy implies multi-band superconductivity, the observation of peak close to T_c is generic to the Fe-As superconductors and needs further understanding.

The second example examines the case of an insulating G-type anti-ferromagnet, $BaMn_2As_2$ under pressure, turning it metallic, with a hint of producing superconductivity. Chemical substitution of $BaMn_2As_2$ also leads to a metallic ground state. $BaMn_2As_2$ has attracted great attention because it is a G-type antiferromagnetic semiconductor [4] with a large magnetic moment of 3.9 μ_B on Mn. This compound in a sense lies between the cuprate Mott insulating ground state and the itinerant SDW ground state of $BaFe_2As_2$. It is believed that a strong spin dependent hybridization between As *p* orbitals and Mn *d* orbitals occurs in this system, which means that by tuning the hybridization the magnetic moment on Mn can be altered. The unit cell volume of $BaMn_2As_2$ is also larger compared to the other neighbouring, iso-structural ternary transition metal pnictides, implying that it can be compressed. True to expectations, the high pressure resistivity measurements carried out on $BaMn_2As_2$ in the 4-300 K temperature and 0 – 8 GPa pressure ranges, reveal an insulator to metal transition upon application of ~ 5 GPa pressure. At pressures greater than 5 GPa, a steep fall of resistivity at a temperature ~ 17 K is clearly visible, in the metallic regime. This anomalous decrease in resistivity could be on account of spin density wave transition or superconducting transition which can only be confirmed by magnetization measurements under high pressures. To check if the metallization at 5 GPa is associated with any structural transition, high pressure XRD measurements were carried out at room temperature. A distinct change in slope in the unit cell volume versus pressure curve at ~ 5 GPa, is seen to occur without any change in the crystal structure. The observed anomaly in unit cell volume is attributed to an electronic transition, which is consistent with the resisivity data. Chemical substitution of Yb at Ba site and P at As site have resulted in significant changes in lattice parameters, affirming that they indeed substitute into the lattice. In addition, these substitutions also result in a large reduction in resistivity, possibly pointing to metallization by chemical substitution as well, in this system.

In the third major contribution in this thesis, a study of $FeSb_2$ Kondo-insulating system is presented. In this compound the magnetic moment on Fe is compensated due to the formation of Kondo singlet leading to an insulating state. Due to the large density of states at the band edges due to KI formation, it shows large thermopower. In fact this compound has been recently investigated due to the extraordinarily large thermo-power of ~45000 μV/K seen at 10 K [5]. The electrical resistivity measurements has been used to reveal a very small KI gap $\Delta \sim 300$ K [6]. The temperature dependent magnetic susceptibility shows the activated appearance of the paramagnetic moment due to quasi-particle excitations across the KI gap [6, 7]. In the thesis an attempt was made to study the behavior of $FeSb_2$ under application of external pressure and/or internal chemical pressure with Ni substitution to explore the possibility of inducing metallization in $FeSb_2$. This could be important, as a reduction in resistivity could be favourable for increasing the thermo-electric power factor in the system.

The temperature dependent high pressure resistivity measurements on $FeSb_2$ were carried out in the 0 to 8.8 GPa range and temperature range of 4K to 300K. The results imply that application of pressure induces delocalization of defects states present in the gap, for low pressures upto 6GPa. Beyond this pressure, there is a collapse of the gap at the highest pressures resulting in a metallic state below ~ 240 K under a pressure ~ 8.8 GPa. This chapter also shows that an insulator to metal transition can be effected at ~ 100 K by the substitution of 10% Ni at the Fe site of $FeSb_2$.

Detailed magneto-resistance measurements were carried out at ambient pressure in the pristine $FeSb_2$ and Ni substituted $FeSb_2$. While a positive magnetoresistance is seen in the pristine sample, the magneto-resistance becomes significantly pronounced by Ni substitution, possibly on account of magnetic field favouring a frozen Ni moment that leads to Kondo scattering of the defect states in the gap. Evidence for the latter is seen by plotting the R variation with T showing a logarithmic dependence at low temperatures, which gets accentuated with increase in magnetic field. The presence of defect states in the gap make delineating of extrinsic and intrinsic effects difficult. The scenario can be improved with measurements on single crystals.

6.1 Future outlook

1. The magneto-resistance behaviour of the SDW state should be measured in annealed single crystals of $BaFe_2As_2$, in order to obtain the magneto-resistance behaviour that truly reflects the electronic structure. This should be used to compare with magneto-resistance behaviour in all substituted similarly annealed crystals. This will help understand whether a given substitution will suppress the

Dirac cone dispersion present in $BaFe_2As_2$. In particular, a comparison of magneto-resistance behaviour of the case of hole doping by K at Ba site, Co at Fe site, Ru at Fe site and P at As site if carried out on single crystal samples, will be extremely instructive.

2. Evolution of Dirac Cone states with pressure can be investigated by combined high pressure and high magnetic field studies, which will be a clean way of suppressing states with Dirac Cone dispersion
3. Detailed correlation of the upper critical anisotropy with the resistivity anisotropy ρ_{ab}/ρ_c should be made for a variety of chemical substitutions, this will help elucidate the origin of the small upper critical field anisotropy seen in these systems.
4. Resistivity measurements under pressure should be carried out on the P and Yb doped $BaMn_2As_2$, already in the verge of metallization in order to look for superconductivity, under pressure in them
5. Magnetisation/neutron scattering measurements should be done under pressure, in order to understand the fate of the magnetic moment of Mn in $BaMn_2As_2$ under the application of pressure.
6. Many more Mn containing intermetallic samples viz., $CaMn_2As_2$, $SrMn_2Sb_2$, $BaMn_2Sb_2$, should be investigated in order to pin point the conditions under which the Mn moments get delocalized.
7. High pressure effects on single crystals of $FeSb_2$ should be carried out to delineate extrinsic and intrinsic effects on electron transport behaviour.
8. Thermopower measurements should be carried out in $FeSb_2$ and Ni substituted $FeSb_2$, in order to see if there is any significant increase in thermopower by the slight metallization seen in the Ni substituted compounds.

9. Thermopower under pressure in $FeSb_2$ will also be useful, in particular to understand if the observed decrease in resistivity under pressure, may contribute to higher thermoelectric power factor.

References

1. Khuong K Huynh, Yoichi Tanabe, and Katsumi Tanigaki, *Phys.Rev Lett.* **106**, 217004 (2010)
2. Hsueh-Hui Kuo, Jiun-Haw Chu, Scott C. Riggs, Leo Yu, Peter L. McMahon, Kristiaan De Greve, Yoshihisa Yamamoto, James G. Analytis, and Ian R. Fisher, *Phys. Rev.* B **84**, 054540 (2011)
3. Jiun-Haw Chu, James G. Analytis, David Press, Kristiaan De Greve, Thaddeus D. Ladd,Yoshihisa Yamamoto, and Ian R. Fisher1, *Phys. Rev.* B **81**, 214502 (2010)
4. D C Johnston, *Advances in Physics* **59***,* 803 (2010)
5. A. Bentien, S. Johnsen, G. K. H. Madsen, B. B. Iversen and F. Steglich, *Europhys. Lett.* **80**, 17008 (2007)
6. C Petrovic, J. W. Kim, S. L. Bud'ko, A. I. Goldman, P. C. Canfield, W. Choe and G. J. Miller, *Phys.Rev B* **67**, 155205 (2003)
7. C Petrovic, Y. Lee, T. Vogt, N. Dj. Lazarov, S. L. Bud'ko, and P. C. Canfield, *Phys.Rev B* **72**, 45103 (2005)

List of Publications

Publications included in Thesis

1. Upper critical field anisotropy in $BaFe_{2-x}Co_xAs_2$ single crystals synthesized without flux
K. Vinod, **A. T. Satya**, Shilpam Sharma, C. S. Sundar, and A. Bharathi
*Phys. Rev .B **84**, 012502 (2011)*
2. Kohler's rule in $Ba_{1-x}K_xFe_2As_2$
N. Ghosh, A. Bharathi, **A.T. Satya**, S. Sharma, Awadhesh Mani, R.M. Sarguna, D. Sornadurai, V.S. Sastry, C.S. Sundar
*Solid State Communications **150**, 1940 (2010)*
3. Pressure induced Metallization of $BaMn_2As_2$
***A*. T. Satya**, Awadhesh Mani, A. Arulraj, N. V. Chandra Shekar, K. Vinod, C. S. Sundar, and A. Bharathi
*Phys. Rev. B **84**, 180515(R) (2011)*
4. The pressure induced insulator to metal transition in $FeSb_2$
Awadhesh Mani, J Janaki, **A T Satya**, T Geetha Kumary and A Bharathi
*J. Phys.: Condens. Matter **24** , 075601 (2012)*
5. Influence of Ni doping on the electrical and structural properties of $FeSb_2$
J Janaki, Awadhesh Mani, **A.T.Satya,** T Geetha Kumary , S Kalavathi and A Bharathi
Phys. Status Solidi B **249**, No. 9, 1756–1760 (2012)

Publications not included in Thesis

1. Superconducting $Fe_{1+\delta}Se_{1-x}Te_x$ thin films: growth, characterization and properties
T Geetha Kumary, Dipak Kumar Baisnab, J Janaki, Awadhesh Mani, **A T Satya**, R M Sarguna, P K Ajikumar, A K Tyagi and A Bharathi
*Supercond. Sci. Technol. **22**, 095018 (2009)*
2. Critical properties of superconducting $Ba_{1-x}K_xFe_2As_2$
A. Bharathi , Shilpam Sharma, S. Paulraj, **A.T. Satya**, Y. Hariharan and C.S. Sundar
*Physica C **470**, 8 (2010)*
3. Superconductivity in Ru-substituted polycrystalline $BaFe_{2-x}Ru_xAs_2$
Shilpam Sharma, A. Bharathi, Sharat Chandra,V. Raghavendra Reddy, S. Paulraj, **A. T. Satya**, V. S. Sastry, Ajay Gupta, and C. S. Sundar
*Phys Rev B **81**, 174512 (2010)*
4. Intricacies of strain and magnetic field induced charge order melting in $Pr_{0.5}Ca_{0.5}MnO_3$ thin films
Dipak Kumar Baisnab n, T. Geetha Kumary, **A.T. Satya**, Awadhesh Mani, J. Janaki, R. Nithya, L.S. Vaidhyanathan, M.P. Janawadkar, A. Bharathi
*Journal of Magnetism and Magnetic Materials **323**, 2823 (2011)*
5. Superconducting and critical properties of $PrOFe_{0.9}Co_{0.1}As$: effect of P doping
Shilpam Sharma, Jai Prakash, Gohil S Thakur, **A T Satya** ,A Bharathi, A K Ganguli,

and C S Sundar
Supercond. Sci. Technol. ***24****, 065020(2011)*

6. Vibrational, magnetic, and dielectric behavior of La-substituted $BiFeO_3$-$PbTiO_3$ K. K. Mishra, **A. T. Satya**, A. Bharathi, V. Sivasubramanian, V. R. K.Murthy, and A. K. Arora
J Appl Phys ***110****, 123529 (2011)*

Published Conference Proceedings

1. Magnetisation Studies on Nickel Nano Particles
   A. T. Satya, T. Gnanasekaran and A. Bharathi
   DAE SSPS (2010) AIP Conf Proc *1349, 427 (2011)*
2. Strain enhanced charge order melting in $Pr_{0.5}Ca_{0.5}MnO_3$ thin films
   Dipak Kumar Baisnab, T.Geetha Kumary, **A.T.Satya**, Awadesh Mani, J.Janaki, R.Nithya, L.S.Vaidhyanathan, M.P.Janawadkar and A.Bharathi
   AIP Conf Proc. 1347,199 (2011)
3. Effect of hole doping on magnetic properties of $GdBaCo_2O_{5.5}$
   N. Thirumurugan, **A.T.Satya,** J.Janaki and A.Bharathi
   AIP Con Proc. 1347, 274-277 (2011)
4. Dirac Cone States in Ru doped $BaFe_2As_2$ as observed by Magneto Resistance measurements
   A. T. Satya, K.Vinod, Shilpam Sharma, C. S. Sundar and A.Bharathi
   56th DAE SSPS 2011, AIP Conf. Proc. 1447, 901 (2012);
5. Metal – Insulator transition upon Ni substitution in $Fe_{1-x}Ni_xSb_2$ Kondo Insulating system
   J. Janaki, Awadhesh Mani, **A. T. Satya**, T. Geetha Kumary, S. Kalavathi and A. Bharathi
   56th DAE SSPS 2011, AIP Conf. Proc. 1447, 929 (2012)
6. Phase Diagram of Ru Doped $BaFe_2As_2$
   K. Vinod, Shilpam Sharma, **A. T. Satya,** C. S. Sundar and A. Bharathi
   56th DAE SSPS 2011, AIP Conf. Proc. ***1447****, 889 (2012)*